

AD _____

Award Number: DAMD17-97-1-7272

TITLE: Breast Images with Diffusing Light Waves

PRINCIPAL INVESTIGATOR: Arjun G. Yodh, Ph.D.

CONTRACTING ORGANIZATION: University of Pennsylvania
Philadelphia, Pennsylvania 19104-3246

REPORT DATE: November 1999

TYPE OF REPORT: Final

PREPARED FOR: U.S. Army Medical Research and Materiel Command
Fort Detrick, Maryland 21702-5012

DISTRIBUTION STATEMENT: Approved for Public Release;
Distribution Unlimited

The views, opinions and/or findings contained in this report are those of the author(s) and should not be construed as an official Department of the Army position, policy or decision unless so designated by other documentation.

DTIC QUALITY ASSURED 4

20010124 091

REPORT DOCUMENTATION PAGE

*Form Approved
OMB No. 074-0188*

Public reporting burden for this collection of information is estimated to average 1 hour per response, including the time for reviewing instructions, searching existing data sources, gathering and maintaining the data needed, and completing and reviewing this collection of information. Send comments regarding this burden estimate or any other aspect of this collection of information, including suggestions for reducing this burden to Washington Headquarters Services, Directorate for Information Operations and Reports, 1215 Jefferson Davis Highway, Suite 1204, Arlington, VA 22202-4302, and to the Office of Management and Budget, Paperwork Reduction Project (0704-0188), Washington, DC 20503

1. AGENCY USE ONLY (Leave blank)	2. REPORT DATE November 1999	3. REPORT TYPE AND DATES COVERED Final (1 Sep 97 - 31 Aug 99)
4. TITLE AND SUBTITLE Breast Images with Diffusing Light Waves		5. FUNDING NUMBERS DAMD17-97-1-7272
6. AUTHOR(S) Arjun G. Yodh, Ph.D.		
7. PERFORMING ORGANIZATION NAME(S) AND ADDRESS(ES) University of Pennsylvania Philadelphia, Pennsylvania 19104-3246 E-Mail: yodh@dept.physics.upenn.edu		8. PERFORMING ORGANIZATION REPORT NUMBER
9. SPONSORING / MONITORING AGENCY NAME(S) AND ADDRESS(ES) U.S. Army Medical Research and Materiel Command Fort Detrick, Maryland 21702-5012		10. SPONSORING / MONITORING AGENCY REPORT NUMBER
11. SUPPLEMENTARY NOTES This report contains colored photos		
12a. DISTRIBUTION / AVAILABILITY STATEMENT Approved for Public Release; Distribution Unlimited		12b. DISTRIBUTION CODE
13. ABSTRACT (Maximum 200 Words) Our work over the last year aimed to develop and assess the utility of various theoretical and experimental diffuse light imaging schemes for tumor detection and characterization within the human breast. We have theoretically and numerically investigated the angular spectrum approach in the parallel plate (compressed breast) geometry. One paper investigated the use of depth dependent regularization and mathematical filtering methods to improve the fidelity of these projection images in the presence of noise. In a related publication we documented a group of refinements to the diffraction tomographic techniques. On the experimental side we have built a soft compression plate apparatus for diffuse optical tomography of the breast. The device was used to experimentally test the angular spectrum and other theoretical approaches. Through this work we uncovered some technical limitations of diffuse optical tomography based on the angular spectrum approach, and, importantly, we developed other schemes for improved breast imaging. In this vein we derived a new integro-differential equation for bounded media within the diffusion approximation, which makes possible full 3D reconstruction in the compressed breast geometry.		
14. SUBJECT TERMS diffuse optical tomography; optical mammography; near-infrared optical diagnostics; image reconstruction		15. NUMBER OF PAGES 95
		16. PRICE CODE
17. SECURITY CLASSIFICATION OF REPORT Unclassified	18. SECURITY CLASSIFICATION OF THIS PAGE Unclassified	19. SECURITY CLASSIFICATION OF ABSTRACT Unclassified
		20. LIMITATION OF ABSTRACT Unlimited

FOREWORD

Opinions, interpretations, conclusions and recommendations are those of the author and are not necessarily endorsed by the U.S. Army.

Where copyrighted material is quoted, permission has been obtained to use such material.

Where material from documents designated for limited distribution is quoted, permission has been obtained to use the material.

X Citations of commercial organizations and trade names in this report do not constitute an official Department of Army endorsement or approval of the products or services of these organizations.

In conducting research using animals, the investigator(s) adhered to the "Guide for the Care and Use of Laboratory Animals," prepared by the Committee on Care and use of Laboratory Animals of the Institute of Laboratory Resources, national Research Council (NIH Publication No. 86-23, Revised 1985).

For the protection of human subjects, the investigator(s) adhered to policies of applicable Federal Law 45 CFR 46.

In conducting research utilizing recombinant DNA technology, the investigator(s) adhered to current guidelines promulgated by the National Institutes of Health.

In the conduct of research utilizing recombinant DNA, the investigator(s) adhered to the NIH Guidelines for Research Involving Recombinant DNA Molecules.

In the conduct of research involving hazardous organisms, the investigator(s) adhered to the CDC-NIH Guide for Biosafety in Microbiological and Biomedical Laboratories.

 2/18

PI - Signature Date

Table of Contents

Front Cover	i
SF 298, Report Documentation Page	ii
Foreword	iii
Table of Contents	iv
Introduction	1
Body	1
Key Research Accomplishments	3
Reportable Outcomes	3
Conclusions	3
References	4
Appendices	5
Final Reports	5

Introduction

Broadly speaking our work aimed to develop and assess the utility of various theoretical and experimental diffuse light imaging schemes for tumor detection and characterization within the human breast. During the last year we have theoretically and numerically investigated the angular spectrum approach in the parallel plate (compressed breast) geometry. On the experimental side we have built a soft compression plate apparatus for diffuse optical tomography of the breast. The device was used to experimentally test the angular spectrum and other theoretical approaches. We have pilot tested the instrument with tissue phantoms and in a few clinical scenarios. Through this work we uncovered some technical limitations of diffuse optical tomography based on the angular spectrum approach, and, importantly, we developed other schemes for improved breast imaging.

Body

Below we have summarized our progress related to each of three specific aims outlined for this grant.

Specific aim 1

To theoretically explore the utility of the FFT approach for breast tumor imaging with diffusing light in the parallel plate compressed breast configuration.

During the last year we contributed 2 papers that developed diffraction tomographic techniques for diffuse optical imaging. The first paper investigated the use of depth dependent regularization and mathematical filtering methods to improve the fidelity of these projection images in the presence of noise [1]. In This paper we developed an algorithm that stabilized the diffraction tomographic deconvolution for optimal resolution at all depths. In addition we found an empirical method to estimate the depth of a heterogeneity of interest using only 2D projection images. In a related publication we documented a group of refinements to the diffraction tomographic techniques [2]. These improvements included incorporating boundary conditions in order to extend the technique to slab media of finite size and to semi-infinite media. The modified theory with better boundary conditions was demonstrated to be superior to the initial formulation using numerical simulations plus noise. We also studied the cross-coupling of absorption and scattering; an important finding of these numerical experiments was that cross-coupling of absorption and scattering would arise in samples for which the thin slice approximation breaks down. This finding suggested that 2D projection images alone will not be sufficient to reconstruct true optical properties in many practical situations, and that some form of 3D reconstruction is critical.

Specific aim 2

To construct an apparatus based on photon migration technology that will enable us to test image reconstruction approaches with realistic conditions and signal to noise ratios. We have made substantial progress in instrumentation development during the last year. There were several important issues to be faced as we began this project. Since the focus of the grant was on the FFT approach, we designed a compressed breast instrument for which it was possible to rigorously test these theoretical schemes. At the same time

however, we wanted to design an apparatus that would be adaptable to other theoretical and experimental approaches that we hoped to investigate.

So far we have primarily been using the frequency domain version of the apparatus to measure the optical properties of tissue phantoms and of normal breast [3]. At the heart of the device are two parallel compression plates (e.g. a “source-plate” and an “output-plate”) with adjustable separation. The original version of the source plate had one source fiber coupled in series to 3 amplitude modulated (140MHz) diode lasers operating at 3 wavelengths in the NIR (750nm, 786nm, and 830nm). The original version of the detection plate had a scannable detection fiber. Typically we would scan the fiber over an ~10x10cm area in steps of 0.5 cm, which required about 20 minutes

We used the original device to demonstrate the basic ideas of the angular spectrum approach, and also to show the limitations of the approach experimentally in tissue phantoms. We also used the device in pilot measurements of the average optical properties of normal human breast. In carrying out these latter studies we obtained a better understanding of some of the clinical problems that will arise in practice. For example, proper treatment of the chest boundary was critical for obtaining correction optical properties. It also became apparent that one needed to obtain a larger data sets, more quickly (i.e. than 20 minutes) in order to push the methodology effectively into the clinic, and to carry out realistic 3D image reconstructions. In this vein we have designed and started building a second-generation optical mammography device that employs a CCD camera that rapidly collects large data sets [4].

Specific aim 3

To theoretically formulate and demonstrate non-perturbative approaches to homogenous and heterogenous media that explicitly incorporates the boundary conditions and that is accurate when variations in scattering and absorption are large (i.e. not in the perturbative limit).

In this vein we derived a new integro-differential equation for bounded media within the diffusion approximation (also following the principles of diffraction tomography) which readily makes possible full 3D reconstructions in the compressed breast geometry [5]. The new technique employs a series of *plane* diffuse photon density waves with different modulation frequencies. It requires both two-dimensional FFT operations (as in the original approach) and a one-dimensional matrix inversion.

In addition we developed finite difference numerical codes for data inversion. This approach was utilized to obtain measurements of the *bulk* optical properties of tissue phantoms and normal breast using the apparatus developed in specific aim 2. During the course of analyzing the results of clinical measurements it became apparent that our *analytical* schemes were suffering in practical scenarios. As a result we developed finite difference numerical codes for data inversion. These *numerical* schemes can flexibly segment and extend the regions of interest. In particular we have been using the explicit adjoint formulation for the inverse problem. Most DOT approaches have been implemented in 2D. In the best 2D cases, researchers have employed a cylindrical geometry to reduce the dimensionality of the problem. In fact, only recently have a few direct comparisons between full 3D and 2D reconstructions been made using simulated data; not surprisingly the 3D reconstructions were superior. Furthermore in any clinical setting the forward problem is necessarily 3D. This is especially true for our compressed

plate geometry where there is no intrinsic symmetry about which to reduce the dimensionality of the problem. A description of these numerical schemes is provided [6].

Key Research Accomplishments

- Developed an algorithm that stabilized the diffraction tomographic technique for optimal resolution at all depths.
- Found an empirical method to estimate the depth of a heterogeneity of interest using only 2D projection images.
- Incorporated boundary conditions into the diffraction tomography approach in order to extend the technique to slab media of finite size and to semi-infinite media.
- Derived a new integro-differential equation for bounded media within the diffusion approximation (also following the principles of diffraction tomography), which readily makes possible full 3D reconstructions in the compressed breast geometry.
- Demonstrate the basic ideas and tested the limitations of the angular spectrum approach using clinical prototype imager.
- Designed and started building a second-generation optical mammography device employing a CCD camera to rapidly collects large data sets.
- Developed finite difference numerical codes for data inversion.

Reportable outcomes

- Grant: Parallel, Rapid Diffuse Optical Tomography of Breast
- Grant: Parallel Detection and Computation for Diffuse Tomography of Breast
- Durduran, T., Culver, J.P., Hoboke, M.J., Li, X.D., Zubkov, L., Chance, B., Pattanayak, D.N., and Yodh, A.G., Algorithms for 3D localization and imaging using near-field diffraction tomography with diffuse light, Optics Express 4, 247-262 (1999).
- Li, X.D., Pattanayak, D.N., Durduran, T., Culver, J.P., Chance, B., and Yodh, A.G., Near-field diffraction tomography with diffuse photon density waves, (Accepted by Physical Review B) (2000).
- Durduran, T., Holboke, M., Culver, J.P., Zubkov, L., Choe, R., Pattanayak, D.N., Chance, B., and Yodh, A.G., Tissue bulk optical properties of breasts and phantoms obtained with clinical optical imager (To be published, Technical Digest Biomedical Topical Meeting, OSA) (2000).
- Culver, J.P., Ntziachristos, V., Zubkov, L., Durduran, T., Pattanayak, D.N., and Yodh, A.G., Data set size and image quality in diffuse optical mammography: evaluation of a clinical prototype (To be published, Technical Digest Biomedical Topical Meeting, OSA) (2000).
- Pattanayak, D.N., and Yodh, A.G., Diffuse optical 3D-slice imaging of bounded turbid media using a new integro-differential equation, Optics Express 4, 231-240 (1999).
- Holboke, M.J. and Yodh, A.G., Parallel three-dimensional diffuse optical tomography (To be published, Technical Digest Biomedical Topical Meeting, OSA) (2000).

Conclusions

In our work over the last year we developed and assessed the utility of various theoretical and experimental diffuse light imaging schemes for tumor detection and characterization

within the human breast. Focusing on the parallel plate (compressed breast) geometry, we have theoretically and numerically investigated the angular spectrum approach.

Significant progress was made in stabilizing the technique with respect to measurement noise and extending the technique to clinically relevant geometries. Through this work we uncovered some technical limitations of diffuse optical tomography based on the angular spectrum approach, and, importantly, we developed other schemes for improved breast imaging. In particular we have derived a new integro-differential equation for bounded media within the diffusion approximation and developed finite difference numerical codes for arbitrary geometries.

On the experimental side we have built a soft compression plate apparatus for diffuse optical tomography of the breast and conducted pilot tests of the instrument with tissue phantoms and in a few clinical scenarios. While using the current system for bulk tissue properties it became obvious that the data acquisition speed needed to be increased significantly. As a result we designed and began building a second-generation mammography machine using a CCD camera. The larger data sets will be complemented by future efforts to develop parallel processor image reconstruction code.

In conclusion we have gained significant knowledge and experience with the optical mammography problem during this period. As a result of this understanding, we have designed and started the development of novel computational and experimental tools that permit rapid acquisition and analysis of informationally dense diffuse optical data sets in the compressed breast geometry.

References

1. Durduran, T., Culver, J.P., Hoboke, M.J., Li, X.D., Zubkov, L., Chance, B., Pattanayak, D.N., and Yodh, A.G., Algorithms for 3D localization and imaging using near-field diffraction tomography with diffuse light, *Optics Express* 4, 247-262 (1999).
2. Li, X.D., Pattanayak, D.N., Durduran, T., Culver, J.P., Chance, B., and Yodh, A.G., Near-field diffraction tomography with diffuse photon density waves, (*Accepted by Physical Review B*) (2000).
3. Durduran, T., Holboke, M., Culver, J.P., Zubkov, L., Choe, R., Pattanayak, D.N., Chance, B., and Yodh, A.G., Tissue bulk optical properties of breasts and phantoms obtained with clinical optical imager (To be published, *Technical Digest Biomedical Topical Meeting, OSA*) (2000).
4. Culver, J.P., Ntziachristos, V., Zubkov, L., Durduran, T., Pattanayak, D.N., and Yodh, A.G., Data set size and image quality in diffuse optical mammography: evaluation of a clinical prototype (To be published, *Technical Digest Biomedical Topical Meeting, OSA*) (2000).
5. Pattanayak, D.N., and Yodh, A.G., Diffuse optical 3D-slice imaging of bounded turbid media using a new integro-differential equation, *Optics Express* 4, 231-240 (1999).
6. Holboke, M.J. and Yodh, A.G., Parallel three-dimensional diffuse optical tomography (To be published, *Technical Digest Biomedical Topical Meeting, OSA*) (2000).

Appendices

Please see attached.

Final Reports

Bibliography

- Durduran, T., Culver, J.P., Hoboke, M.J., Li, X.D., Zubkov, L., Chance, B., Pattanayak, D.N., and Yodh, A.G., Algorithms for 3D localization and imaging using near-field diffraction tomography with diffuse light, *Optics Express* 4, 247-262 (1999).
- Li, X.D., Pattanayak, D.N., Durduran, T., Culver, J.P., Chance, B., and Yodh, A.G., Near-field diffraction tomography with diffuse photon density waves, (Accepted by *Physical Review B*) (2000).
- Durduran, T., Holboke, M., Culver, J.P., Zubkov, L., Choe, R., Pattanayak, D.N., Chance, B., and Yodh, A.G., Tissue bulk optical properties of breasts and phantoms obtained with clinical optical imager (To be published, *Technical Digest Biomedical Topical Meeting, OSA*) (2000).
- Culver, J.P., Ntziachristos, V., Zubkov, L., Durduran, T., Pattanayak, D.N., and Yodh, A.G., Data set size and image quality in diffuse optical mammography: evaluation of a clinical prototype (To be published, *Technical Digest Biomedical Topical Meeting, OSA*) (2000).
- Pattanayak, D.N., and Yodh, A.G., Diffuse optical 3D-slice imaging of bounded turbid media using a new integro-differential equation, *Optics Express* 4, 231-240 (1999).
- Holboke, M.J. and Yodh, A.G., Parallel three-dimensional diffuse optical tomography (To be published, *Technical Digest Biomedical Topical Meeting, OSA*) (2000).
- Li, X.D., Durduran, T., Yodh, A.G., Chance, B., and Pattanayak, D.N., Diffraction tomography for biochemical imaging with diffuse-photon density waves, *Opt. Lett.* 22, 573-575 (1997).
- Zhu, Q., Durduran, T., Ntziachristos, V., Holboke, M., and Yodh, A.G., Imager that combines near-infrared diffusive light and ultrasound, *Optics Letters* 24, 1050-1052 (1999).
- Holboke, M., Fishkin, J., Tromberg, B., Yodh, A.G., Three dimensional diffuse optical mammography segmentation and sensitivity studies, *Journal of Biomedical Optics* (submitted for publication, Oct. 1999).
- Li, X.D., Durduran, T., Yodh, A.G., Chance, B., and Pattanayak, D.N., Diffraction tomography for biochemical imaging with diffuse-photon density waves, *Optics Letters* 22, 573-575 (1997).
- Li, X., Pattanayak, D.N., Durduran, T., Culver, J., Chance, B., and Yodh, A.G., Near-field diffraction tomography with diffuse photon density waves, (submitted to *Phys Rev E*, Aug 1999).
- Pattanayak, D.N., Resolution of optical images formed by diffusion waves in highly scattering media, *GE Tech. Info. Series*, 91CRD241 (1991).

- Durduran, T., Culver, J., Zubkov, M., Holboke, M. Choe, R., Li, X.D., Chance, B., Pattanayak, D.N., and Yodh, A.G., Diffraction tomography in diffuse optical imaging; filters & noise, SPIE 3597 (1999).

Personnel

- Arjun G. Yodh
- Deva N. Pattanayak
- Xingde Li
- Joseph P. Culver
- Turgut Durduran
- Leonid Zubkov
- Monica J. Holboke
- Britton Chance

Algorithms for 3D localization and imaging using near-field diffraction tomography with diffuse light

Turgut Durduran, J. P. Culver, M. J. Holboke, X. D. Li*
and Leonid Zubkov

Department Of Physics and Astronomy,

University of Pennsylvania, Philadelphia, PA 19104

* Now with the Department of Electrical Engineering and Computer Sciences,
Massachusetts Institute of Technology, Cambridge, Massachusetts 02139

durduran@mail.sas.upenn.edu

B. Chance

*Department of Biophysics and Biochemistry,
University of Pennsylvania, Philadelphia, PA 19104*

chance@mail.med.upenn.edu

Deva N. Pattanayak* and A. G. Yodh

*Department Of Physics and Astronomy,
University of Pennsylvania, Philadelphia, PA 19104*

* Also at Silicon Power Corporation, Latham NY 12110

*pattanayak@aol.com
yodh@dept.physics.upenn.edu*

Abstract: We introduce two filtering methods for near-field diffuse light diffraction tomography based on the angular spectrum representation. We then combine these filtering techniques with a new method to find the approximate depth of the image heterogeneities. Taken together these ideas improve the fidelity of our projection image reconstructions, provide an interesting three dimensional rendering of the reconstructed volume, and enable us to identify and classify image artifacts that need to be controlled better for tissue applications. The analysis is accomplished using data derived from numerical finite difference simulations with added noise.

©1999 Optical Society of America

OCIS codes: (170.3010) Image reconstruction techniques; (170.5280) photon migration; (170.3830) mammography; (170.5270) Photon density waves; (170.3660) Light propagation in tissues

References and links

1. A. G. Yodh and B. Chance, "Spectroscopy and imaging with diffusing light," *Physics Today* **48**, 34-40 (March 1995).
2. B. Chance, in *Photon Migration in Tissues* (Plenum Press, 1989).
3. B.J Trombeg, L. O. Svaasand, T. Tsay and R.C.M. Haskell, "Properties of Photon Density Waves in Multiple-Scattering Media," *Appl. Opt.* **32**, 607 (1993).
4. M. A. O'Leary, D. A . Boas, B. Chance and A.G. Yodh, "Experimental Images of heterogeneous turbid media by frequency-domain diffusing-photon tomography," *Opt. Lett.* **20**, 426-428 (1995).
5. H. Jiang, K. D. Paulsen, U. L. Osterberg, B. W. Pogue and M.S. Patterson, "Optical Image reconstruction using frequency-domain data: Simulations and experiments," *J. Opt. Soc. Am. A* **13**, 253-266 (1996).

6. Y. Yao, Y. Wang, Y. Pei, W. Zhu and R. L. Barbour, "Frequency-domain optical imaging of absorption and scattering distributions using a born iterative method," *J. Opt. Soc. Am. A* **14**, 325-342 (1997).
7. M. O'Leary, "Imaging with Diffuse Photon Density Waves," in PhD Thesis (Dept. Physics & Astronomy, U. of Pennsylvania, May 1996) .
8. M. S Patterson, B. Chance and B. C. Wilson, "Time Resolved Reflectance And Transmittance for the Non-Invasive Measurement of Tissue Optical Properties," *Appl. Opt.* **28**, 2331 (1989).
9. S. R. Arridge, "Forward and inverse problems in time-resolved infrared imaging," in *Medical Optical Tomography: Functional Imaging and Monitoring*, ed. G. Muller and B. Chance, Rl. Alfano, S. Arridge, J. Beuthan, E. Gratton, M Kaschke, B. Masters, S. Svanberg and P. van der Zee, Proc SPIE IS11, 35-64 (1993).
10. D. A. Benaron, D. C. Ho, S. Spilman, J. P. Van Houten and D. K. Stevenson, "Tomographic time-of-flight optical imaging device," *Adv. Exp. Med. Biol.* **361**, 609-617 (1994).
11. Gratton, E. and J. B. Fishkin, "Optical spectroscopy of tissue-like phantoms using photon density waves," *Comments on Cell. and Mol. Biophys.* **8(6)**, 309-359 (1995).
12. J. B. Fishkin, O. Coquoz, E. R. Anderson, M. Brenner and B. J. Tromberg, "Frequency-domain photon migration measurements of normal and malignant tissue optical properties in a human subject," *Appl. Opt.* **36**, 10 (1997).
13. W. Bank and B. Chance, "An Oxidative Effect in metabolic myopathies - diagnosis by noninvasive tissue oximetry," *Ann. Neurol.* **36**, 830 (1994).
14. Y. Hoshi and M. Tamura, "Near-Infrared Optical Detection of Sequential Brain Activation in The Prefrontal cortex during mental tasks," *Neuroimage*. **5**, 292 (1997).
15. A. Villringer and B. Chance, "Non-invasive optical spectroscopy and imaging of human brain functions," *Trends. Neurosci.* **20**, 435 (1997) .
16. B. Chance, Q. M. Luo, S. Nioka, D. C. Alsop and J.A. Detre, "Optical investigations of physiology: a study of intrinsic and extrinsic biomedical contrast," *Phil. Trans. Roy. Soc. London B.* **352**, 707 (1997).
17. BW Pogue and KD Paulsen, "High-resolution near-infrared tomographic imaging simulations of the rat cranium by use of apriori magnetic resonance imaging structural information," *Opt. Lett.* **23**, 1716-1718 (1998).
18. R. M. Danen, Y. Wang, X. D. Li, W. S. Thayer and A.G.Yodh, "Regional imager for low-resolution functional imaging of the brain with diffusing near-infrared light," *Photochem. Photobiol.* **67**, 33-40 (1998).
19. J.H.Hoogenraad, M.B.van der Mark, S.B.Colak, G.W.'t Hooft and E.S.van der Linden, "First Results from the Philips Optical Mammoscope," Proc.SPIE / BiOS-97 (SanRemo, 1997) .
20. S.K. Gayen, M.E.Zevallos, B. B. Das, R. R. Alfano and "Time-sliced transillumination imaging of normal and cancerous breast tissues," in *Trends in Opt. And Photonics*, ed. J. G. Fujimoto and M. S. Patterson.
21. X.D.Li, J. Culver, D. N. Pattanayak, A. G. Yodh and B. Chance, "Photon Density Wave Imaging With K-Space Spectrum Analysis: clinical studies - background subtraction and boundary effects," Technical Digest Series - CLEO '98, **6**, 88-89 (1998).
22. Fantini, S., S. A. Walker, M. A. Franceschini, K. T. Moesta, P. M. Schlag, M. Kaschke, and E. Gratton. "Assessment of the size, position, and optical properties of breast tumors in vivo by non-invasive optical methods" *Appl. Opt.*, **37**, 1982-1989 (1998).
23. Franceschini, M. A., K. T. Moesta, S. Fantini, G. Gaida, E. Gratton, H. Jess, W. W. Mantulin, M. Seeber, P. M. Schlag, and M. Kaschke. "Frequency-domain instrumentation techniques enhance optical mammography: Initial clinical results" *Proc. Natl. Acad. Sci. USA*, **94**, 6468-6473 (1997).
24. S. Fantini, M. A. Franceschini, G. Gaida, E. Gratton, H. Jess and W.W. Mantulin, "Frequency-domain optical mammography: edge effect corrections," *Med. Phys.* **23**, 149 (1996).
25. E. Wolf, "Principles and Development of Diffraction Tomography" in *Trends in Optics*, ed. A. Consortini (Academic Press, San Diego, 1996).
26. A.J.Devaney, "Diffraction Tomography," *Inv. Meth. In Electromagnetic Imaging*, 1107-1135 .
27. E. Wolf, "Inverse Diffraction and a New Reciprocity Theorem," *J. Opt. Soc. Am.* **58**, 1568 (1968).
28. E. Wolf , "Three Dimensional Structure Determination of Semi-Transparent Objects From Holographic Data," *Opt. Commun.* **1** , 153-156 (1969).

29. BQ Chen, JJ Stamnes, and K Stamnes, "Reconstruction algorithm for diffraction tomography of diffuse photon density waves in a random medium". Pure Appl Opt ,**7**, 1161-1180 (1998).
30. DL Lasocki, CL Matson and PJ Collins, "Analysis of forward scattering of diffuse photon-density waves in turbid media: a diffraction tomography approach to an analytic solution," Opt. Lett. **23**, 558-560 (1998).
31. D. N. Pattanayak, "Resolution of Optical Images Formed by Diffusion Waves in Highly Scattering Media," GE Tech. Info. Series **91CRD241** (1991).
32. X.D.Li, T. Durduran, A.G. Yodh, B. Chance and D.N. Pattanayak, "Diffraction Tomography for Biomedical Imaging With Diffuse Photon Density Waves," Opt. Lett. **22**, 573-575 (1997).
33. X.D.Li, in PhD Thesis (Dept. Physics & Astronomy, U. of Pennsylvania, May 1998).
34. X.D.Li, D. N. Pattanayak, J. P. Culver, T. Durduran and A. G. Yodh, "Near-Field Diffraction Tomography with Diffuse Photon Density Waves," to be published (1998).
35. X. Cheng and D. Boas, "Diffuse Optical Reflection Tomography Using Continous Wave Illumination," Opt. Express **3**, 118-123 (1998), <http://pubs.osa.org/oearchive/source/5663.htm>.
36. J. C. Schotland, "Near-field Inverse Scattering: Microscopy to Tomography," SPIE 3597 (1999).
37. C. L. Matson, N. Clark, L. McMackin and J. S. Fender, "Three-dimensional Tumor Localization in Thick Tissue with The Use of Diffuse Photon-Density Waves," Appl. Opt. **36**, 214-219 (1997).
38. C. L. Matson, "A Diffraction Tomographic Model Of The Forward Problem Using Diffuse Photon Density Waves," Opt. Express **1**, 6-11 (1997), <http://pubs.osa.org/oearchive/source/1884.htm>.
39. S. J. Norton and T. Vo-Dinh, "Diffraction Tomographic Imaging With Photon Density Waves: an Explicit Solution," J. Opt. Soc. Am. A **15**, 2670-2677 (1998).
40. J. C. Schotland, "Continous Wave Diffusion Imaging," J. Opt. Soc. Am. A **14**, 275-279 (1997).
41. T. Durduran, J. Culver, L. Zubkov, M. Holboke, R. Choe, X. D. Li, B. Chance, D. N. Pattanayak, A. G. Yodh, "Diffraction Tomography In Diffuse Optical Imaging; Filters & Noise," SPIE 3597 (1999).
42. J. Ripoll and M. Nieto-Vesperinas, "Reflection and Transmission Coefficients of Diffuse Photon Density Waves," in press.
43. J. Ripoll and M. Nieto-Vesperinas, "Spatial Resolution of Diffuse Photon Density Waves," to be published in J. Opt. Soc. Am.A (1999).
44. C. L. Matson, "Resolution, Linear Filtering , and Positivity," J. Opt. Soc. Am. A **15**, 33-41 (1998).
45. F. J. Harris, "On The Use of Windows For Harmonic Analysis with the Discrete Fourier Transform," Proc. Of IEEE **66**, 51-83 (1978).
46. A.Kak and M. Slaney, in *Principles of Computerized Tomographic Imaging* (IEEE Press, New York, 1988).
47. A.J.Devaney, "Linearised Inverse Scattering in Attenuating Media," Inv. Probs. **3**, 389-397 (1987).
48. A. J. Devaney, "Reconstructive Tomography With Diffracting Wavefields," Inv. Probl. **2**, 161-183 (1986).
49. Essentially we assume that the scattering contrast ($\delta\mu'_s$) is slowly varying. For a detailed description we refer to [33] and [34].
50. A.J. Banos, in *Dipole Radiation In the Presence of a Conducting Half-Space* (Pergamon Press, New York, 1966).
51. J. W. Goodman, in *Introduction To Fourier Optics*, (McGraw-Hill, San Fransisco , 1968).
52. We are aware of a similar normalization scheme by Hanli Liu and her collaborators (private communications SPIE Jan 1999).

1. Introduction

Diffuse photon density waves (DPDWs) [1-7] and their time-domain analogs [8-10] can provide quantitative spectroscopic information about tissue structure, tissue chromophores, and tissue metabolism. Tomographic imaging of deep tissues with diffusive waves offers the possibility for functional imaging based on these spectroscopic contrasts. Thus image reconstruction has been explored intensely with varying degrees of success in tissue phantoms [11,12], the brain [13-18], and the breast [19-24]. One theoretical approach that has received significant recent interest is the method of diffraction tomography [25-28] extended to the near-field [29-43]. This scheme is particularly well suited for planar source-detection geometries that arise for example, in breast imaging. The methodology has attracted attention [29-43] because the diffusive wave modes derived using the angular-spectrum representation provide a very convenient framework for imaging in parallel-plate geometries, and for analytic or semi-analytic investigation of resolution and signal-to-noise issues. The method also offers a very fast and direct way to obtain two-dimensional projection images of the turbid media; these images are essentially optical mammograms[21].

In this contribution we study a set of theoretical issues associated with image reconstruction using near-field diffraction tomography. In order to obtain quality images, for example, one apply spectral filters [41-46] to the data at several levels of the image processing (i.e. filters with respect to spatial frequencies in the reconstructions). Well defined rules do not exist for choosing these filter functions; in fact different filter functions introduce uncontrolled systematic errors into the images [41] . Additionally, the images are dramatically improved when the experimenter has knowledge of the approximate depth of the optical heterogeneity. Object depth determination is generally difficult unless one has other means to obtain this information such as multiple optical views of the same sample or image segmentation from other types of diagnostics.

We investigate both critical issues in this paper, and demonstrate algorithms for optimizing projection image fidelity. Data for these studies is derived from numerical simulations with added noise. Two kinds of mathematical filters are introduced; (1) a phase-only filter which does not have any free parameters and allows accurate localization, and (2) a depth and noise dependent low-pass filter with the cut-off frequency as a free parameter. Then the two filtering methods are combined with a technique to find the approximate depth of the heterogeneities. We obtain two dimensional projection images and we demonstrate a three dimensional rendering of these image projections which appears promising for clinical applications. Our work clarifies the mentioned issues in a quantitative way; it makes apparent the limitations of the technique, identifies artifacts and directions for improvement.

2. Theory

2.1 Angular spectrum representation of diffuse photon density waves

The angular-spectrum representation provides a set of modes well suited for the description of the propagation and scattering of diffuse photon density waves in parallel-plate geometries (fig.(1)). The representation and its applications have been described by numerous investigators in optics [25-28,47-48] and in the photon migration community [29-43]. For clarity we review the salient features of this approach below. We assume infinite space boundary conditions in this discussion; Green's functions for semi-infinite and slab geometries have been reported in the literature [33-35] and do not qualitatively change the conclusions presented herein. The starting point for our treatment is the formal expression relating the scattered diffuse light field, Φ_{sc} , to a volume integral over

heterogeneities within the entire turbid medium [33]:

$$\Phi_{sc}(\mathbf{r}) = \int_V T(\mathbf{r}') G_0(\mathbf{r}, \mathbf{r}') d^3 r' . \quad (1)$$

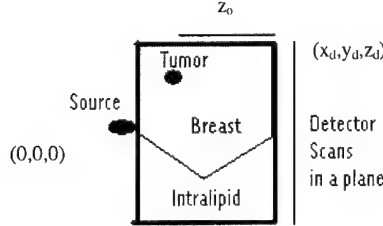


Figure 1. The generic near-field diffraction tomography experiment. The detector is scanned in a 2D grid on the surface of the plane parallel to and displaced from the plane containing the source. The breast is embedded in the box along with Intralipid in order to match its average optical properties.

Here $T(\mathbf{r}')$ is “tumor” function at position \mathbf{r}' which, in the Born Approximation, depends on the background diffuse photon density wave, $\Phi_0(\mathbf{r})$, as well as the absorption ($\delta\mu_a(\mathbf{r}')$) and scattering ($\delta\mu_s(\mathbf{r}')$) deviations from the medium’s background absorption (μ_{a0}) and scattering coefficients (μ_{s0}) respectively. $T(\mathbf{r}')$ also depends on the speed of light in the medium, v , the background light diffusion constant D_0 , the background diffuse photon density wavevector $k_0 = \sqrt{(-v\mu_{a0} + i\omega)/D_0}$, and the modulation frequency, ω . It can be conveniently separated into absorptive and scattering parts [49], i.e.,

$$T_{abs}(\mathbf{r}) = -\frac{v}{D_0} \Phi_0(\mathbf{r}) \delta\mu_a(\mathbf{r}) , \quad (2)$$

$$T_{sc}(\mathbf{r}) = \frac{3D_0 k_0^2}{v} \Phi_0(\mathbf{r}) . \quad (3)$$

Here we drop the gradient terms due to the scattering variations for simplicity. This approximation is described in detail in [49]. $G_0(\mathbf{r}, \mathbf{r}')$ is the usual Green’s function for the medium of the form:

$$G_0(\mathbf{r}, \mathbf{r}') = \frac{\exp(ik_0|\mathbf{r} - \mathbf{r}'|)}{4\pi|\mathbf{r} - \mathbf{r}'|} . \quad (4)$$

Typical experiments that employ the angular-spectrum representation for analysis use a “parallel-plate” geometry (e.g. fig.(1)) where the detected DPDW, $\Phi(\mathbf{r}) = \Phi_{sc}(\mathbf{r}) + \Phi_0(\mathbf{r})$, is measured at discrete points within a square grid on the planar output (detector plane, (x, y, z_d)) surface. We take our source (at the origin, $(0, 0, 0)$) to be a point emitter on the planar input surface (source plane, $(x_s, y_s, 0)$). In this geometry the Green’s function is conveniently written in the following form:

$$G_0(\mathbf{r}, \mathbf{r}') = \int \int dp dq \hat{G}_0(p, q, z_d, z') e^{-i(p(x_d - x') + q(y_d - y'))} , \quad (5)$$

where the z -axis is defined in the direction normal to the plane surfaces, and (p, q) are the 2D spatial (k-space) frequencies conjugate to the x - and y -coordinates. The angular spectrum (Weyl expansion) representation of the Green’s function is [31,50]

$$\hat{G}_0(p, q, z_d, z') = \frac{i}{2m} e^{im|z_d - z'|} , \quad (6)$$

where $m = \sqrt{k_0^2 - (p^2 + q^2)}$ is the complex propagator wavenumber and the imaginary part of m is positive, i.e. $\Im(m) > 0$. With these definitions, the 2D Fourier Transform of the scattered field in the detection plane is simply [33]

$$\hat{\Phi}_{sc}(p, q, z_d) = \int dz' \hat{G}_0(p, q, z_d, z') \hat{T}(p, q, z) . \quad (7)$$

where hat ($\hat{\cdot}$) indicates quantities in k-space. This equation is the fundamental equation for diffraction tomography.

2.2 Image reconstruction

Equation (7) relates the tumor function in each slice to the 2D Fourier Transform of the scattered DPDW in the detection plane. Rather than inverting the Laplace Transform directly, we discretize the integral into a sum over slices of thickness Δz , i.e

$$\hat{\Phi}_{sc}(p, q, z_d) = \sum_{j=1}^N \hat{G}_0(p, q, z_d, z_j) \hat{T}(p, q, z_j) = \sum_{j=1}^N \frac{i\Delta z}{2m} \hat{T}(p, q, z_j) e^{im(z_d - z_j)} . \quad (8)$$

Δz is the step size in the z-direction and $N = z_d/\Delta z$ is the total number of slices. This is the key equation for our image reconstruction using the angular-spectrum approach. There are a number of possible ways to solve this problem in 3D [36,40], but from this point onwards we focus on projection images and a 3D variant thereof.

For two dimensional projection images in the x-y planes along the depth direction (z), we assume that the inhomogeneities are isolated and thin, and we drop the sum. That is, we take the tumor function to be zero everywhere except at the phantom (object) depth. Thus a measurement, Fourier transform, and a simple division in the k-space yields the tumor function, i.e

$$\hat{T}(p, q, z_{obj}) = \frac{\Phi_{sc}(p, q, z_d)}{\Delta z \hat{G}_0(p, q, z_d, z_{obj})} , \quad (9)$$

where the subscript “obj” indicates the phantom coordinates.

The inverse Fourier transform of this quantity enables us to solve for absorption and scattering variations. Using

$$T(x', y', z_{obj}) = \iint dp dq \frac{e^{-i2\pi(px' + qy')}}{\Delta z \hat{G}(p, q, z_{obj}, z)} \iint dx dy e^{i2\pi(px' + qy')} \Phi_{sc}(x, y, z_d) , \quad (10)$$

we can solve eq. (2) and (3) to get $\delta\mu_a(\mathbf{r})$ and $\delta\mu'_s(\mathbf{r})$. Note that we need to know the background field at the object depth to accurately obtain optical properties. Fig.(2) is a flowchart illustrating the algorithm described above.

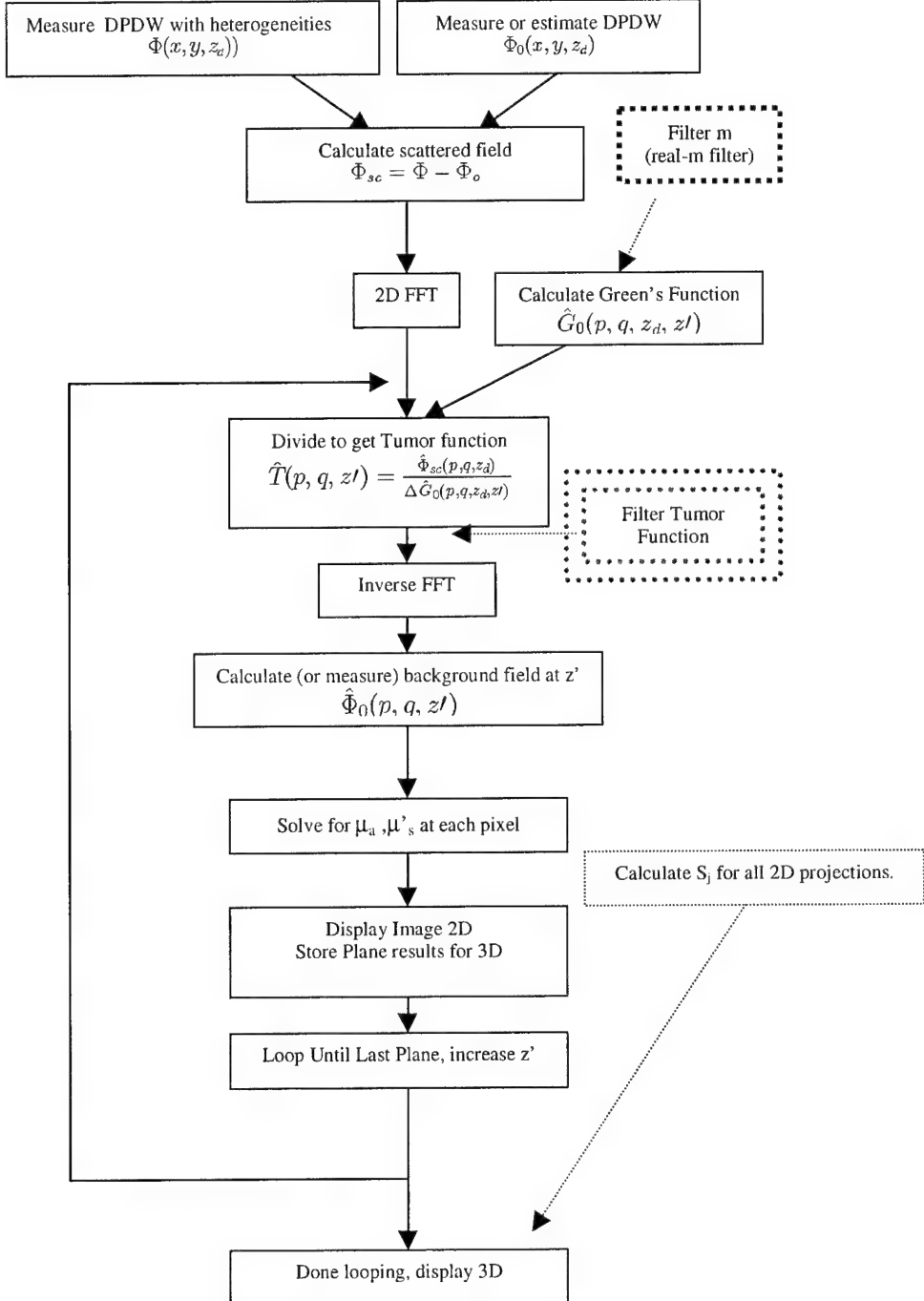


Figure 2. Simplified flow diagram of the image reconstruction algorithm. Dotted lines are used for optional steps. Brown and blue indicate real-m filtering, green indicates G-filtering steps.

The relevant clinical situation is shown in fig.(1). The breast is embedded in a slab-like box filled with matching material such as Intralipid. The optical properties of Intralipid are chosen to be close to the average optical properties of the breast. Illumination comes from one plane, and the detectors are scanned in a grid on the opposite

plane. The amplitude and phase of the DPSW's with and without the breast are measured and used to obtain the scattered DPDW. In our experiments [21,33,41] we also use multiple optical wavelengths to obtain spectroscopic information[41]. The background field at different depths is not measured and must be estimated using numerical models or a backpropagation technique [25,51]. This is the main difficulty for obtaining 3D information in clinical situations and we are investigating various methods to overcome this problem [33,34].

2.3 Noise amplification at high spatial frequencies

In eq.(9) we divide two waves with complex wavenumbers (m and k_0). The scattered field generally suffers from noise; the origin of this noise can be experimental, numerical, or due to finite sampling. The noise in the high spatial frequencies is preferentially amplified by the deconvolution because the Green's function in the denominator of equation (9) decays to zero faster for higher values of p and q . The amplification of the high frequency noise and the associated instabilities are common problems associated with Fourier convolution approaches to image reconstruction [25-28,44-46]. Fig.(3) demonstrates this problem.

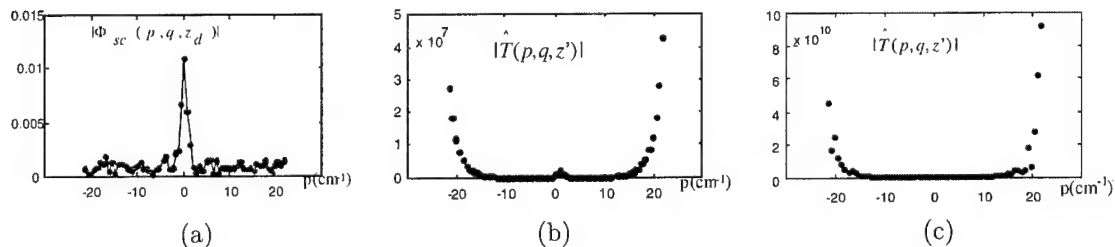


Figure 3. (a)Amplitude of the scattered wave as a function of p for a fixed q and (b) amplitude of the tumor function plotted in the k-space for noiseless (only numerical noise) and (c) noise-added data from the single object (sec. 5.1) . The maximum frequency, $|p| = \pi/\Delta x$. The rising “wings” on the sides are due to noise. The noise effects are amplified by $\approx 10^3$ relative to the noiseless case at large p .

One [37,38,41] way of dealing with this problem is to apply a low-pass spatial filter in order to suppress the high frequency components of the tumor function. The quantitative effects of this cut are not known however [41,45,46]. Furthermore, the spatial resolution of the images depend on the highest k-space frequencies available and therefore filtering modifies image resolution (see eq.(12))[31,41,43,44].

3. Filtering and normalization for improving depth information / image quality

We have investigated filtering and normalization techniques which provide different types of information and lead to the improvement of image quality within the context of projection imaging. In particular we have found a robust method which enables the experimenter to estimate the approximate depth of the heterogeneities below the detection plane; the method does not require more data, yet offers a prescription for extending the 2D projection approach to quasi-3D imaging and localization. In this section we briefly outline three techniques to optimize image reconstruction. In the remainder of the paper we demonstrate their utility. For simplicity we focus entirely on absorption heterogeneities.

3.1 Phase only Green's function (real-m filter)

We have found a very crude filtering technique that gives fairly accurate positional information in two- and even three-dimensional images. In essence the method is based on the hypothesis that most of the positional information is contained in the phase of our signals in k-space. In this procedure we modify the Green's function, $\hat{G}_0(p, q, z_d, z')$; in particular we put $\hat{G}_0(p, q, z_d, z') \approx ie^{i\Re(m)|z_d-z'|}$. We set its amplitude to unity, so only phase information in the Green's function is used for the reconstruction. We also apply a Blackman Window on \hat{T} (see [43] for its properties) which is a standard windowing function used in the Fourier domain to further stabilise the image. This last step is used for better image quality and is not an essential part of the algorithm. Calculation of the projection image proceeds along similar lines except for these steps (see fig. (2)). Although quantitative information about optical properties is largely lost, the real-m filter has no free parameters (except from the optional windowing function) and provides superior information about the xyz central coordinates of heterogeneities.

3.2 Depth estimation (S_j)

We have empirically found [52] that the following set of operations applied to the projection images obtained with the real-m filter enable us to accurately estimate the heterogeneity depth below the detection surface. Briefly, we first obtain the tumor function for each slice (centered on some z_j) using the real-m filter. We then derive an image of $\delta\mu_a(x, y, z_j)$ for each slice, determine the center position of the object we are trying to characterize, and record the absorption variation at the object central position. Finally we compute the quantity

$$S_j = \frac{|\delta\mu_a - \bar{\delta\mu}_a|}{\sqrt{\sum_{xy} (\delta\mu_{axy} - \bar{\delta\mu}_a)^2}} \quad (11)$$

where the sum in the denominator is over all pixels in the image slice. $\bar{\delta\mu}_a$ is the mean $\delta\mu_{axy}$ in the j^{th} plane. S_j is in essence a measure of the contrast of the object in the j^{th} plane. We empirically found that the value of z_j for which S_j is a maximum closely approximates the actual depth of the object (z_{obj}). This procedure enables us to select a slice for the projection image and, thus provides a scheme for extending images to three dimensions (see section 5.1 .1).

3.3 High frequency filtering based on depth and experimental noise floor (G-filtering)

After we have obtained this rough picture of the object in the turbid medium, we repeat the entire procedure using the true Green's function. From our discussion in section 2.3 however, it is apparent that we need to devise a scheme to select the spatial frequencies for reconstruction. We carry out this procedure in a straightforward way. Note that it is critical for this procedure that the scattered waves are normalized by the source strength. For our convenience we used a source strength of one photon per unit volume per unit time. We first plot the raw data to determine the experimental noise level. For example by plotting $\hat{\Phi}_{sc}$ vs. p and q (e.g. fig.(3)) we will find at sufficiently high p and q , that $\hat{\Phi}_{sc}$ hits a "white" noise floor; the ratio of the signal amplitude at $p = q = 0$ to the signal amplitude at these high frequencies provides a measure of the experimental signal-to-noise. Next we insert the estimated object depth $z' = z_{obj}$ into the expression for $\hat{G}_0(p, q, z_d, z')$, and we determine at what value of m , $\hat{G}_0(p, q, z_d, z_{obj})$ drops below a threshold based on our experimental S/N. In practice we set this threshold to be about five times the white noise floor. We set $\hat{T} = 0$ for all m greater than this threshold (see fig (2) for the occurrence of this step in the general algorithm.). The result is a depth

dependent pillbox filter applied to the tumor function. The rest of the reconstruction is the same. The combination technique offers the possibility of improvement in the accuracy of optical properties and better images.

At this point it may also be desirable to recompute S_j using reconstructions based on the G-filter technique. Usually the maximum S_j determined with the G-filter is within ≈ 1 cm of the maximum S_j determined using the real-m filter (see section 3.1). In applying this latter procedure the high frequency cut-off depends on depth (z_j).

4. Data generation

Our “data” was derived from numerical simulations. In particular the finite difference method with partial current boundary conditions was used to solve the diffusion equation for arbitrary interior inhomogeneities. The program is capable of simulating the forward problem in a box geometry. We used a point source with a strength of one photon per unit volume per unit time; this choice of source term eliminated the need to normalize the scattered wave when computing the noise floor and comparing the threshold to the Green’s function. The source was modulated at 140Mhz. For the purposes of this paper we simulate data in a 20x20x20cm box and use the central 9x9x5cm region for “experiments”. The region is far from all boundaries and is a very good approximation to the infinite medium. The region created from the simulation is a 65 by 65 by 36 grid in x, y and z with the coordinates respectively, running from -4.5 to 4.5cm in x & y and 0 to 5 cm in z directions. The step size is 0.14cm corresponding to a voxel size of (0.14cm)³. The geometry chosen closely mimics our clinical set-up [34,41]. We use a high number of pixels in the numerical simulation to avoid truncation errors. Each point of the detection grid is centered in the squares of the same 65x65 region in the detector plane at $z_j = z_d = 5$ cm.

Optical properties can be assigned to each pixel independently so that we are able to simulate heterogeneities of arbitrary shape. We use thin rectangular slices (i.e thin in z-direction) for objects. Thin slices insure that our projection approximation is reasonable. Figs. (4) and (8) provide 3D renderings of the input phantoms.

Noise is added to the data using a random number generator with a normal distribution of variance one and mean zero. The approach is tuned to provide gaussian noise with variance 0.5% for the amplitude and variance of 0.05° for the phase. These probably overestimate our experimental noise. Noise is added to heterogeneous and homogeneous measurements. Figs.(4) and (12) show the amplitude of the noiseless and noisy scattered fields obtained in Born approximation.

5. Results

5.1 Tissue phantoms with single slice heterogeneity

The simulated heterogeneity is shown in fig.(4). It has dimensions 1.4 x 1.4 x 0.28 cm in x,y and z directions respectively. The optical properties are $\mu_a = 0.1 \text{ cm}^{-1}$ and $\mu'_s = 8 \text{ cm}^{-1}$. The background optical properties are $\mu_{ao} = 0.02 \text{ cm}^{-1}$ and $\mu'_{so} = 8 \text{ cm}^{-1}$. The phantom is centered at a depth of 2.65cm from the source plane. It’s transverse location centers on y=x=1.97cm. The amplitude of the “measured” scattered field at the detector plane is shown in its noiseless and noisy versions in fig.(4) for comparison.

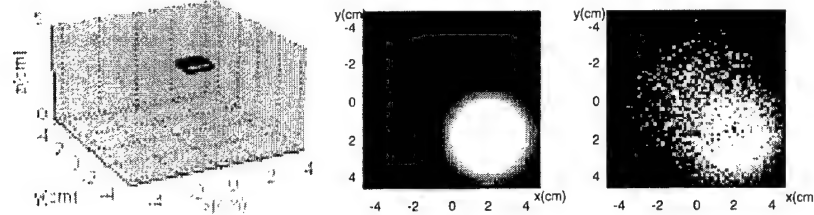


Figure 4. Single Slice Phantom: Left figure shows a 3D rendering of the phantom. Gray region has background properties. The detector plane is assumed to be at $z=5\text{cm}$ and the source is at the origin in $z=0\text{cm}$ plane. Amplitude of the scattered field in the detector plane for the phantom shown in the middle (noiseless) and right (noise added) figures.

5.1 .1 Real-m imaging

We now employ the real-m filter scheme described in section 3.1 on the single object data shown above. Figs.(5a) and (5b) show two dimensional projection images at depths $z=2.42\text{cm}$ and $z=3.24\text{cm}$ respectively. We see that the object is clearly apparent. In fig. (5c), we plot S_j vs z_j ; we see that the contrast parameter is peaked at $z_j = 2.71\text{cm}$, and we use this value to make a “true” real-m filter reconstruction of the data which is shown in fig.(5d). This result is representative of all of the single-object phantoms that we tested.

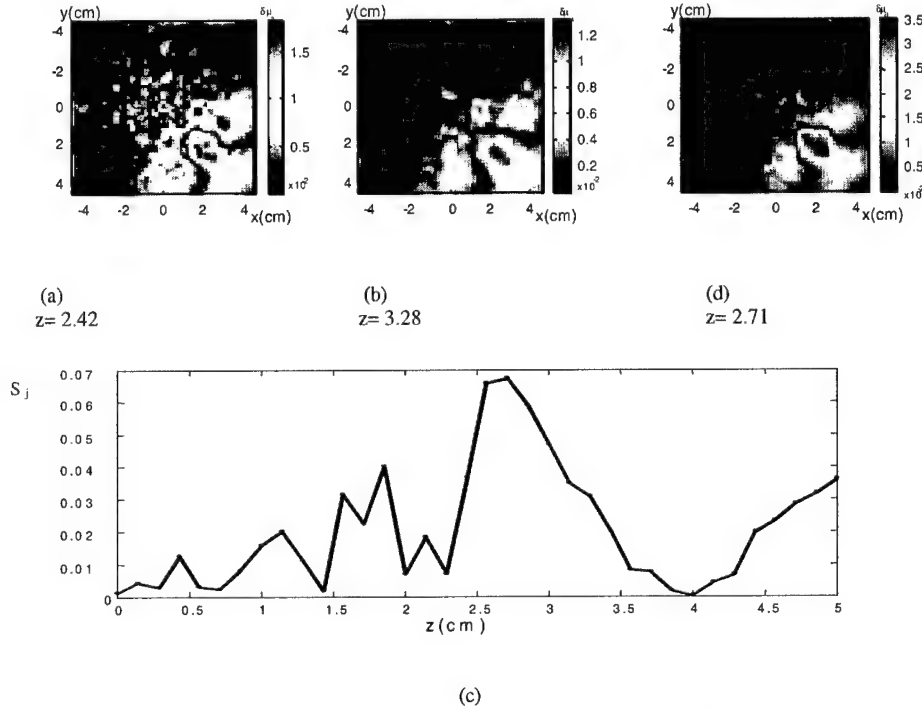


Figure 5. (a) and (b) projections at $z=2.42$, $z=3.28$ respectively, (c) S_j vs z_j (cm) through the transverse center, peaks at $z=2.71$, (d) projection at $z=2.71$. All with real-m filter.

Although most of the information about optical properties is lost, the 3D local-

ization of single objects is quite good. The slices with the greatest noise are either near the detection or source planes. The issue of multiple objects at different depths will be addressed later in this paper.

5.1 .2 G-filter imaging

Next we use the combination scheme described in section 3.3 to reconstruct the single object data. Our experimental noise threshold was 3×10^{-3} for all cases. For $z_j = 2.71\text{cm}$, the G-filter was set for $p=q=1.01/\text{cm}$ at maximum, and the resulting image in this plane is shown in fig.(6a) . Notice that the image is a little cleaner than the real-m image with most of the artifacts from the characteristic ringing near the corners of the reconstructed volume. The optical properties (although still not accurate for such a deep object) are more reasonable.

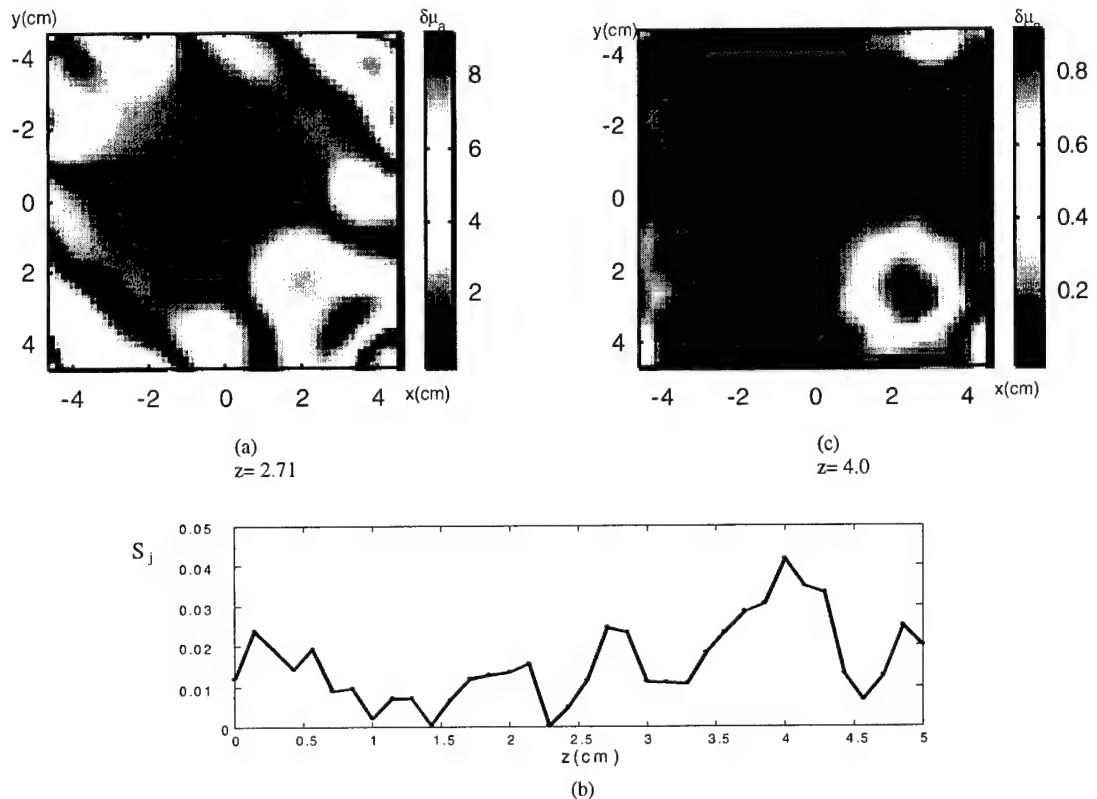


Figure 6. (a) projection at $z=2.71$ at real-m peak, (b) S_j vs z_j (cm) through the transverse center peaks at $z=4\text{cm}$, (c) projection at $z=4.0$. All obtained with G-giltering.

We next computed S_j vs z_j using the G-filter (see fig.(6b)). Notice that the peak value of S_j has shifted from its true value. The G-filter image (at $p=q=2.36/\text{cm}$) based on this new z_j is shown in fig.(6c); we see that the image is sharper and has better optical properties. This is very important for multiple wavelength images as we observe that the ratio of reconstructed optical properties is fairly well approximated by this technique. However, its actual location is systematically shifted away from its true value. At present we do not fully understand the origin of this systematic error in a deep way. We find that this shift is related to the amount of power cut out by the filter. By changing the filter spatial frequency cut-off to a lower frequency (increasing

the threshold) we find that the shift is increased but the optical properties at the shifted location however approach their correct values.

Finally we note that since the maximum spatial frequencies used in the G-filter approach depend on object depth, we can expect our resolution to decrease with increasing object-detector separation. Following Pattanayak [31] our approximate experimental resolution, L , depends on the maximum allowable p and q , i.e

$$p_{max}^2 + q_{max}^2 = \left(\frac{2\pi}{L}\right)^2. \quad (12)$$

In fig.(7) we show the change in resolution with depth assuming our experimental S/N threshold. While the exact numerical values depend on approximations in [31], the important qualitative effect to note is that the resolution improves dramatically for objects near the detection plane.

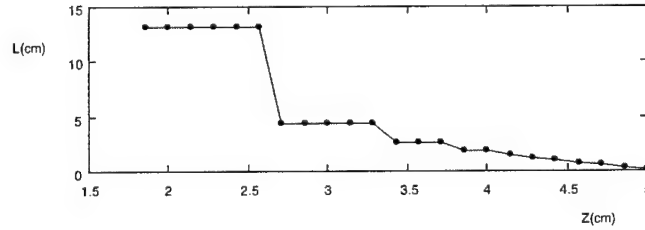


Figure 7. Estimate of resolution(cm) vs distance from source plane (cm) . The changing depth dependent cut-off frequency results in the increase in resolution with distance from source plane (i.e decrease in resolution with depth from the detector plane).

5.2 Tissue phantoms with two slice heterogeneities / three dimensional renderings

We now simulate two objects with same dimensions and optical properties but in a more complicated geometry where in principle the scattered waves from one heterogeneity could effect the other. One object is centered at 3.07cm deep with its transverse center at $x=y=1.97$ cm and the other object is 4.35cm deep with its transverse center at $x=y=-1.97$ cm as shown in fig.(8). The amplitude of the “measured” scattered field at the detector plane is shown in its noiseless and noisy version in fig.(8) for comparison.

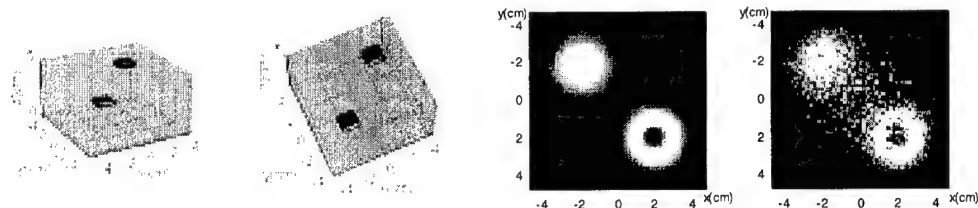


Figure 8. Two slice Phantoms: Two leftmost figures show 3D renderings. Gray region has background properties. The detector plane is at $z=5$ cm and the source is at the origin in $z=0$ cm plane. Amplitude of the scattered field at the detector plane is shown in the two rightmost figures. The left is the noiseless data and the right shows the data after adding noise.

We performed essentially the same set of reconstruction procedures as described in sections 3. and 5.1 . In fig.(9a) we show that S_j has two maxima in different planes depending on the heterogeneity under consideration using real-m filter. Note that the real-m images were more noisy by comparison to the single object phantom. We again

find that the optical properties are most accurate where S_j has its shifted maxima with the G-filter. These images are shown in Fig (9b,c). Absolute values are closer to the real values for shallow objects and the positional shift also depends on the depth.

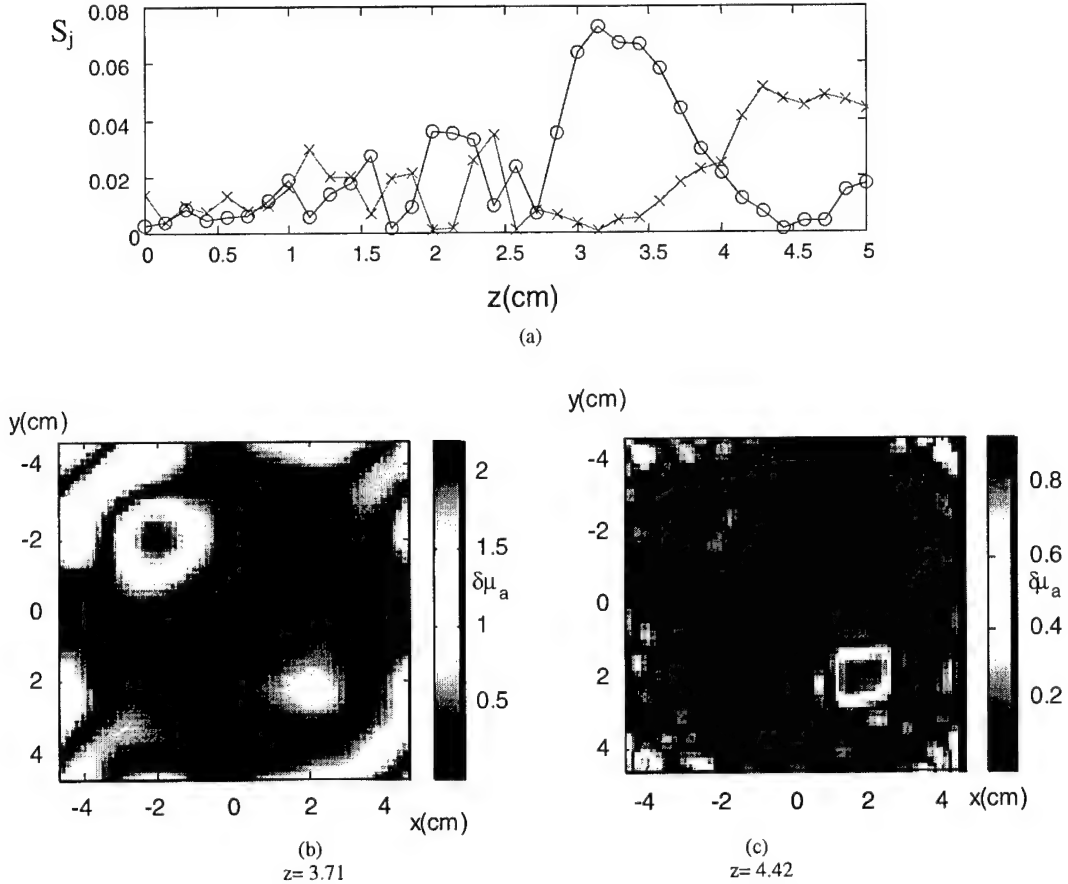


Figure 9. (a) Circles (crosses) show S_j vs z_j (cm) through the center region of deeper (shallower) object obtained with m-filter. Peak for both objects are exact. Then with G-filter we get projections at (b) $z=3.71$ and (c) at $z=4.41$.

Finally, by calculating S_j at all the voxels we can generate three dimensional images of the entire reconstructed volume. That is, for each of the 36 projections we calculate the value of S_j for all transverse pixels ($65 \times 65 = 4225$ values in each projection) and plot all S_j 's in three dimensions. In fig.(10a) and (10b) we show an isosurface rendering at value $S_j = 0.042$ at two viewing angles. Two dimensional projections in plane $y=2\text{cm}$ and plane $y=-2\text{cm}$ are also shown in fig. (10c) and fig.(10d) to provide a better sense of contrast. Comparing this to fig.(8) we see that the shallow object is very well reconstructed both in terms of shape and location. The deeper object has lower resolution and is shifted from its original location. In the corners we see the characteristic ringing effects from Fourier domain reconstructions. These latter artifacts, however, are usually fairly easy to identify. We find that, even when the objects are close to the image edges we are capable of separating objects from ringing artifacts. We are investigating presently whether it is possible to extract any quantitative or qualitative optical property information from these images.

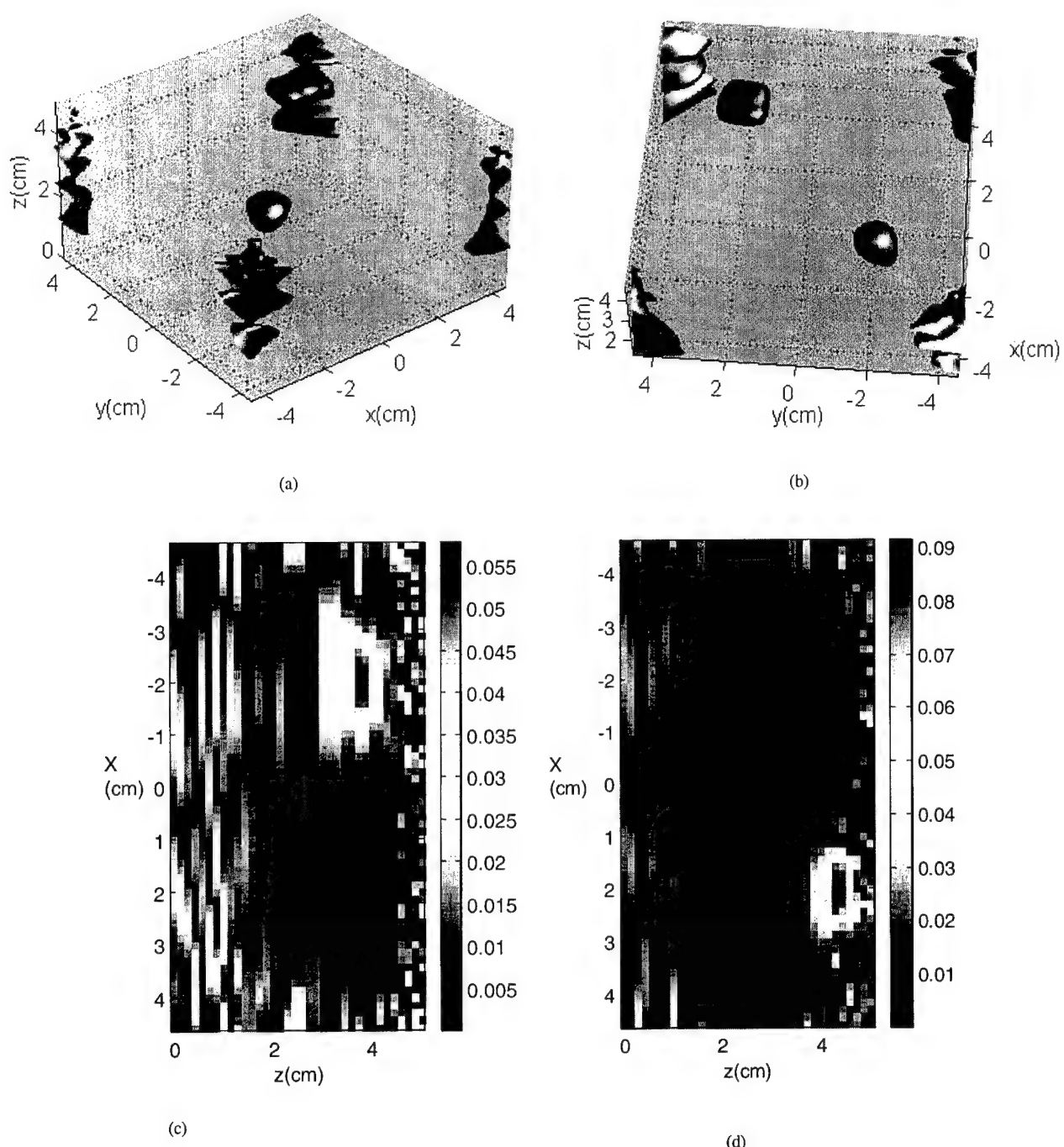


Figure 10. Three Dimensional Rendering of the G-filter reconstruction. An isosurface at $S_j = 0.042$ is shown in two different angles in (a) and (b). In (c) and (d) images of S_j in x-z plane through $y=2\text{cm}$ and $y=-2\text{cm}$ are shown respectively. Compare the results to that of fig.(8)

6. Conclusion

We have studied projection images of turbid media based on the angular-spectrum representation. We demonstrated two filtering schemes. One of them, the real-m filter, provided object location information with no free parameters; the other method, the G-filter, introduced a systematic approach for eliminating high spatial frequencies from the reconstructions. Image localization in 3D was demonstrated using both filters by maximizing the object signal-to-noise (S_j) on a slice-by-slice basis. Despite these successes, some image artifacts remain and must be addressed in future work. These include: noise near the detection plane and image boundaries, systematic shifts of the object location depending on filtering schemes and noise floors, and optical property accuracy.

Acknowledgements

We gratefully acknowledge useful conversations with Hanli Liu, D. A. Boas and C. L. Matson. A.G. Y. and D. N. P. acknowledge partial support from US Army RO DAMD17-97-1-7272 and NIH 1-RO1-CA75124-01 grants respectively.

Near-field Diffraction Tomography with Diffuse Photon Density Waves

Xingde Li^{* *}, Deva N. Pattanayak^{†§}, Turgut Durduman[†], Joseph P. Culver[†],
Britton Chance^{*} and Arjun G. Yodh[†]

[†]*Department of Physics and Astronomy, *Department of Biochemistry and Biophysics
University of Pennsylvania, Philadelphia, PA 19104*

[§]*Silicon Power Corporation, 3 Northway Lane North, Latham, NY 12110*

(August 14, 1999, Version 4)

Abstract

An angular spectrum algorithm is presented for fast, near-field diffraction tomographic imaging with diffuse photon density waves in highly scattering media. A general relation in K-space is derived that connects the spatial variations of the optical properties of heterogeneities to the spatial spectra of the measured scattered diffuse photon density waves. The theory is verified experimentally for situations when boundary effects can be neglected. We further describe how to incorporate boundary conditions into this angular spectrum algorithm for a turbid medium of finite size, the slab medium. Limitations and potential improvements of the near-field diffraction tomography are also discussed.

*Xingde Li is now with the Department of Electrical Engineering and Computer Science, Massachusetts Institute of Technology, Cambridge, MA 02139. When this work was performed, he was with the University of Pennsylvania. His current email address is *xingde@mit.edu*

I. INTRODUCTION

Optical radiation was used to image breast tumors by the shadowing effect as early as the 1920's [1]. However, recent advances in light generation and detection, along with improvements in our theoretical understanding of near infrared (NIR) light propagation in tissue-like highly scattering turbid media have opened new possibilities for optical imaging of the interior of thick biological tissues [2]. In highly scattering media such as biological tissue, light propagation is described adequately within the diffusion model of photon transport [3–5]. It has been shown by several investigators that diffuse photon density waves, which are created inside highly scattering media by an intensity modulated light source, obey a Helmholtz wave equation with a complex wave number [6,7]. In spite of the complexities resulting from strong tissue scattering, the new modality with diffusing photons offers many attractive features for imaging thick tissue. These features include non-invasiveness, low cost, and unique optical contrast and spectroscopic signatures with clinical and physiological relevance [8,9].

The goal of optical imaging with diffusive photon density waves is to reconstruct a low resolution map of the heterogeneous absorption and scattering properties from the measurements of diffuse photons on the sample surface or within the sample. Image reconstruction entails solving the inverse problem. Most quantitative optical image reconstruction algorithms such as the Algebraic Reconstruction Technique (ART) and the Spontaneous Iterative Reconstruction Technique (SIRT) [10], the Newton-Raphson technique combined with finite element numerical method [11–13], the Conjugate Gradient Descent technique [14], and the Singular Value Decomposition (SVD) [15], rely on iterative schemes in a least-square sense. The optical image reconstruction therefore requires a significant amount of computational resources and time.

Recently, we showed that by essentially following the techniques of diffraction tomography [16,17], it is possible to rapidly reconstruct thin slice and spherical objects whose absorption and/or scattering parameters differ from the background homogeneous scattering medium [18]. The image reconstruction algorithm employing the diffraction tomography

technique (called angular spectrum algorithm in this paper) is rapid, permitting object localization and characterization in ~ 1000 volume-element samples on sub-second computational time scales. The primary purpose of this paper is to provide a more complete discussion of the results reported in those earlier papers. In addition, we will provide detailed analysis of this algorithm incorporating the effects of finite boundaries. We will first derive the general integral solution of the total and scattered photon density waves in a heterogeneous turbid medium within the first order Born approximation (Section II, III and IV). We next derive a relation in K-space between the spatial spectrum of the heterogeneity function and the spatial spectrum of the measured scattered diffuse photon density wave (Section V (A)). Experimental results are presented to verify the feasibility of the angular spectrum algorithm for image reconstruction. Some limitations and potential improvements of the diffraction tomography are also discussed (Section VI). Finally we present a discussion about how to incorporate boundary conditions into this angular spectrum algorithm for a turbid medium of finite size, in particular, the slab medium and the semi-infinite medium (Section VII).

II. PHOTON DIFFUSION EQUATION IN HETEROGENEOUS MEDIA - A PERTURBATION APPROACH

Light transport in highly scattering turbid media is often well described by photon diffusion [2]. Consider a light source at \mathbf{r}_s with its intensity sinusoidally modulated at modulation frequency f , e.g., the source term is $S(\mathbf{r}, t) = S(\mathbf{r})e^{-i\omega t} = M_0 e^{-i\omega t}\delta(\mathbf{r} - \mathbf{r}_s)$, where $\omega = 2\pi f$ is the angular source modulation frequency¹, M_0 is the source strength representing the number of photons emitted per second. Consider steady state photon diffusion in which the photon fluence $\Phi(\mathbf{r}, t)$ has the same time dependence as the source, i.e., $\Phi(\mathbf{r}, t) = \Phi(\mathbf{r})e^{-i\omega t}$. It is straight forward to show that the photon fluence $\Phi(\mathbf{r})$ satisfies the photon diffusion

¹The continuous-wave (CW) case is a special case where $\omega = 0$ and the frequency domain analysis can be readily applied to the CW case.

equation [3–5]:

$$\nabla \cdot (D \nabla \Phi(\mathbf{r})) - v\mu_a \Phi(\mathbf{r}) + i\omega \Phi(\mathbf{r}) = -vS(\mathbf{r}) . \quad (1)$$

Here the common time dependence $\exp(-i\omega t)$ of the fluence $\Phi(\mathbf{r})$ and the source $S(\mathbf{r})$ are omitted. v is the speed of light in the turbid medium; $D = \frac{v}{3\mu'_s}$ is photon diffusion coefficient; μ_a and μ'_s are respectively the optical absorption and reduced scattering coefficients. Since $\nabla \cdot (D \nabla \Phi) = D \nabla^2 \Phi + \nabla D \cdot \nabla \Phi$ and $\nabla D = \nabla \frac{v}{3\mu'_s} = -\frac{v}{3\mu'_s} \frac{\nabla \mu'_s}{\mu'_s}$, Eq. (1) can be rewritten as

$$\nabla^2 \Phi(\mathbf{r}) + 3\mu'_s \left(\frac{-v\mu_a + i\omega}{v} \right) \Phi(\mathbf{r}) - \frac{\nabla \mu'_s}{\mu'_s} \cdot \nabla \Phi(\mathbf{r}) = -3\mu'_s S(\mathbf{r}) . \quad (2)$$

In a homogeneous medium, the absorption and scattering coefficients (μ_{a0} and μ'_{s0}) are constant, and the above equation reduces to a simple Helmholtz equation:

$$(\nabla^2 + k_0^2) \Phi_0(\mathbf{r}) = -3\mu'_{s0} S(\mathbf{r}) . \quad (3)$$

Here the wave number k_0 is complex and $k_0 = [3\mu'_s (\frac{-v\mu_a + i\omega}{v})]^{1/2}$ with $Im(k_0) > 0$ to ensure that the photon density goes to zero at a large distance. The simplest solution of this Helmholtz equation shows that photons propagate collectively as a damped spherical wave outward from the source, i.e., $\Phi_0(\mathbf{r}) \propto \frac{\exp(ik_0|\mathbf{r}-\mathbf{r}_s|)}{4\pi|\mathbf{r}-\mathbf{r}_s|}$.

In an optically heterogeneous turbid medium, the spherical wave-fronts of the homogeneous incident wave are distorted by inhomogeneities and scattered waves are produced. The concept of the scattered wave is illustrated in Fig. 1. The total photon density wave $\Phi(\mathbf{r})$ is the sum of the incident wave $\Phi_0(\mathbf{r})$ and the scattered wave $\Phi_{sc}(\mathbf{r})$:

$$\Phi(\mathbf{r}) = \Phi_0(\mathbf{r}) + \Phi_{sc}(\mathbf{r}) . \quad (4)$$

This formalism is not limited to an infinite geometry. In general the incident wave $\Phi_0(\mathbf{r})$ corresponds to the photon density wave in a homogeneous turbid medium for an arbitrary geometry, and we interchangeably use another name – “background photon density wave” – for $\Phi_0(\mathbf{r})$; the scattered wave $\Phi_{sc}(\mathbf{r})$ represents the perturbation of the incident wave in the presence of inhomogeneities for the same geometry. The scattered wave is determined by

characteristics of the inhomogeneity such as its size, shape, position and its absorption and scattering properties. The goal of optical tomography is to reconstruct the map of these heterogeneous optical properties from measurements of the scattered wave. We first derive the photon diffusion equation obeyed by the total photon density wave within the first order Born Approximation.

In a heterogeneous medium we write the optical properties (μ_a and μ'_s) as the sum of background optical properties (μ_{a0} , μ'_{s0}) and the variations relative to the background ($\delta\mu_a$, $\delta\mu'_s$), i.e.

$$\mu_a = \mu_{a0} + \delta\mu_a , \quad (5)$$

$$\mu'_s = \mu'_{s0} + \delta\mu'_s . \quad (6)$$

We consider the case of weak optical inhomogeneities where $\delta\mu_a \ll \mu_{a0}$ and $\delta\mu'_s \ll \mu'_{s0}$. The optical inhomogeneities introduce a weak perturbation to the incident wave, i.e., $|\Phi_{sc}(\mathbf{r})| \ll |\Phi_0(\mathbf{r})|$. Substituting Eqs. (5) and (6) into Eq. (2) and keeping only the zeroth and first order terms in optical property variations (i.e. $\delta\mu_a$, $\delta\mu'_s$) as well as in the scattered wave ($\Phi_{sc}(\mathbf{r})$), we find

$$(\nabla^2 + k_0^2)\Phi(\mathbf{r}) = -\frac{v}{D_0}[1 + \frac{\delta\mu'_s(\mathbf{r})}{\mu'_{s0}}] S(\mathbf{r}) - T_{abs}(\mathbf{r}) - T_{sc}(\mathbf{r}) , \quad (7)$$

where we have introduced the heterogeneity functions $T_{abs}(\mathbf{r})$ and $T_{sc}(\mathbf{r})$ representing the perturbations due to the absorption and scattering variations. They are

$$T_{abs}(\mathbf{r}) = -\frac{v}{D_0}\Phi_0(\mathbf{r}) \delta\mu_a(\mathbf{r}) , \quad (8)$$

$$T_{sc}(\mathbf{r}) = \frac{3D_0k_0^2}{v}\Phi_0(\mathbf{r}) \delta\mu'_s(\mathbf{r}) - \frac{\nabla[\mu'_{s0} + \delta\mu'_s(\mathbf{r})]}{\mu'_{s0}} \cdot \nabla\Phi_0(\mathbf{r}) . \quad (9)$$

Here $D_0 = \frac{v}{3\mu'_{s0}}$ is the background photon diffusion coefficient; $k_0 = [(-v\mu_{a0} + i\omega)/D_0]^{1/2}$ is the wavenumber of the incident diffuse photon density wave $\Phi_0(\mathbf{r})$. Note that $\frac{\delta\mu'_s(\mathbf{r})}{\mu'_{s0}} S(\mathbf{r})$ in the first term on the right-hand side of Eq. (7) is zero as long as the source is outside the inhomogeneity (which is generally the case in practice), and therefore we can drop this term from Eq. (7). In addition we assume, for simplicity, that the scattering varies slowly in

space and the second term in Eq. (9) $\frac{\nabla[\mu'_{a0} + \delta\mu'_a(\mathbf{r})]}{\mu'_{a0}} \cdot \nabla\Phi_0(\mathbf{r})$ can then be neglected. We thus have the following simplified equation within the first order Born Approximation:

$$(\nabla^2 + k_0^2)\Phi(\mathbf{r}) = -\frac{v}{D_0} S(\mathbf{r}) - T(\mathbf{r}) , \quad (10)$$

where $T(\mathbf{r}) = T_{abs}(\mathbf{r}) + T_{sc}(\mathbf{r})$ and the heterogeneity functions $T_{abs}(\mathbf{r})$ and $T_{sc}(\mathbf{r})$ are given by

$$T_{abs}(\mathbf{r}) = -\frac{v}{D_0}\Phi_0(\mathbf{r})\delta\mu_a(\mathbf{r}) \quad (11)$$

$$T_{sc}(\mathbf{r}) = \frac{3D_0k_0^2}{v}\Phi_0(\mathbf{r})\delta\mu'_s(\mathbf{r}) \quad (12)$$

We see that the heterogeneity functions due to the optical inhomogeneities can be treated as equivalent "source" terms which give rise to the scattered component $\Phi_{sc}(\mathbf{r})$ of the total diffuse photon density wave $\Phi(\mathbf{r})$.

III. TOTAL DIFFUSE PHOTON DENSITY WAVE IN HETEROGENEOUS TURBID MEDIA — THE GREEN'S FUNCTION APPROACH

We will take a Green's function approach to derive the total and therefore the scattered photon density wave in a heterogeneous highly scattering medium. Consider the Green's function in turbid media which satisfies

$$(\nabla^2 + k_0^2)G(\mathbf{r}, \mathbf{r}') = -\delta(\mathbf{r}, \mathbf{r}') , \quad (13)$$

where $k_0 = [(-v\mu_{a0} + i\omega)/D_0]^{1/2}$ is the wavenumber of the incident photon density wave (the same as in Eq. (10)). Using the Green's theorem, we obtain an integral expression for the total optical density wave $\Phi(\mathbf{r})$:

$$\begin{aligned} \Phi(\mathbf{r}) &= \frac{v}{D_0} \int_V S(\mathbf{r}') G(\mathbf{r}, \mathbf{r}') d^3 r' + \int_V T(\mathbf{r}') G(\mathbf{r}, \mathbf{r}') d^3 r' \\ &\quad + \int_S [G(\mathbf{r}, \mathbf{r}') \frac{\partial\Phi(\mathbf{r}')}{\partial n'} - \Phi(\mathbf{r}') \frac{\partial G(\mathbf{r}, \mathbf{r}')}{\partial n'}] dA' . \end{aligned} \quad (14)$$

The first term on the right-hand side of Eq. (14) is a volume integral of the light source over the entire turbid medium. It gives us the incident wave. The second term is a volume

integral of the heterogeneity function over the entire turbid medium and it determines the perturbation resulting from the optical heterogeneities. The third term is a surface integral over the closed surface of the entire turbid medium. It takes into account the boundary effects on the total photon density wave, and it includes contributions to the total photon density wave from both the incident wave and the scattered wave on the boundary. n' in the surface term denotes the surface normal pointing outward. For an infinite heterogeneous medium, this surface term is zero since the enclosure surface of an infinite medium is at infinity. Therefore the scattered wave can be simply separated from the incident wave. For a finite turbid medium, however the separation of the incident wave component from the scattered wave component in the surface term is generally difficult. It is advantageous therefore to remove the surface integral from the total photon density wave by choosing an appropriate Green's function. We will consider this complicated (yet more realistic) case at the end of this paper. We will start with a simple case - the infinite geometry case.

IV. SCATTERED WAVE IN INFINITE HETEROGENEOUS TURBID MEDIA

As shown in Fig. 1, in the presence of optical heterogeneities, the total photon density wave consists of the incident wave and the scattered wave, and the scattered wave carries the information of the optical inhomogeneities. Starting with Eq. (14), we can easily find the relation between the scattered wave $\Phi_{sc}(\mathbf{r})$ and optical inhomogeneities, for example through the heterogeneity function $T_{obs}(\mathbf{r})$ and $T_{sc}(\mathbf{r})$. For an infinite geometry, the surface integral in Eq. (14) disappears. The incident wave in this case is given by the first term (volume integral of the source) on the right-hand side of Eq. (14). For an infinite geometry, the Green's function $G_0(\mathbf{r}, \mathbf{r}')$ which satisfies Eq. (13) is [19]

$$G_0(\mathbf{r}, \mathbf{r}') = \frac{\exp(ik_0|\mathbf{r} - \mathbf{r}'|)}{4\pi|\mathbf{r} - \mathbf{r}'|}. \quad (15)$$

Using this Green's function and considering an infinite medium with a point source at \mathbf{r}_s , i.e., $S(\mathbf{r}') = M_0\delta(\mathbf{r}' - \mathbf{r}_s)$, we can readily obtain the incident wave, i.e.

$$\Phi_0(\mathbf{r}) = \frac{v}{D_0} \int_{-\infty}^{\infty} d^3 r' M_0 \delta(\mathbf{r}' - \mathbf{r}_s) \frac{\exp(ik_0 |\mathbf{r} - \mathbf{r}'|)}{4\pi |\mathbf{r} - \mathbf{r}'|} = \frac{v M_0 \exp(ik_0 |\mathbf{r} - \mathbf{r}_s|)}{4\pi D_0 |\mathbf{r} - \mathbf{r}_s|}, \quad (16)$$

where M_0 is number of photons emitted from the source per second. We see that this incident wave is of course the same as the one obtained by directly solving the Helmholtz Equation. The scattered wave (by definition) is the difference between the total photon density wave $\Phi(\mathbf{r})$ and the incident wave $\Phi_0(\mathbf{r})$, which is related to the volume integral of the heterogeneity function, i.e.

$$\Phi_{sc}(\mathbf{r}) = \Phi(\mathbf{r}) - \Phi_0(\mathbf{r}) = \int_V T(\mathbf{r}') G_0(\mathbf{r}, \mathbf{r}') d^3 r' \quad (17)$$

V. IMAGE RECONSTRUCTION ALGORITHM AND EXPERIMENTAL RESULTS

The scattered wave depends on the heterogeneity function. In practice the scattered wave can be obtained from measurements and the knowledge of the incident wave. Given the scattered wave, how can one obtain the heterogeneity function and thus $\delta\mu_a(\mathbf{r})$ and $\delta\mu'_s(\mathbf{r})$? The approach we take here employs the angular spectrum analysis of the scattered wave. In this approach we relate the spatial spectrum of the scattered wave to the spatial spectrum of the heterogeneity function. The basic ideas are similar to those of diffraction tomography [16]. The analysis involves forward and inverse Fourier transforms following the conventions given in Appendix A.

A. The Angular Spectrum Algorithm

The detection geometry we consider for the angular spectrum algorithm is a 2-D planar geometry. As shown in Fig. 2, the scattered wave $\Phi_{sc}(\mathbf{r})$ is determined at a plane $z = z_d$ from a set of measurements in that plane. Eq. (17) tells us that the scattered wave $\Phi_{sc}(\mathbf{r})$ is the convolution of the heterogeneity function $T(\mathbf{r})$ with the Green's function $G_0(\mathbf{r}, \mathbf{r}')$. In order to reveal the relation between the scattered wave and the heterogeneity function in

K-space, we first expand the Green's function in terms of plane waves in two-dimensions, i.e.

$$\begin{aligned} G_0(\mathbf{r}_d, \mathbf{r}') &= \iint_{-\infty}^{+\infty} dp dq \tilde{G}_0(p, q, z_d, z') e^{-i2\pi[p(x_d-x')+q(y_d-y')]} \\ &= \iint_{-\infty}^{+\infty} dp dq \frac{i}{2m} e^{im|z_d-z'|} e^{-i2\pi[p(x_d-x')+q(y_d-y')]} , \end{aligned} \quad (18)$$

where (p, q) are the 2-D spatial frequencies with respect to the x-y coordinates. In the second line of the above equation, we have employed the Weyl expansion of the Green's function [20], i.e.

$$\hat{G}_0(p, q, z_d, z') = \frac{i}{2m} e^{im|z_d-z'|} , \quad (19)$$

where $m = [k_0^2 - (2\pi)^2(p^2 + q^2)]^{1/2}$ and $Im(m) > 0$. The derivation of the Weyl expansion of the Green's function is given in Appendix B.

Note that Eq. (18) is the *angular spectrum* representation of the Green's function, a solution of the wave equation with a point source at (x', y', z') (see Eq. (15)). At any point inside the half space to the right (or left) of the source, there are eigen-plane waves in the x-y plane whose amplitudes and phases vary with the distance from the source $|z_d - z'|$. Because of the large positive imaginary part of m , the amplitude decays exponentially versus the perpendicular distance $|z_d - z'|$ away from the source point. Plane waves with large spatial frequencies (p, q) (and therefore a large imaginary part of m) will have negligible amplitudes. This is the characteristic difference between diffuse photon density waves and ordinary diffractive electromagnetic waves in lossless dielectric media. These plane waves will be scattered by optical inhomogeneities and their resulting amplitudes and phases will carry information about the absorption and/or scattering characteristics of the inhomogeneities.

If we substitute the angular spectrum representation of the Green's function (Eq. (18)) into the volume integral of the scattered wave given by Eq. (17), after simple algebraic manipulation and interchanging the order of integrations, we obtain the following representation, known as the *angular spectrum* representation of the scattered wave:

$$\Phi_{sc}(\mathbf{r}_d) = \iint_{-\infty}^{+\infty} dp dq e^{-i2\pi(px_d+qy_d)} \int dz' \hat{G}_0(p, q, z_d, z') \hat{T}(p, q, z') , \quad (20)$$

where $\hat{T}(p, q, z')$ is the 2-D spatial spectrum (Fourier transform) of the heterogeneity function, i.e.

$$\hat{T}(p, q, z') = \iint_{-\infty}^{+\infty} dx' dy' T(x', y', z') e^{i2\pi(px'+qy')} . \quad (21)$$

Taking the 2-D Fourier transform of the scattered wave $\Phi_{sc}(\mathbf{r}_d)$ in the detection plane at $z = z_d$, i.e.,

$$\Phi_{sc}(\mathbf{r}_d) = \iint_{-\infty}^{+\infty} dp dq \hat{\Phi}_{sc}(p, q, z_d) e^{-i2\pi(px_d+qy_d)} , \quad (22)$$

and comparing Eq. (20) and Eq. (22), we then obtain the relation between the spatial spectrum of the scattered wave and the spatial spectrum of the heterogeneity function at any given spatial frequency (p, q) , i.e.

$$\hat{\Phi}_{sc}(p, q, z_d) = \int_{-\infty}^{\infty} dz' \hat{G}_0(p, q, z_d, z') \hat{T}(p, q, z') . \quad (23)$$

Without losing generality, we assume the optical heterogeneities are *below* the detection plane. This assumption enables us to remove the absolute value sign in the Weyl expansion in Eq. (19) since $z_d - z' > 0$. We also assume the heterogeneities are localized between the detection plane at $z = z_d$ and a plane at $z = z_0$. Thus we need consider only the interval between $(z=z_0, z=z_d)$ for the integral in Eq. (23). Dividing the turbid medium between the plane at $z = z_0$ and the detection plane into slices, we can rewrite Eq. (23) in the following form of discretized summation:

$$\begin{aligned} \hat{\Phi}_{sc}(p, q, z_d) &= \sum_{j=1}^N \Delta z \hat{T}(p, q, z_j) \hat{G}_0(p, q, z_d, z_j) \\ &= \sum_{j=1}^N \frac{i \Delta z}{2m} \hat{T}(p, q, z_j) e^{im(z_d-z_j)} , \end{aligned} \quad (24)$$

where in the second line we substitute the Green's function $\hat{G}_0(p, q, z_d, z_j)$ with its Weyl expansion (Eq. (19)); Δz is the discretized step size along the z-direction and N is the total

number of slices in the z -direction. Ideally the discretization step size Δz needs to be as small as possible. In practice we choose Δz to be a few random walk steps (i.e. $\sim \frac{1}{\mu'_{s0}}$).

Eq. (24) implies that at any given spatial frequency (p, q) , the heterogeneity functions at different depth z_j 's can be thought of as the “source terms” for the scattered wave. The plane waves arising from different slices propagate along the z direction to the detection plane. During the propagation these plane waves experience different amplitude attenuation and phase shifts which are given by $e^{im(z_d-z_j)}/m$, where $m = [k_0^2 - (2\pi)^2(p^2 + q^2)]^{1/2}$ is a complex number with $Im(m) > 0$; the scattered wave detected at the detection plane $z = z_d$ is thus a sum of plane waves originating from the heterogeneity functions at different depths. In Fig. 3 we illustrate this concept. In this figure we consider two non-zero heterogeneity functions $\tilde{T}_1(p, z_1)$ and $\tilde{T}_2(p, z_2)$ corresponding to plane waves along the x -direction in the x - z plane (i.e., $y = 0$) with a spatial frequency p at depth z_1 and z_2 . The perturbations from these two slices propagate to the detection plane with a phase shift and amplitude attenuation factor $e^{im(z_d-z_j)}/m$. At the detection plane the perturbations from these two slices add up to make a scattered wave $\tilde{\Phi}_{sc}(p, z_d)$ at the same spatial frequency p .

In K-space the propagation of the perturbation $\hat{T}(p, q, z_j)$ at different depths $z_d - z_j$ is weighted by the amplitude attenuation and phase shift given by the Weyl expansion of the Green's function $\hat{G}_0(p, q, z_d, z_j) = i e^{im(z_d-z_j)}/(2m)$. Recall $m = [k_0^2 - (2\pi)^2(p^2 + q^2)]^{1/2}$ with $Im(m) > 0$, therefore the amplitude and phase of the Weyl expansion $\hat{G}_0(p, q, z_d, z_j)$ depend on the spatial frequency (p, q) at a given depth $z_d - z_j$. The amplitude decays more quickly as the spatial frequencies (p, q) increase, and the Green's function effectively acts as a low pass filter in K-space.

For spatial frequencies (p, q) with the range of $(0, 1.6)$ cm $^{-1}$, we plot the amplitude and phase of the Weyl expansion ($\sim e^{im(z_d-z_j)}/m$) in Fig. 4 (a, b) assuming the depth is $z_d - z_j = 1$ cm. In calculating the incident diffuse wave wavenumber $k_0 = [(-v \mu_{a0} + i \omega)/D_0]^{1/2}$ we choose background optical properties $\mu_{a0} = 0.02$ cm $^{-1}$ and $\mu'_{s0} = 8.0$ cm $^{-1}$, and a 140 MHz modulation frequency. The resultant wavenumber is $|k_0| \sim 1.1$ cm $^{-1}$. We find that the amplitude attenuates by ~ 7 orders of magnitude when the spatial frequencies (p, q)

increase from $(0, 0)$ cm^{-1} to $(1.6, 1.6)$ cm^{-1} . In practice the maximum spatial frequency is determined by the Nyquist sampling frequency, i.e. $q_{max} = 1/2\Delta x \approx 0.833 \text{ cm}^{-1}$ for a scanning step size $\Delta x = 0.6 \text{ cm}$. In Fig. 4 (c, d), we also plot the amplitude attenuation and phase shift versus depth for given spatial frequencies, i.e. $(0.1, 0.1) \text{ cm}^{-1}$ and $(0.5, 0.5) \text{ cm}^{-1}$. The amplitude attenuates exponentially and the phase shift increases linearly as we consider the perturbation from deeper slices. Again as already shown in Fig. 4 (c), the amplitude attenuates much faster at spatial frequencies $(0.5, 0.5) \text{ cm}^{-1}$ than at $(0.1, 0.1) \text{ cm}^{-1}$. At any given depth $(z_d - z_j)$, those plane waves with sufficiently large spatial frequencies (p, q) have negligible contribution to the scattered wave, and therefore carry less information about the inhomogeneities.

B. 2-D Projection Imaging

2-D photographic images have been used by radiologists for many years. In order to acquire 2-D photographic-type *projection* images, we make a “thin” slice approximation by replacing z_j on the left hand side of Eq. (24) with the estimated slice position of the object. We then drop the sum over all *other* z_j ’s and obtain the following simple relation at any given spatial frequency (p, q) in K-space between the heterogeneity function at depth $z = z_{obj}$ and the measured scattered wave at the detection plane $z = z_d$:

$$\begin{aligned}\hat{T}(p, q, z_{obj}) &= \frac{\hat{\Phi}_{sc}(p, q, z_d)}{\Delta z \hat{G}_0(p, q, z_d, z_{obj})} \\ &= \frac{2m}{i\Delta z} \hat{\Phi}_{so}(p, q, z_d) e^{-im(z_d - z_{obj})}.\end{aligned}\quad (25)$$

This “thin” slice approximation may be adequate since we are often interested in early tumors whose size will be of the order of slice thickness of $\sim 0.5 \text{ cm}$, and thus can be considered thin. As we discussed at the end of Section V(A), plane waves in K-space with large spatial frequencies (p, q) are attenuated quickly as they propagate within the turbid media. The largest detectable spatial frequencies are determined by the sensitivity and signal-to-noise ratio of the detection system. For image reconstruction, we neglect the

high spatial frequency components (p, q) in the heterogeneity function $\tilde{T}(p, q, z_{obj})$ when $Im(m) > 3.5Im(k_0)$, by using an empirical “m-cut” filter in K-space [21].

When the heterogeneity function in K-space, $\tilde{T}(p, q, z_{obj})$, is determined by Eq. (25), we can then take the inverse 2-D Fourier transform of $\tilde{T}(p, q, z_{obj})$ to obtain the tumor function $T(x, y, z_{obj})$ in the real x-y space at the depth of the heterogeneity $z = z_{obj}$. We derive a 2-D photographic image of the optical properties using Eqs. (11) and (12); for example, $\delta\mu_a(x, y, z_{obj}) = T_{abs}(x, y, z_{obj})/(-\frac{v}{D_0} \Phi_0(x, y, z_{obj}))$ for absorbing objects, and $\delta\mu'_s(x, y, z_{obj}) = T_{sc}(x, y, z_{obj})/(\frac{3D_0 k_0^2}{v} \Phi_0(x, y, z_{obj}))$ for scattering objects. Note that for a purely absorbing or scattering object, either a frequency domain (modulation frequency $f \neq 0$) or a continuous-wave (CW, $f = 0$) DPDW can be employed to extract the absorption or scattering variation; but for objects having both absorption and scattering variations, a CW DPDW is not sufficient to separate the absorption and scattering. Details will be discussed in Section VI(A).

Consider next a case where the optical heterogeneities are located within a “thin” slice at $z = z_{obj}$ (see Fig. 5). If the slice thickness Δz is less than a few transport mean free path-lengths [$1/(\mu'_{s0} + \mu_{a0})$], the heterogeneity function within this thin slice is approximately uniform, therefore Eq. (25) provides a quite accurate relation between the heterogeneity function and the scattered wave in K-space, and optical properties of the heterogeneity can further be deduced quite accurately. For thicker objects (i.e. thickness > 4 mm), the average over the size of the object weighted by the sum of exponential amplitude and phase factors $e^{im(z_d - z_j)}/m$ provides only an approximate relation between the heterogeneity function and the scattered wave. However we find that the relative optical properties of multiple objects can still be reconstructed with an reasonable accuracy.

Obviously the image reconstruction involves only 2-D forward and inverse Fourier transforms, and no iterative schemes are needed; therefore this angular spectrum algorithm is very rapid.

C. *a priori* Depth Information and Perspectives of 3-D Imaging

From the derivation we notice that in principle, this K-space spectrum analysis algorithm should work well when the optical heterogeneities are confined within a thin slice. The reconstruction then provides a 2-D photographic projection image of the optical properties given *a priori* information about the depth of the heterogeneity. Since the heterogeneity function (therefore the optical properties of the heterogeneities) is related to the scattered wave via the Weyl expansion of the Green's function, and since the amplitude and phase of the Weyl expansion depend upon the depth $z_d - z_j$, an incorrect depth estimate produces incorrect values of the reconstructed optical properties. However, rough estimation of the depth information can be tolerated if it is desirable to reconstruct contrast images of multiple objects.

Eq. (25) reveals how the heterogeneity function and hence the reconstructed optical properties of the heterogeneities vary with the estimated depth. Choice of a too small depth underestimates the optical properties and a too large depth overestimates the optical properties. Fig. 6(a) shows the reconstructed absorption coefficient of a spherical object versus the estimated depth $z_d - z_{obj}$. In this case we have a spherical object of 0.5 cm radius 2 cm below the detection plane, i.e., $z_d - z_{obj} = 2$ cm. The true optical property variations of the spheres with respect to the background are $\delta\mu_a = 0.02 \text{ cm}^{-1}$ and $\delta\mu'_s = 0$. We find that the reconstructed absorption increases as the estimated object depth increases. In Fig. 6(b) we plot the ratio of the reconstructed absorption coefficients of two spherical absorbing objects ($\delta\mu_{a1}^{rec}/\delta\mu_{a2}^{rec}$) versus the estimated depth. One sphere of $\delta\mu_{a1} = 0.04 \text{ cm}^{-1}$ and $\delta\mu'_{s1} = 0 \text{ cm}^{-1}$ is at (2, 1, 3) cm and the other sphere of $\delta\mu_{a2} = 0.02 \text{ cm}^{-1}$ and $\delta\mu'_{s2} = 0 \text{ cm}^{-1}$ is at (1, -1, 3) cm. Two spheres have the same size (0.5 cm in radius) and they are chosen to be at the same depth, e.g. 2 cm below the detection plane. Therefore any depth estimate is either correct or incorrect for both objects at the same time, and we do not have to take into account the additional complexity shown in Fig. 6(a). We find that the ratio of the reconstructed absorption coefficients is not sensitive to the depth estimation,

and therefore the incorrect depth estimate for contrast image can be tolerated in this case.

The image quality is also affected by the choice of a *priori* depth. Recall the heterogeneity function and the scattered wave in K-space is coupled to each other via the Weyl expansion (see Eq. (25)). The factor $e^{-im(z_d - z_{obj})}/m$ increases exponentially with the $(z_d - z_{obj})$. The noise (numerical and experimental) can be amplified at greater depths ($|z_d - z_{obj}|$). A series of reconstructed images with different depths are shown in Fig. 7. In this example an absorbing spherical object is at (2, 1, 3) cm and the scattered wave is measured in the plane at $z=5$ cm over a 9×9 cm² square with steps of 0.6 cm. The images (b-f) are reconstructed with assumptions of the depth $(z_d - z_{obj})$ to be respectively 4, 3, 2, 1, 0 cm. We find that the image quality gets worse (e.g. noisier) at greater depths. The depth-dependent noise and the *monotonic* variation of the image sharpness make it difficult to estimate the true object depth from image sharpness. For a spatially extended object, however, a choice of a shallow depth is often sufficient to reconstruct fairly well the spatial margins of inhomogeneities.

In order to obtain better 3-D information with this diffraction tomography technique, one can use a secondary localization scheme to deduce the object depth. An example would be to scan the phased-array in two orthogonal planes [22,23]. Alternatively as shown in Fig. 8, if we take two planar measurements along two different directions of the same sample, the projection image 1 from the first measurement in one plane (plane 1) will provide the depth information for the projection image 2 from the second measurement in the other plane (plane 2).

D. Experimental Results

To demonstrate the experimental feasibility of this algorithm, we have performed amplitude and phase measurements in a parallel-plane geometry (Fig. 2). We used a rapid homodyne detection system based upon In-phase/Quadrature (IQ) demodulation techniques [24]. The block diagram of the experimental setup is shown in Fig. 9. Source light intensity is modulated at 100 MHz and the source power is about ~ 3 mW at 786 nm. The source light

is guided into a large fish tank of 50 Liters 0.75% Intralipid ($\mu_a=0.020 \text{ cm}^{-1}$, $\mu'_s=7.3 \text{ cm}^{-1}$) with a fiber bundle of 3 mm in diameter. The large volume of Intralipid enables the use of infinite medium boundary conditions. A detection fiber bundle also of 3 mm diameter, couples the detected diffusive wave to a fast avalanche photo-diode (APD).

The experimental geometry is shown in Fig. 2. The source position was fixed and taken to be the origin of our coordinate system. As shown in Fig. 2, we “made” the detection plane by scanning a single detection fiber over a square region from (-4.65, -4.65, 5.0) cm to (4.65, 4.65, 5.0) cm in a plane at $z_d=5.0$ cm in steps of size $\Delta x=\Delta y=0.3$ cm. The amplitude and phase of the DPDW was recorded at each position for a total of 1024 points. Each data point takes about half second. We directly measured the amplitude and phase in the *homogeneous* medium to obtain the incident wave $\Phi_0(\mathbf{r}_d)$.

In this experiment, a absorbing slice with dimensions $1.5 \times 1.5 \times 0.4 \text{ cm}^3$ was submerged in the turbid medium (0.75% Intralipid) at position (-1.6, -0.3, 3.0) cm. The slice was made of resin plus TiO_2 and absorbing dye. TiO_2 particles (from Sigma) cause the scattering and the absorbing dye (900NP from Zeneca) causes the absorption. The absorption coefficient of the slice was $\mu_{a,obj} \approx 0.20 \text{ cm}^{-1}$; its scattering coefficient was about the same as that of the background, i.e. $\sim 7.3 \text{ cm}^{-1}$. The scattered wave $\Phi_{sc}(\mathbf{r}_d)$ was obtained by subtracting the incident wave $\Phi_0(\mathbf{r}_d)$ from the measured (total) signal $\Phi(\mathbf{r}_d)$.

For image reconstruction, we first take the 2-D Fourier transform of the scattered wave $\Phi_{sc}(\mathbf{r}_d)$ measured at the detection plane $z = z_d$. Using Eq. (25) along with *a priori* information about the slice depth, we then obtain the heterogeneity function in K-space $\hat{T}(p, q, z_{obj})$ in the plane containing the slice at $z = z_{obj}$. During this step, an “m-cut” filter is used to neglect high spatial frequency components with $Im(m) > 3.5Im(k_0)$ in the heterogeneity function $\hat{T}(p, q, z_{obj})$. We then take 2-D inverse Fourier transform of $\hat{T}(p, q, z_{obj})$ with respect to spatial frequency (p, q) to obtain the heterogeneity function $T(x, y, z_{obj})$ in real space. Finally we divide the heterogeneity function $T(x, y, z_{obj})$ by the background field $\Phi_0(x, y, z_{obj})$ in the plane containing the slice at $z=z_{obj}$ to obtain a spatial map of the reconstructed

absorption variation, e.g., $\delta\mu_a(x, y, z_{obj}) = T_{abs}(x, y, z_{obj}) / (-\frac{v}{D_0} \Phi_0(x, y, z_{obj}))$. The homogeneous background field $\Phi_0(x, y, z_{obj})$ is calculated using the best estimated optical properties ($\mu_{a0}=0.017 \text{ cm}^{-1}$ and $\mu'_{s0}=7.21 \text{ cm}^{-1}$) by fitting the incident wave $\Phi_0(\mathbf{r}_d)$ measured in the detection plane $z=z_d$ to the exact solution of DPDW's (Eq. (16)). The reconstructed images of the slice are shown in Fig. 10. The reconstructed x-y position was about at (-1.80, -0.25) cm, close to the true x-y position at (-1.6, -0.3) cm. Inaccuracies in the position measurements might account for the discrepancy. The reconstructed absorption coefficient is well above the background noise level and close to the true value, e.g., $\delta\mu_{a,obj}^{rec} \approx 0.125 \text{ cm}^{-1}$. Errors in our estimate of the slice depth and background optical properties estimates are the main sources of inaccuracy in reconstructed absorption properties. The refractive index mismatch between the object (~ 1.46) and background medium (~ 1.33) also contributes to the inaccuracy in the reconstruction. The complete reconstruction based upon forward and inverse FFT calculations takes less than 0.2 second CPU time on Sun Sparc10 workstation.

The feasibility of this diffraction tomography algorithm for multiple slices and multiple spatially extended optical heterogeneities has also been experimentally verified [18]. We found that the optical properties of thin objects or the relative optical properties of spatially extended objects (contrast image) with *a priori* depth information can be reconstructed with a reasonable accuracy.

VI. TWO ISSUES RELATED TO ANGULAR SPECTRUM ALGORITHM

The angular spectrum algorithm provides an approximate relation between the heterogeneity function (or the heterogeneities) and the scattered wave within the framework of the first order Born approximation. In addition to this first order approximation, it also requires the information of the background optical properties. The resultant images are 2-D photographic-type images. In this section, we will consider the possibility of simultaneous reconstruction of the absorption and scattering coefficients, and we will explore methods to extract the background optical properties from a single measurement on a heterogeneous

sample.

A. Absorption and Scattering

So far we have assumed that we have either purely absorbing inhomogeneities or purely scattering inhomogeneities, but not a mixture. We introduce a dual modulation frequency approach as a means to reconstruct the absorption and scattering coefficients simultaneously.

When both absorption and scattering variations are present, the heterogeneity function is (see Eq. (11) and Eq. (12))

$$T(\mathbf{r}) = -\frac{v}{D_0} \Phi_0(\mathbf{r}) \delta\mu_a(\mathbf{r}) + \frac{3D_0 k_0^2}{v} \Phi_0(\mathbf{r}) \delta\mu'_s(\mathbf{r}) . \quad (26)$$

Within a “thin” slice approximation, the heterogeneity function $T(\mathbf{r})$ in the plane at $z = z_{obj}$ can be obtained using the angular spectrum algorithm. Dividing $T(\mathbf{r})$ by the incident wave $\Phi_0(\mathbf{r})$ in the plane at $z = z_{obj}$, we obtain the following quantity, denoted by $F(\omega)$, which is a function of $\delta\mu_a$, $\delta\mu'_s$, as well as the modulation frequency ω , i.e.

$$F(\omega) = \frac{T(\mathbf{r})}{\Phi_0(\mathbf{r})}|_{z_{obj}} = -3\mu'_{s0} \delta\mu_a(\mathbf{r}) + [-3\mu_{a0} + i\frac{3\omega}{v}] \delta\mu'_s(\mathbf{r}) . \quad (27)$$

Note that the scattering variation $\delta\mu'_s$ appears along with the modulation frequency, while $\delta\mu_a$ does not. Therefore, if we measure the scattered wave at two different modulation frequencies ω_1 and ω_2 , the difference between the two the reconstructed $F(\omega_1)$ and $F(\omega_2)$ will only be related to $\delta\mu'_s$:

$$F(\omega_2) - F(\omega_1) = i \frac{3(\omega_2 - \omega_1)}{v} \delta\mu'_s . \quad (28)$$

$\delta\mu'_s$ can be determined from Eq. (28). Then by substituting the resultant $\delta\mu'_s$ into Eq. (27), we can then determine the absorption variation $\delta\mu_a$.

To demonstrate the feasibility of this approach, we simultaneously reconstruct the absorption and scattering coefficients of a generic slice using simulated data. The simulation geometry is similar to the experimental geometry shown in Fig. 2. A $1 \times 1 \times 0.3 \text{ cm}^3$ slice of $\mu_a = 0.04 \text{ cm}^{-1}$ and $\mu'_s = 12.0 \text{ cm}^{-1}$ is placed at $(1, -1, 3) \text{ cm}$. The source is at $(0, 0, 0) \text{ cm}$

and the homogeneous background has optical properties of $\mu_{a0} = 0.02 \text{ cm}^{-1}$ and $\mu'_{s0} = 8.0 \text{ cm}^{-1}$. Note that the slice has both absorption and scattering variations with respect to the homogeneous background. The total and background diffuse photon density waves at $z_d = 5 \text{ cm}$ are calculated for $f = 70 \text{ MHz}$ and $f = 140 \text{ MHz}$ using the finite difference method. The reconstructed images are shown in Fig. 11 (b) and (c). The reconstructed absorption and scattering coefficients are $\delta\mu_a \approx 0.025 \text{ cm}^{-1}$ and $\delta\mu'_s \approx 3.32 \text{ cm}^{-1}$. We find that this approach provides simultaneous estimates of the absorption and scattering coefficients with a reasonable accuracy.

B. Extraction of Background Optical Properties

Image reconstruction requires knowledge of the optical properties of the homogeneous background medium. For example, the complex spatial frequency $m = [k_0^2 - (2\pi)^2(p^2 + q^2)]^{1/2}$ in Eq. (25) depends on the incident photon density wave number k_0 , and k_0 in turn depends upon the absorption and scattering coefficients of the background turbid medium (e.g., $k_0 = \|(-v\mu_{a0} + i\omega)/D_0\|^{1/2}$). Ideally we would like to determine the background optical properties from a single data set measured on a heterogeneous medium. One simple way to achieve this goal is to fit the heterogeneous data set with a homogeneous model to obtain bulk average values of the optical properties. We find that the results for this case are generally unsatisfactory. Fig. 12(b) shows the total photon density wave $\Phi(\mathbf{r})$ (the amplitude, for example) from the absorbing slice experiment where the detector was scanned along a line symmetrically with respect to the source. When fitting all the data points with a simple homogeneous model, we find that the resultant absorption and scattering coefficients are $\mu_{a0}^{fit} = 0.012 \text{ cm}^{-1}$ and $\mu'_{s0}^{fit} = 6.27 \text{ cm}^{-1}$, while the expected values for 0.75% Intralipid are $\mu_{a0} = 0.020 \text{ cm}^{-1}$ and $\mu'_{s0} = 7.30 \text{ cm}^{-1}$.

We can improve the results by considering the symmetry of our detection scheme. As we recall (see Fig. 2), our scanning geometry is mirror symmetric with respect to the source. In Fig. 12(a), we project the 3-D geometry into 2-D to re-emphasize this mirror symmetry. If the

medium is homogeneous, the data should be symmetric with respect to source; if the medium is heterogeneous, the left-right symmetry will be broken. This broken symmetry enables us to identify the data points which are mostly perturbed by the inhomogeneities. Since the phase of diffuse photon density waves is not as sensitive to the absorption variation as the amplitude, it is safe to use only the amplitudes of the photon density waves in identifying the most perturbed data points from the symmetry consideration. If the left-right difference in amplitude signals is greater than the system noise level, we call those data points the most perturbed data points (See Fig. 12(c)). We then exclude these perturbed data points, and fit the rest of data points (both amplitude and phase) to a homogeneous model (see Fig. 12(d)). We find that resultant optical properties are indeed improved, e.g., $\mu_{a0}^{fit} = 0.015 \text{ cm}^{-1}$ and $\mu_{s0}^{fit} = 7.23 \text{ cm}^{-1}$, where the inaccuracy decreases from $\sim 40\%$ to $\sim 25\%$ in μ_{a0} and from $\sim 18\%$ to $\sim 2\%$ in μ_{s0}^f .

VII. SLAB AND SEMI-INFINITE GEOMETRIES

Recall that the total photon density wave $\Phi(\mathbf{r})$ for a turbid medium with boundaries is given by Eq. (14), i.e.

$$\begin{aligned}\Phi(\mathbf{r}) = & \frac{v}{D_0} \int_V S(\mathbf{r}') G(\mathbf{r}, \mathbf{r}') d^3 r' + \int_V T(\mathbf{r}') G(\mathbf{r}, \mathbf{r}') d^3 r' \\ & + \int_S [G(\mathbf{r}, \mathbf{r}') \frac{\partial \Phi(\mathbf{r}')}{\partial n'} - \Phi(\mathbf{r}') \frac{\partial G(\mathbf{r}, \mathbf{r}')}{\partial n'}] dA' .\end{aligned}\quad (29)$$

On the surface of the turbid medium, the diffuse photon density wave satisfies the zero *partial current* boundary condition [25]:

$$\Phi(\mathbf{r}) + \frac{1+R_{eff}}{1-R_{eff}} \frac{2D_0}{v} \frac{\partial \Phi(\mathbf{r})}{\partial n'} = 0 \rightarrow \frac{\partial \Phi(\mathbf{r})}{\partial n'} = -\alpha \Phi(\mathbf{r}) , \quad (30)$$

for \mathbf{r} on the surface .

Here n' is the surface normal pointing outward from the scattering medium, $\alpha = \frac{1-R_{eff}}{1+R_{eff}} \frac{u}{2D_0}$ where R_{eff} is the effective reflection coefficient². Using this zero partial current boundary condition in Eq. (29), we obtain a general solution for the total diffuse photon density wave $\Phi(\mathbf{r})$ in a finite turbid medium:

$$\begin{aligned}\Phi(\mathbf{r}) &= \frac{v}{D_0} \int_V S(\mathbf{r}') G(\mathbf{r}, \mathbf{r}') d^3 r' + \int_V T(\mathbf{r}') G(\mathbf{r}, \mathbf{r}') d^3 r' \\ &\quad - \int_S \Phi(\mathbf{r}') [\alpha G(\mathbf{r}, \mathbf{r}') + \frac{\partial G(\mathbf{r}, \mathbf{r}')}{\partial n'}] dA'.\end{aligned}\quad (31)$$

How the scattered wave is related to the heterogeneity function in this case? As we discussed at the end of Section III, the surface term (the last term in the above equation) depends on the total photon density wave $\Phi(\mathbf{r})$, and therefore the surface term includes both an incident wave component and a scattered wave component. Analytic separation of the incident wave component from the scattered wave component in the surface term is generally not feasible though perturbative approaches may be used approximately.

The approach we take here is to find an appropriate Green's function so that the surface term is zero by requiring

$$\alpha G(\mathbf{r}, \mathbf{r}') + \frac{\partial G(\mathbf{r}, \mathbf{r}')}{\partial n'} = 0, \quad \mathbf{r} \text{ is on the surface.} \quad (32)$$

Note that this boundary condition, as we discussed in Section III, is naturally satisfied for an infinite turbid medium (no photons reach the infinity). By requiring the Green's function to satisfy Eq. (32), we then have the total photon density wave $\Phi(\mathbf{r})$:

$$\Phi(\mathbf{r}) = \frac{v}{D_0} \int_V S(\mathbf{r}') G(\mathbf{r}, \mathbf{r}') d^3 r' + \int_V T(\mathbf{r}') G(\mathbf{r}, \mathbf{r}') d^3 r', \quad (33)$$

from which we can obtain the scattered wave $\Phi_{sc}(\mathbf{r})$:

²The exact expression of R_{eff} was derived by Haskell, Tromberg and their coworkers [25]. An approximate expression offered by Ghoenluis and coworkers [26], is in agreement with the exact R_{eff} within 10%. The approximate expression is $R_{eff} = -1.440n^{-2} + 0.710n^{-1} + 0.668 + 0.0636n$ where the relative index of refraction $n = n_{in,turbid}/n_{out,air}$.

$$\Phi_{sc}(\mathbf{r}) = \Phi(\mathbf{r}) - \Phi_0(\mathbf{r}) = \int_V T(\mathbf{r}') G(\mathbf{r}, \mathbf{r}') d^3 n' . \quad (34)$$

Our task is to find the appropriate Green's function which satisfies Eq. (13) and the boundary condition given by Eq. (32), i.e.

$$(\nabla^2 + k_0^2)G(\mathbf{r}, \mathbf{r}') = -\delta(\mathbf{r}, \mathbf{r}') , \quad (35)$$

and

$$\alpha G(\mathbf{r}, \mathbf{r}') + \frac{\partial G(\mathbf{r}, \mathbf{r}')}{\partial n'} = 0 , \text{ for } \mathbf{r} \text{ on the boundaries.} \quad (36)$$

We expect the Green's function for a finite medium to include the Green's function in an infinite medium $G_0(\mathbf{r}, \mathbf{r}')$, and an additional term $G_h(\mathbf{r}, \mathbf{r}')$ which results from backreflections at the boundaries, i.e.

$$G(\mathbf{r}, \mathbf{r}') = G_0(\mathbf{r}, \mathbf{r}') + G_h(\mathbf{r}, \mathbf{r}') , \quad (37)$$

where $G_0(\mathbf{r}, \mathbf{r}') = \frac{\exp(ik_0|\mathbf{r}-\mathbf{r}'|)}{4\pi|\mathbf{r}-\mathbf{r}'|}$. $G_h(\mathbf{r}, \mathbf{r}')$ is required to satisfy the homogeneous Helmholtz equation:

$$(\nabla^2 + k_0^2)G_h(\mathbf{r}, \mathbf{r}') = 0 , \quad (38)$$

and the following boundary condition:

$$\alpha G_h(\mathbf{r}, \mathbf{r}') + \frac{\partial G_h(\mathbf{r}, \mathbf{r}')}{\partial n'} = -[\alpha G_0(\mathbf{r}, \mathbf{r}') + \frac{\partial G_0(\mathbf{r}, \mathbf{r}')}{\partial n'}] , \text{ for } \mathbf{r} \text{ on the boundaries.} \quad (39)$$

A. Slab Geometry

Boundaries of arbitrary shapes are in general difficult to incorporate into the solution of the photon diffusion equation (Eq. (14)). Here we consider a slab geometry shown in Fig. 13. Within the slab is the scattering medium and outside the slab is air. This slab geometry is to approximate the compressed breast configuration which is suitable for clinical breast lesion diagnosis.

Suppose the two surfaces of a slab turbid medium are at $z = z_0$ and $z = z_d$ as shown in Fig. 13. Again we use the angular spectrum representation of the Green's function $G_h(\mathbf{r}, \mathbf{r}')$, i.e.

$$G_h(\mathbf{r}, \mathbf{r}') = \iint dp dq \hat{G}_h(p, q, z, z') e^{-i2\pi [p(x-x')+q(y-y')]} , \quad (40)$$

Substituting this equation in Eq. (38), we find for any given spatial frequencies (p, q) , $\hat{G}_h(p, q, z, z')$ satisfies the following 1-dimensional homogeneous Helmholtz equation:

$$[\frac{\partial^2}{\partial^2 z} + m^2] \hat{G}_h(p, q, z, z') = 0 , \quad (41)$$

where $m = [k_0^2 - (2\pi)^2(p^2 + q^2)]^{1/2}$ and $Im(m) > 0$. The boundary conditions given by Eq. (39) for a slab geometry shown in Fig. 13 can be rewritten for the angular spectrum $\hat{G}_h(p, q, z, z')$ as

$$\alpha \hat{G}_h(p, q, z, z' = z_0) - \frac{\partial \hat{G}_h(p, q, z, z' = z_0)}{\partial z'} = -(\alpha + im) \hat{G}_0(p, q, z, z' = z_0) , \quad (42)$$

$$\alpha \hat{G}_h(p, q, z, z' = z_d) + \frac{\partial \hat{G}_h(p, q, z, z' = z_d)}{\partial z'} = -(\alpha + im) \hat{G}_0(p, q, z, z' = z_d) , \quad (43)$$

where $\hat{G}_0(p, q, z, z') = \frac{i}{2m} e^{im|z-z'|}$ is given by the Weyl expansion (see Eq. (19)).

The general solution of $\hat{G}_h(p, q, z, z')$ has the form of

$$\hat{G}_h(p, q, z, z') = A e^{imz'} + B e^{-imz'} . \quad (44)$$

The first term represents the wave which is reflected by the *lower* surface at $z = z_0$ and then propagates *forward* along $+z$ direction, i.e., the “transmission” component; the second term represents the wave which is reflected by the *upper* surface at $z = z_d$ and then propagates *backward* along $-z$ direction, i.e., the “reflection” component. Coefficients A and B can then be solved using the boundary conditions given by Eqs. (42) and (43). After some algebra, we find that

$$A = f_1 e^{imz} + f_2 e^{-imz} , \quad B = f_3 e^{imz} + f_4 e^{-imz} , \quad (45)$$

where f_1, f_2, f_3 and f_4 are given by

$$f_1 = \frac{f_0}{\beta} (\alpha^2 + m^2) e^{-im(z_d+z_0)}, \quad f_2 = -\frac{f_0}{\beta} (\alpha + im)^2 e^{im(z_d-z_0)}, \quad (46)$$

$$f_3 = -\frac{f_0}{\beta} (\alpha + im)^2 e^{im(z_d-z_0)}, \quad f_4 = \frac{f_0}{\beta} (\alpha^2 + m^2) e^{im(z_d+z_0)}, \quad (47)$$

with

$$f_0 = \frac{i}{2m}, \quad \beta = (\alpha + im)^2 e^{im(z_d-z_0)} - (\alpha - im)^2 e^{-im(z_d-z_0)}. \quad (48)$$

Finally for a slab geometry, the Fourier component of total Green's function $\hat{G}(p, q, z, z')$ in K-space is

$$\begin{aligned} \hat{G}(p, q, z, z') &= \hat{G}_0(p, q, z, z') + \hat{G}_h(p, q, z, z') = \\ f_0 e^{im|z-z'|} + f_1 e^{im(z+z')} + f_2 e^{-im(z-z')} + f_3 e^{im(z-z')} + f_4 e^{-im(z+z')} \end{aligned} \quad (49)$$

Using $\hat{G}(p, q, z, z')$, the relation between the scattered wave $\hat{\Phi}_{sc}(p, q, z_d)$ and the heterogeneity function $\hat{T}(p, q, z_{obj})$ for a slab geometry within "thin" slice approximation is

$$\hat{T}(p, q, z_{obj}) \approx \frac{\hat{\Phi}_{sc}(p, q, z_d)}{\Delta z \hat{G}(p, q, z_{obj})}. \quad (50)$$

The 2-D inverse Fourier transform of $\hat{T}(p, q, z_{obj})$ gives the heterogeneity function $T(x, y, z_{obj})$ in real x-y space. The optical properties of the inhomogeneities can then be obtained, e.g., for absorbing objects, we have $\delta\mu_a(x, y, z_{obj}) = T_{abs}(x, y, z_{obj}) / (-\frac{v}{D_0} \Phi_0^{slab}(x, y, z_{obj}))$; and for scattering objects, we have $\delta\mu'_s(x, y, z_{obj}) = T_{sc}(x, y, z_{obj}) / (\frac{3D_0 k_0^2}{v} \Phi_0^{slab}(x, y, z_{obj}))$.

Using the appropriate Green's function (Eq. (49)) for a slab geometry, we reconstructed a 2-D optical image of a slice embedded in a slab turbid medium. The slab geometry is shown in Fig. 13 where the two surfaces are at planes $z = 0$ and $z = 5$ cm, respectively. The source is at the origin. A 1.0×1.0 cm² slice of 0.3 cm thick is at (1,-1,3) cm (see Fig. 14 (a)) and the detection plane is at the top surface of the slab ($z = 5$ cm). The slice has a higher absorption coefficient than the background medium but shares the same scattering coefficient with the background, e.g., $\mu_{a,obj} = 0.04$ cm⁻¹ and $\mu'_{s,obj} = 8.0$ cm⁻¹ for the slice and $\mu_{a,0} = 0.02$ cm⁻¹ and $\mu'_{s,0} = 8.0$ cm⁻¹ for the background. The total and background diffuse photon density waves at the top surface $z=5$ cm are calculated using the finite difference method.

The reconstructed absorption image using the appropriate Green's function (Eq. (49)) for the slab geometry is shown in Fig. 14 (b), and the reconstructed absorption is $\delta\mu_{a,slab}^{rec} \approx 0.0240 \text{ cm}^{-1}$, which is close to the expected value $\delta\mu_a^{th} = 0.0200 \text{ cm}^{-1}$. For comparison, we also reconstructed the image of the slice using the *wrong* Green's function, i.e. the Green's $G_0(\mathbf{r}, \mathbf{r}')$ which is only correct for the infinite medium (Eq. (19)). The resultant absorption image is shown in Fig. 14 (c). We found that the position of the slice can be well reconstructed by using different Green's functions. However the image shown in Fig. 14 (c), which is reconstructed by using the *wrong* infinite Green's function, has more artifacts than that shown in Fig. 14 (b), which is reconstructed by using the *right* slab Green's function. Notice that the Green's function for a slab geometry $|\hat{G}(p, q, z, z')|$ is smaller than the Green's function for an infinite geometry $|\hat{G}_0(p, q, z, z')|$ simply because we lose photons through the finite boundaries. When we use the Green's function of an infinite medium to reconstruct the image for a slab geometry, the overestimate of the Green's function is responsible for the nosier image structures (artifacts) in Fig. 14(c). The overestimated infinite Green's function also results in smaller reconstructed optical properties, e.g., the reconstructed value by using the *wrong* infinite Green's function, $\delta\mu_{a,wrong}^{rec} = 0.0056 \text{ cm}^{-1}$, is about 4 times as small as the value $\delta\mu_{a,slab}^{rec} = 0.0240 \text{ cm}^{-1}$ reconstructed by using the appropriate slab Green's function. We see that the appropriate Green's function for a slab geometry (Eq. (49)) produces cleaner images and more accurate optical properties than the Green's function which is only suitable for an infinite medium (Eq. (19)).

B. Semi-infinite Geometry

As an extension of the above derivation, we can easily obtain the Fourier component of the total Green's function $\hat{G}^{semi}(p, q, z, z')$ for a *semi-infinite* turbid medium. Alternatively we can start with the Green's function for a slab geometry (Eq. (49)), then move the lower boundary of the slab in Fig. 13 to the negative infinity, i.e. $z_0 \rightarrow -\infty$. Note that $Im(m) > 0$ and therefore all terms in Eq. (49) with e^{-imz_0} vanish when $z_0 \rightarrow -\infty$. The

Fourier component of the total Green's function $\hat{G}^{semi}(p, q, z, z')$ for a *semi-infinite* medium at any spatial frequencies (p, q) in K-space is thus

$$\hat{G}^{semi}(p, q, z, z') = f_0 e^{im|z-z'|} + f_1^{semi} e^{-im(z+z')} . \quad (51)$$

Here the coefficients f_0 and f_1^{semi} are given by

$$f_0 = \frac{i}{2m}, \quad f_1^{semi} = -f_0 \frac{\alpha + im}{\alpha - im} e^{2imz_d} . \quad (52)$$

The first term on the right hand side of Eq. (51) represents the Green's function in an infinite medium, and the second term represents the wave which is reflected by the boundary at $z = z_d$ and propagates backward along the negative z -direction. For arbitrary boundaries the solution of the Green's function are in general difficult to obtain.

C. Re-emission Geometry

In the previous discussions the source and the detector were assumed to be on the opposite sides of the inhomogeneity. This configuration is called transmission (see Fig. 15 (a)). It is suitable for two-plate soft compression geometry in breast cancer studies, with the source placed on one plate and the detector scanned over the other plate. Interestingly the derivation is not limited to this transmission configuration. Recall that dependence of the angular spectrum algorithm on the source position is implied in the heterogeneity function (see Eqs. (11) and (12)). The relation between the heterogeneity function and the scattered wave measured at the detection plane (see Eq. (25)) does not explicitly depend on the source position. The light source and the detector can be placed on the same side or on the opposite sides of the object without affecting the conclusion of the above derivation. Hence, we can apply the algorithm equally well to another geometry - the re-emission geometry (see Fig. 15 (b)) [27,28]. In the re-emission configuration, the detector scans in the plane which contains the source. This could be necessary, for example, in brain function studies. The re-emission geometry could also be useful for studies of large dense breast tissues in which fewer photons pass through the tissue.

In the transmission geometry, we measure the scattered wave propagating *forward* away from the source; in the re-emission geometry, we measure the scattered wave propagating *backward* towards the source. For a re-emission geometry and within a thin slice approximation, the relation of the heterogeneity function $\hat{T}(p, q, z_{obj})$ in K-space with the measured scattered wave in the plane $z = z_d$ is given by the same equation as for the transmission geometry (Eq. (25)). Here we rewrite the relation for the re-emission geometry:

$$\hat{T}(p, q, z_{obj}) = \frac{\hat{\Phi}_{sc}(p, q, z_d)}{\Delta z \hat{G}(p, q, z_d, z_{obj})}, \quad (53)$$

where an appropriate Green's function for an infinite medium (Eq. (19)) or a slab medium (Eq. (49)) has been assumed.

Simulations have shown the applicability of the algorithm to the re-emission geometry. Consider an absorbing spherical inhomogeneity of 0.5 cm radius at (2, 1, 2) cm embedded in an otherwise homogeneous slab turbid medium (see Fig. 15 (c)). The two surfaces of the slab are at $z_0 = 0$ cm and $z_d = 4.0$ cm, respectively. The absorption and scattering coefficients of the sphere are $\mu_a = 0.04 \text{ cm}^{-1}$ and $\mu'_s = 8.0 \text{ cm}^{-1}$ while the background optical properties are $\mu_{a0} = 0.02 \text{ cm}^{-1}$ and $\mu'_{s0} = 8.0 \text{ cm}^{-1}$. For the re-emission configuration, both the source and detector are placed on the top surface of the slab, i.e. in a plane at $z_d = 4$ cm. The scattered wave is calculated over a $9 \times 9 \text{ cm}^2$ region with x-y steps of 0.6 cm. The source is placed at the center of the square scanning region in the detection plane, i.e. at (0, 0, 4) cm. The reconstructed image for the re-emission geometry is shown in Fig. 15 (d). For comparison we also reconstruct the image of the same object for the transmission geometry. In this case the source is at the origin (0, 0, 0) cm, on the lower surface of the slab, with all other configurations kept the same as in the re-emission geometry. The image is shown in Fig. 15 (e). We see that the image quality in these two configurations is about the same. The ratio of the reconstructed absorption coefficient for the re-emission geometry to that for the transmission geometry is $\delta\mu_{a,re-em}^{rec}/\delta\mu_{a,trans}^{rec} \sim 1.1$. The finite object size (as opposed to a “thin” slice) might contribute to the small difference in the reconstructed absorption.

VIII. SUMMARY

We have presented a full exposition of our recent work that employs the angular spectrum algorithm for optical diffraction tomography with diffuse photon density waves. The image reconstruction becomes practically easy for thin heterogeneities wherein the heterogeneity function of interest is proportional to the scattered wave measured at the detection plane, i.e. $\tilde{T}(p, q, z_{obj}) \propto \Phi_{sc}(p, q, z_d)$. We have shown that although this relation is accurate only for thin inhomogeneities, it provides an approximate short cut for fast, 2-D projection imaging of spatially extended objects. The reconstruction is very rapid, requiring only a forward and inverse Fourier transform, e.g., it takes less than 0.2 second on a Sparc10 workstation to reconstruct an image of ~ 1000 pixels. For spatially extended objects, although the reconstructed optical properties are not accurate, the ratio of the reconstructed optical properties of multiple objects are close to the true ratio. In this sense we say that *contrast* image can still be obtained by using this algorithm. The feasibility for using this algorithm for image reconstruction of absorbing and scattering inhomogeneities has been experimentally demonstrated [18].

We have extended the theory to other geometries including the slab and the semi-infinite geometry for both transmission and re-emission configuration. The theory was confirmed in simulation experiments.

APPENDIX A: CONVENTIONS USED IN THIS PAPER REGARDING FOURIER TRANSFORM

The conventions regarding the forward and inverse Fourier transforms are as follows.

Consider a function $f(x)$ in 1-dimension:

Forward Fourier transform:

$$F(p) = \int f(x) e^{i2\pi xp} dx ; \quad (\text{A1})$$

Inverse Fourier transform:

$$f(x) = \int F(q) e^{-i2\pi xp} dp ; \quad (\text{A2})$$

and the δ -function is therefore given by

$$\delta(p) = \int e^{i2\pi xp} dx , \quad \delta(x) = \int e^{-i2\pi px} dp . \quad (\text{A3})$$

Using these conventions, we eliminate the 2π factor outside the integral of forward and inverse Fourier transforms.

APPENDIX B: THE WEYL EXPANSION OF GREEN'S FUNCTION

Consider an infinite turbid medium. μ_{a0} and μ'_{s0} are respectively the absorption and scattering coefficients. The Green's function $G_0(\mathbf{r}, \mathbf{r}')$ satisfies the following equation:

$$(\nabla^2 + k_0^2) G_0(\mathbf{r}, \mathbf{r}') = -\delta(\mathbf{r}, \mathbf{r}') , \quad (\text{B1})$$

where $k_0 = [(-v\mu_{a0} + i\omega)/D_0]^{1/2}$ with $\text{Im}(k_0) > 0$; $D_0 = v/(3\mu'_{s0})$ is the photon diffusion coefficient. The solution of the Green's function is [19]

$$G_0(\mathbf{r}, \mathbf{r}') = \frac{e^{ik_0|\mathbf{r}-\mathbf{r}'|}}{4\pi|\mathbf{r}-\mathbf{r}'|} . \quad (\text{B2})$$

The Green's function is related to its Fourier transform by

$$G_0(\mathbf{r}) = \iiint \tilde{G}_0(p, q, n) e^{-i2\pi(px+qy+nz)} dp dq dn , \quad (\text{B3})$$

where we assume $\mathbf{r}^t = 0$ without losing generality and (p, q, n) are the spatial frequencies. Plugging Eq. (B3) into Eq. (B2) and using the integral expression for the δ -function (Eq. (A3)), we have

$$\begin{aligned} & \iiint \hat{G}_0(p, q, n) [k_0^2 - (2\pi)^2(p^2 + q^2 + n^2)] e^{-i2\pi(px+qy+nz)} dp dq dn \\ &= - \iiint e^{-i2\pi(px+qy+nz)} dp dq dn . \end{aligned} \quad (\text{B4})$$

Without a rigorous proof, we can obtain the Fourier transform of the Green's function just by looking at both sides of the above equation, i.e.

$$\hat{G}_0(p, q, n) = \frac{1}{(2\pi)^2(p^2 + q^2 + n^2) - k_0^2} = \frac{1}{(2\pi)^2n^2 - m^2} , \quad (\text{B5})$$

where $m = [k_0^2 - (2\pi)^2(p^2 + q^2)]^{1/2}$ and $Im(m) > 0$. Eq. (B3) can then be written as

$$G_0(\mathbf{r}) = \iint dp dq e^{-i2\pi(px+qy)} \int \frac{e^{-i2\pi nz}}{(2\pi)^2n^2 - m^2} dn , \quad (\text{B6})$$

The integral over spatial frequency n can first be done by “pole” structure analysis. There are two poles in the integral over n as shown in Fig. 16. For $z > 0$, we require $Im(n) < 0$ to ensure the convergence of the integral over n . Therefore we choose the pole in the lower half space (Fig. 16(a)), e.g., $n = -m/2\pi$ (recall $Im(m) > 0$ which gives $Im(n) < 0$). Note that the integral is along the clockwise direction which gives us an extra minus sign. The resultant integral is

$$\int \frac{e^{-i2\pi nz}}{(2\pi)^2(n + \frac{m}{2\pi})(n - \frac{m}{2\pi})} dn = -2\pi i \frac{e^{-i2\pi nz}}{(2\pi)^2(n - \frac{m}{2\pi})} \stackrel{n=-m/2\pi}{=} \frac{i}{2m} e^{imz} . \quad (\text{B7})$$

Similarly, for $z < 0$ we require $Im(n) > 0$. Therefore we choose the pole is in the upper half space (Fig. 16(b)), e.g., $n = m/2\pi$. The integral is along the counter-clockwise direction so there is no extra minus sign in this case. The resultant integral is thus

$$\int \frac{e^{-i2\pi nz}}{(2\pi)^2(n + \frac{m}{2\pi})(n - \frac{m}{2\pi})} dn = 2\pi i \frac{e^{-i2\pi nz}}{(2\pi)^2(n + \frac{m}{2\pi})} \stackrel{n=m/2\pi}{=} \frac{i}{2m} e^{-imz} . \quad (\text{B8})$$

Combining Eqs. (B7) and (B8), we have the general expression for the integral over n :

$$\int \frac{e^{-i2\pi nz}}{(2\pi)^2n^2 - m^2} dn = \frac{i}{2m} e^{im|z|} . \quad (\text{B9})$$

Substituting this equation into Eq. (B6), we then end up with the Weyl expansion of the Green's function:

$$G_0(\mathbf{r}) = \iint dp dq e^{-i2\pi(px+qy)} \frac{i}{2m} e^{im|z|}, \quad (\text{B10})$$

where $m = [k_0^2 - (2\pi)^2(p^2 + q^2)]^{1/2}$ and $\text{Im}(m) > 0$.

The Weyl expansion represents the superposition of elementary harmonic waves in the x - and y -directions ($e^{-i2\pi(px+qy)}$); the harmonic waves exponentially attenuate in the z -direction away from the plane $z = 0$ which contains the source. The harmonic waves and the attenuation factor $\frac{i e^{im|z|}}{2m}$ are so combined that the double integral in Eq. (B10) over all the spatial frequencies (p, q) yields the elementary damped spherical wave on the left-hand side of Eq. (B10), i.e., $G_0(\mathbf{r}) = e^{ik_0 r}/(4\pi r)$.

REFERENCES

- [1] M. Cutler, "Transillumination as an aid in the diagnosis of breast lesions," *Surg. Gynecol. Obstet.* **48**, 721–730 (1929).
- [2] A. Yodh and B. Chance, "Spectroscopy and imaging with diffusing light," *Physics Today*, **48**, 34–40 (March 1995).
- [3] C. O. Johnson, "Optical Diffusion in blood," *IEEE Trans. BME* **17**, 129–133 (1970).
- [4] A. Ishimaru, in *Wave Propagation and Scattering in Random Media* (Academic Press, New York, 1978).
- [5] M. S. Patterson, B. Chance, and B. C. Wilson, "Time Resolved Reflectance and Transmittance for the Non-Invasive Measurement of Tissue Optical Properties," *Appl. Opt.* **28**, 2331–2336 (1989).
- [6] B. Barbieri, F. D. Piccoli, M. van de Ven, and E. Gratton, "What determines the uncertainty of phase and modulation measurements in frequency domain fluorometry?," *SPFE Time resolved laser spectroscopy in biochemistry II* **1204**, 158–170 (1990).
- [7] J. B. Fishkin and E. Gratton, "Propagation of Photon Density Waves in Strongly Scattering Media containing an Absorbing "Semi-infinite" Plane Bounded by a Straight edge," *J. Opt. Soc. of America A* **10**, 127–140 (Jan 1993).
- [8] J. B. Fishkin, O. Coquoz, E. R. Anderson, M. Brenner, and B. J. Tromberg, "Frequency-domain photon migration measurements of normal and malignant tissue optical properties in a human subject," *Appl. Opt.* **36**, 10–20 (1997).
- [9] in *Advances in Optical Imaging and Photon Migration, on Trends in Optics and Photonics Vol. XXI*, J. G. Fujimoto and M. S. Patterson, Eds, Orlando,FL (1998).
- [10] M. A. OLeary, D. A. Boas, B. Chance, and A. G. Yodh, "Experimental images of heterogeneous turbid media by frequency-domain diffusing-photon tomography," *Opt.*

Lett. **20**, 426–428 (1995).

- [11] S. R. Arridge, M. Schweiger, M. Hiraoka, and D. T. Delpy, “Performance of an iterative reconstruction algorithm for near infrared absorption and scattering imaging,” SPIE Proc. **1888**, 360–371 (1993).
- [12] B. W. Pogue, M. S. Patterson, H. Jiang, and K. D. Paulsen, “Initial assessment of a simple system for frequency domain diffuse optical tomography,” Phys. Med. Biol. **40**, 1709–1729 (1995).
- [13] H. Jiang, K. D. Paulsen, U. L. Osterberg, B. W. Pogue, and M. S. Patterson, “Simultaneous reconstruction of optical absorption and scattering maps in turbid media from near-infrared frequency-domain data,” Opt. Lett. **20**, 2128–2130 (1995).
- [14] J. H. Chang, H. L. Graber, and R. L. Barbour, “Imaging of fluorescence in highly scattering media,” IEEE Trans. Biomed. Eng. **44**, 810–822 (1997).
- [15] C. P. Gonatas, M. Ishii, J. S. Leigh, and J. C. Schotland, “Optical diffusion imaging using a direct inversion method,” Phys. Rev. E. **52**, 4361–4365 (1995).
- [16] E. Wolf, “Three dimensional structure determination of semi-transparent objects from holographic data,” Opt. Commun. **1**, 153–156 (1969).
- [17] D. N. Pattanayak, “Resolution of optical images formed by diffusion waves in highly scattering media,” GE Tech. Info. Series **91CRD241**, – (1991).
- [18] X. D. Li, T. Durduran, A. G. Yodh, B. Chance, and D. N. Pattanayak, “Diffraction tomography for biomedical imaging with diffuse photon density waves,” Opt. Lett. **22**, 573–575 (1997); X. D. Li, T. Durduran, A. G. Yodh, B. Chance, and D. N. Pattanayak, “Diffraction tomography for biomedical imaging with diffuse photon density waves—Errata,” Opt. Lett. **22**, 1198–1198 (1997).
- [19] J. D. Jackson, in *Classical Electrodynamics* (Wiley and Sons Inc., New York, 1975).

[20] A. J. Banos, in *Dipole Radiation in the Presence of a Conducting Half-Space* (Pergamon Press, New York, 1966).

[21] T. Durduran, J. P. Culver, M. J. Holboke, X. D. Li, L. Zubkov, and B. Chance, "Algorithms for 3d localization and imaging using near-field diffraction tomography with diffuse light," *Opt. Express.* **4**, 247–262 (1999).

[22] B. Chance, K. Kang, L. He, J. Weng, and E. Sevick, "Highly Sensitive Object Location in Tissue models with Linear in-phase and anti-phase multi-element optical arrays in one and two dimensions," *Proc. Natl. Acad. Sci. USA* **90**, 3423–3427 (April 1993).

[23] B. Chance, K. A. Kang, L. B. He, H. L. Liu, and S. M. Zhou, "Precision localization of hidden absorbers in body tissues with phased-array optical systems," *Rev. Sci. Instr.* **67**, 4324–4332 (1996).

[24] Y. S. Yang, H. L. Liu, X. D. Li, and B. Chance, "Low-cost frequency-domain photon migration instrument for tissue spectroscopy-oximetry and imaging," *Opt. Eng.* **36**, 1562–1569 (1997).

[25] R. C. Haskell, L. O. Svaasand, T. Tsay, T. Feng, M. S. McAdams, and B. J. Tromberg, "Boundary Conditions for the Diffusion Equation in Radiative Transfer," *J. Opt. Soc. Am. A* **11**, 2727–2741 (1994).

[26] R. A. J. Groenbuis, H. A. Ferwerda, and J. J. T. Bosch, "Scattering and absorption of turbid materials determined from reflection measurements 1:Theory," *Appl. Opt.* **22**, 2456–2462 (1983).

[27] X. D. Li, in *PhD Thesis* (Department of Physics and Astronomy, University of Pennsylvania, May 1998).

[28] X. Chieng and D. Boas, "Diffuse optical reflection tomography using continuous wave illumination," *Opt. Express* **3**, 118–123 (1998).

FIGURES

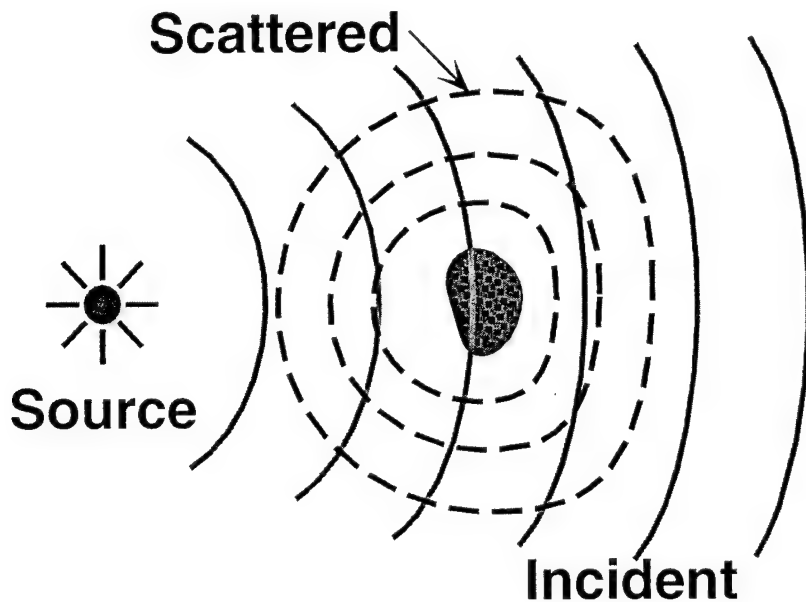


FIG. 1. In the presence of optical inhomogeneities, the spherical wave front of the incident wave is distorted. The total photon density wave is the sum of the incident wave and the scattered wave.

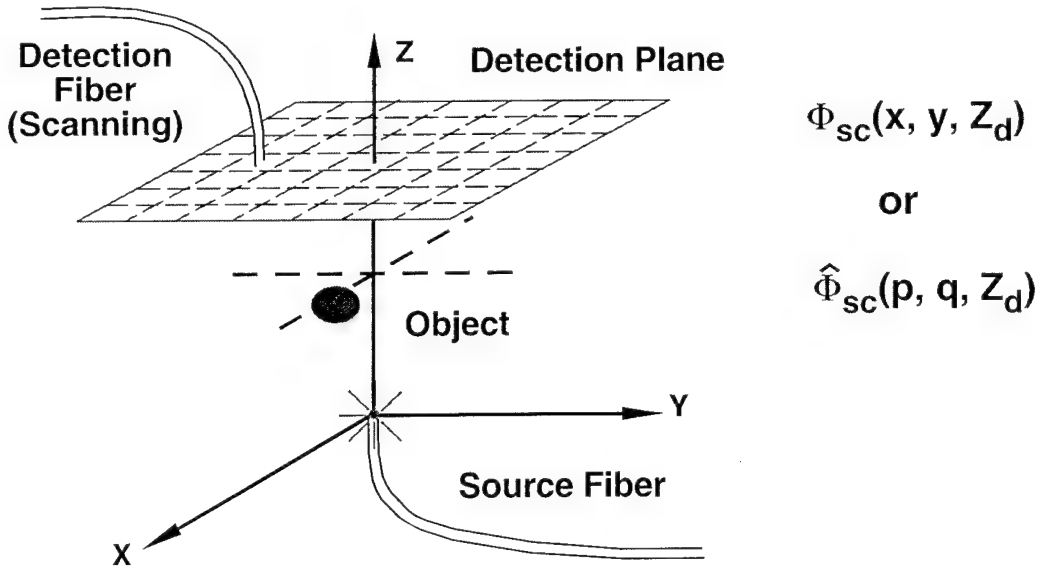


FIG. 2. Illustration of 2-D geometry which we consider for the image reconstruction algorithm based upon K-space spectrum analysis. The scattered wave $\Phi_{sc}(x, y, z_d)$ (or its spatial Fourier component $\hat{\Phi}_{sc}(p, q, z_d)$) is determined at the detection plane $z = z_d$ by scanning the detector over a square region. Without losing generality we assume the optical heterogeneities are located below the detection plane at $z = z_d$. A point source can be placed anywhere in the turbid medium. In practice the point source and the detection plane are either on the opposite side of the heterogeneities (transmission) or both on the same side of the heterogeneities (re-emission). In this figure the point source happens to be placed at the origin of our coordinate system for demonstration of a transmission measurement geometry.

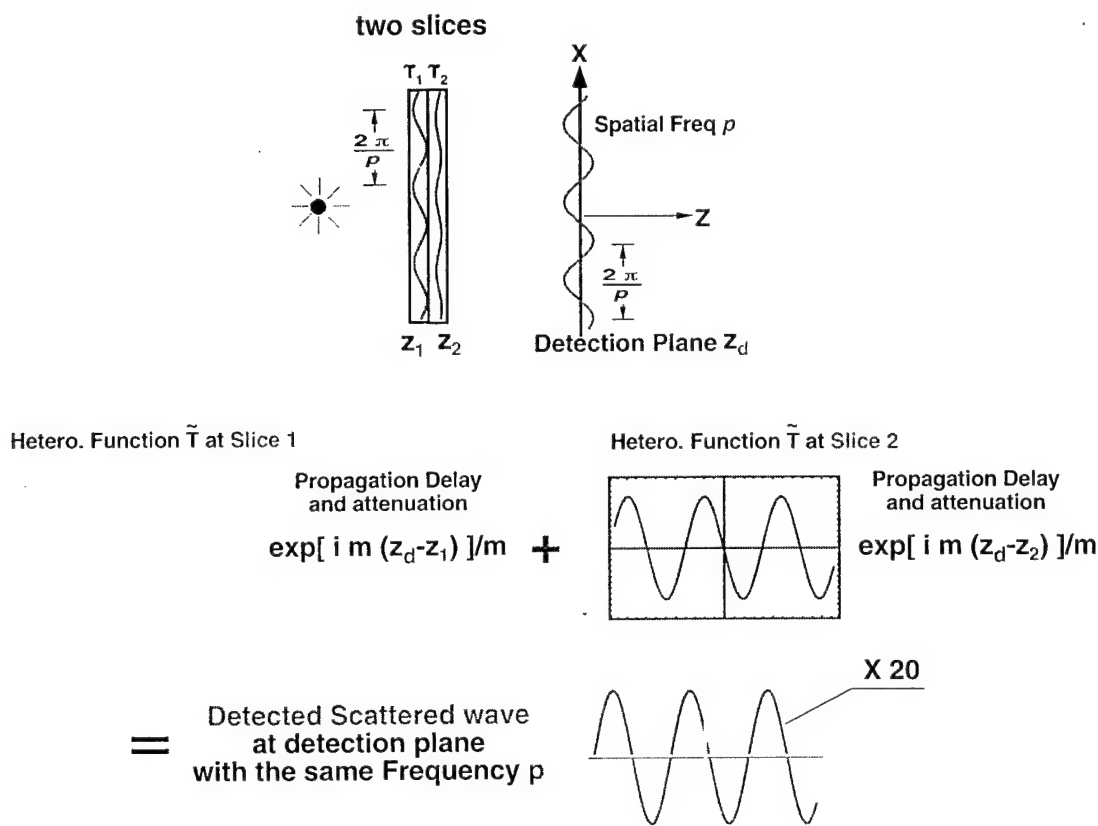


FIG. 3. The heterogeneity functions \hat{T}_1 and \hat{T}_2 with spatial frequency p from two slices propagate to the detection plane at $z = z_d$ where they add up to make the scattered wave $\hat{\Phi}_{sc}$ in K-space at the same spatial frequency p .

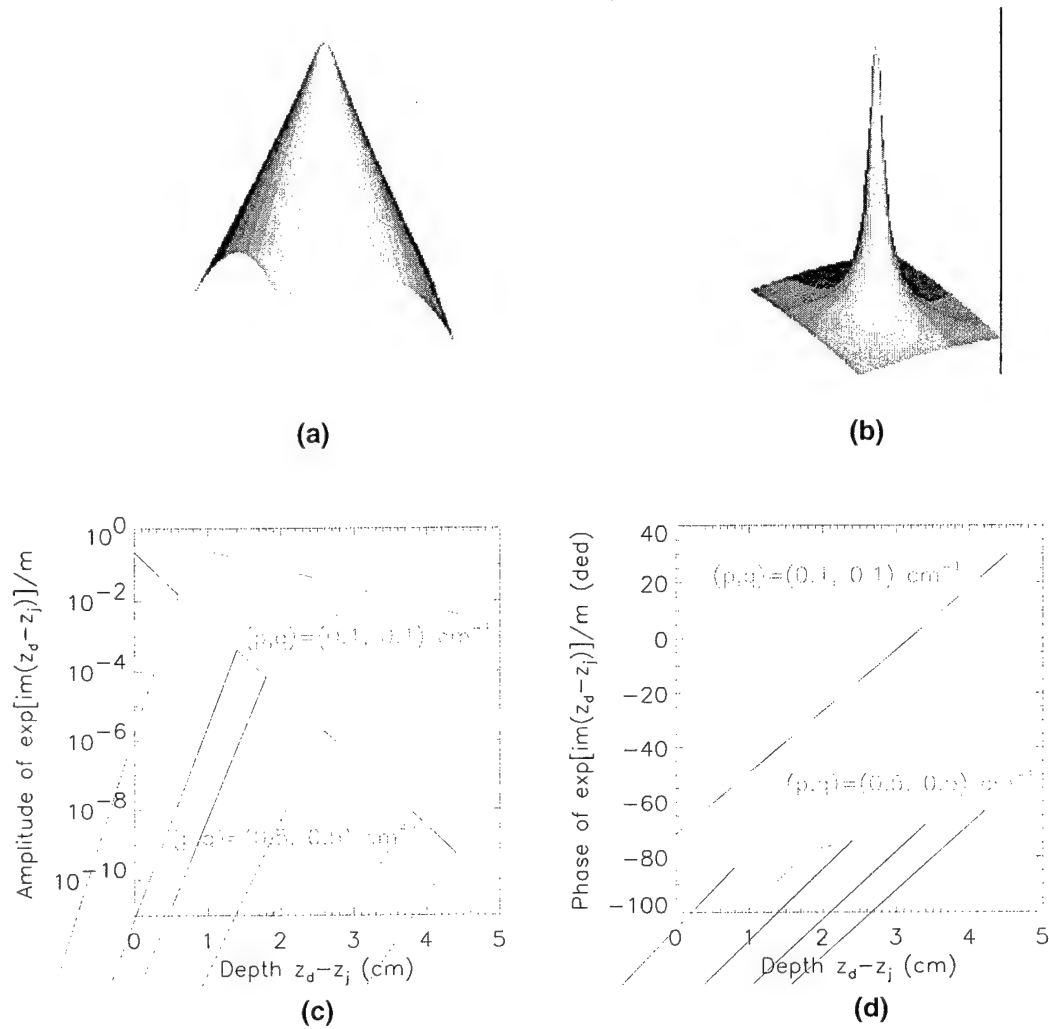


FIG. 4. (a) and (b) respectively show the amplitude attenuation and phase shift associated with the Weyl expansion in Kl-space versus spatial frequencies (p, q) . Note in (a) the z-axis is the log of the amplitude of $e^{im(z_d - z_j)}/m$; in (b) the z-axis is the phase of $e^{im(z_d - z_j)}/m$ in degrees. (c) and (d) show the amplitude attenuation and phase shift versus the depth $z_d - z_j$ for given spatial frequencies $(0.1, 0.1) \text{ cm}^{-1}$ (solid lines) and $(0.5, 0.5) \text{ cm}^{-1}$ (dashed lines).

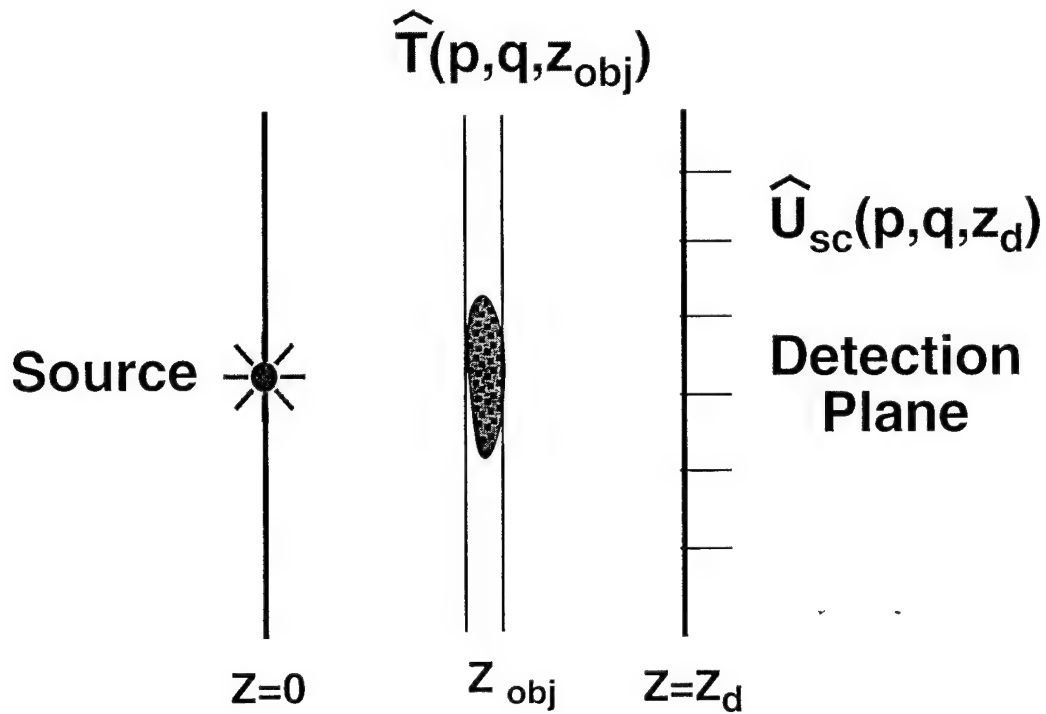


FIG. 5. The heterogeneities are considered to be thin which locate within a thin slice at $z = z_{\text{obj}}$ in parallel to the detection plane. The heterogeneity function within this thin slice is approximately uniform and the heterogeneity function is zero elsewhere.

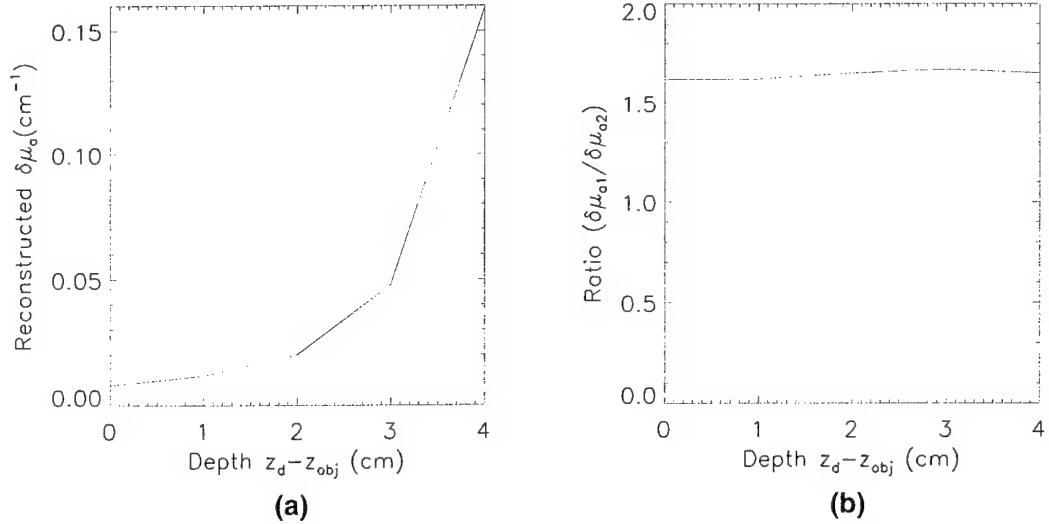


FIG. 6. (a) shows the reconstructed absorption coefficient versus the depth estimation. The data points in (a) are normalized by the absorption reconstructed at the depth where the object is, e.g. $z_d - z_{obj} = 2$ cm. (b) shows the ratio of reconstructed absorption of two spherical objects versus the depth estimation. Although the ratio is only approximately reconstructed (e.g., the true ratio is 2), the ratio is relatively insensitive to the depth estimate.

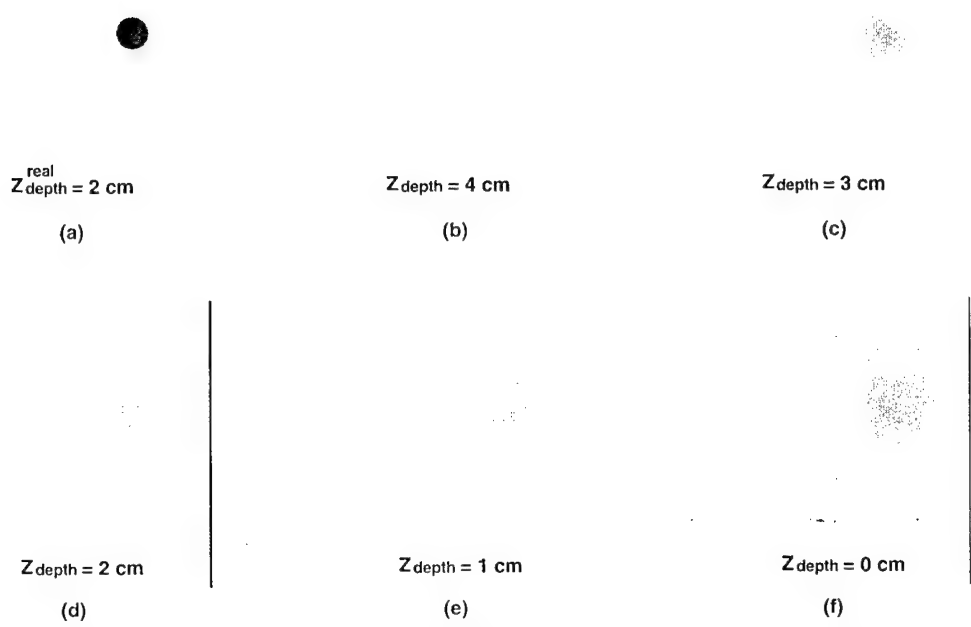


FIG. 7. Illustration of the dependence of reconstructed images on the estimated depth. The detection plane is at $z=5$ cm and an absorbing object shown in (a) is at $(2, 1, 3)$ cm which is 2 cm below the detection plane. (b-f) are the images reconstructed with an estimated depth respectively at 4 cm, 3 cm, 2 cm, 1 cm and 0 cm.

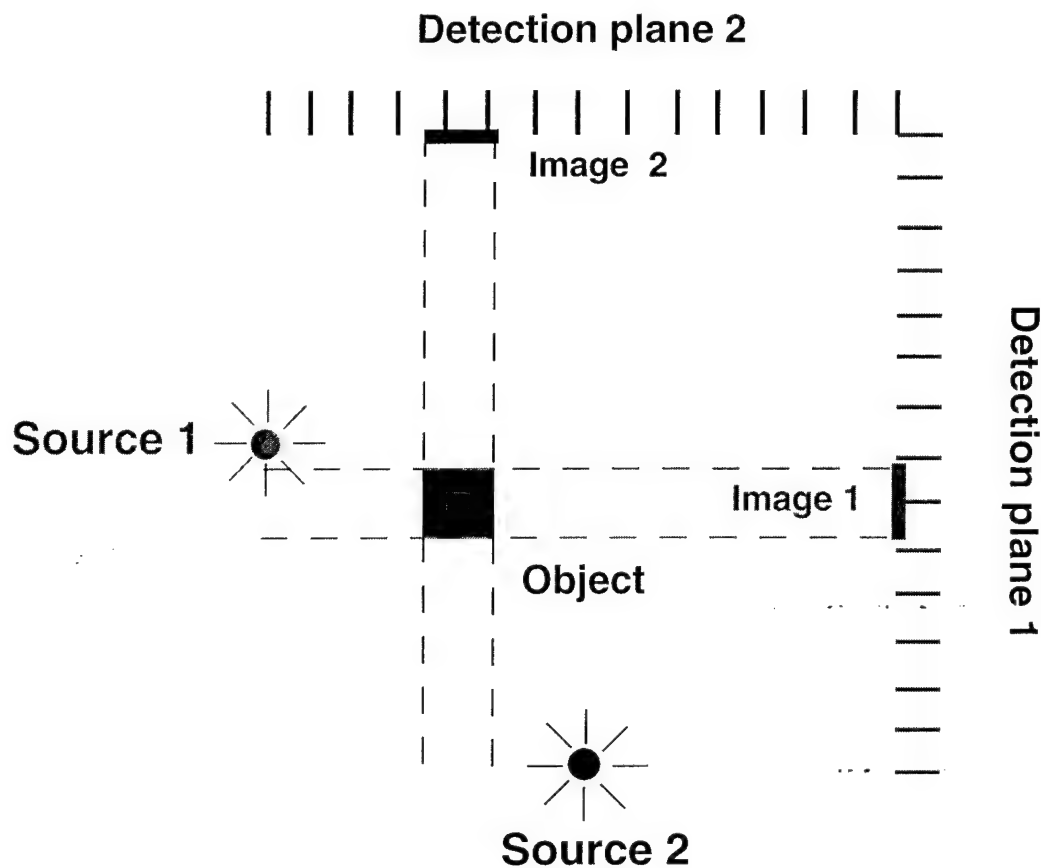


FIG. 8. Illustration of how to obtain a 3-D image from two projection images reconstructed from two measurements along two orthogonal directions. Image 1 from the measurement in plane 1 provides the depth information for image 2 from the measurement in plane 2.

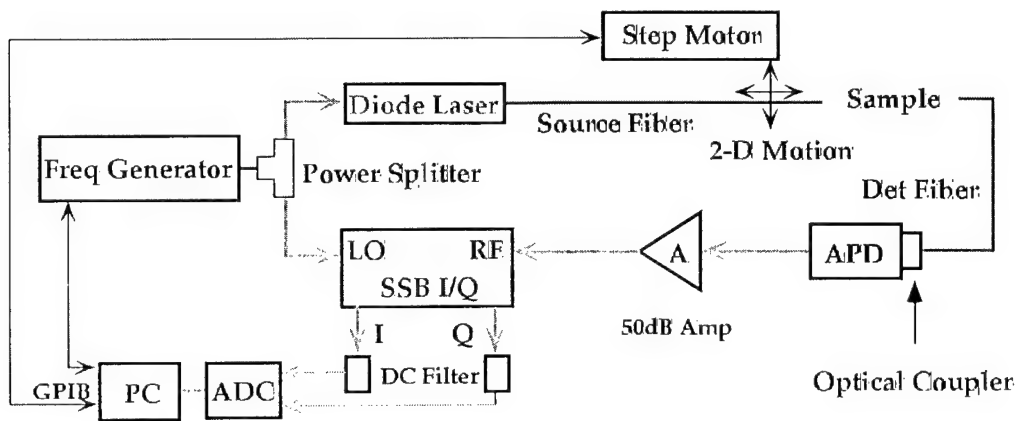


FIG. 9. Block diagram of the homodyne setup. APD-Avalanche Photo Diode; A-Amplifier; SSB I/Q-Single Side Band In-phase/Quadrature-phase Demodulator; LO-Local Port; RF-Radio Frequency Port; ADC-Analog to Digital Converter; GPIB-General Purpose Interface Bus.

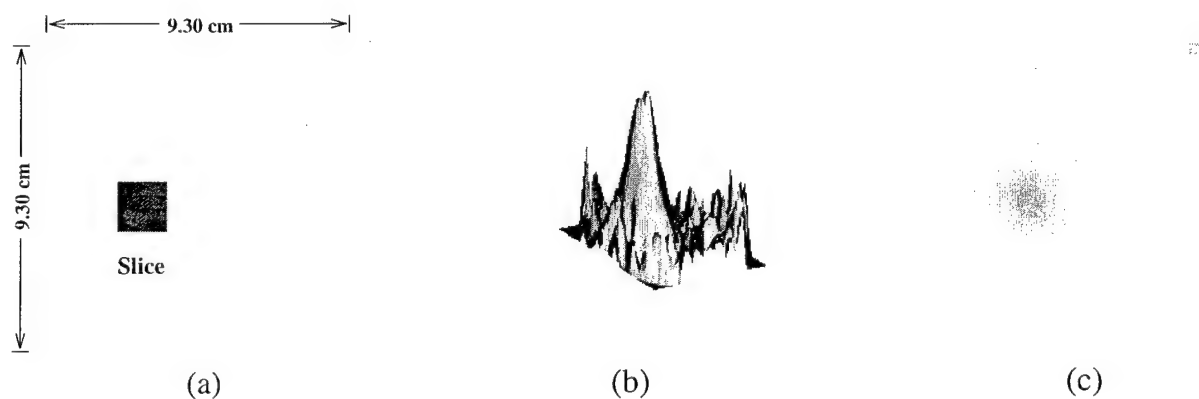


FIG. 10. (a) shows the exact x-y position of a thin absorbing slice. (b) shows the surface plot of the reconstructed absorption variation ($\delta\mu_a^{rec}$) using the angular spectrum algorithm. (c) illustrates the reconstructed 2-D photographic image of this slice. Agreement between the reconstructed position and the exact position as shown in (a) can be readily found.

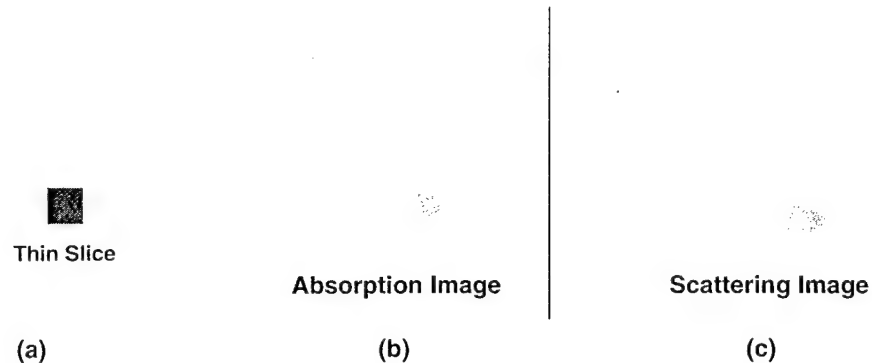


FIG. 11. (a) shows a thin slice object at $(1, -1, 3)$ cm. The slice is 0.3 cm thick with its $1 \times 1 \text{ cm}^2$ surface in parallel to the detection plane at $z_d = 5$ cm. The scattered waves at two modulation frequencies (70 MHz and 140 MHz) in the detection plane at $z_d = 5$ cm are calculated using finite difference method over a $9.3 \times 9.3 \text{ cm}^2$ region with x-y steps of 0.3 cm. (b) and (c) show the absorption and scattering images reconstructed simultaneously using the dual modulation frequency approach. The reconstructed position of the slice is close to its true position and the reconstructed absorption and scattering properties are close to their true values. See Section VI(A) for details.

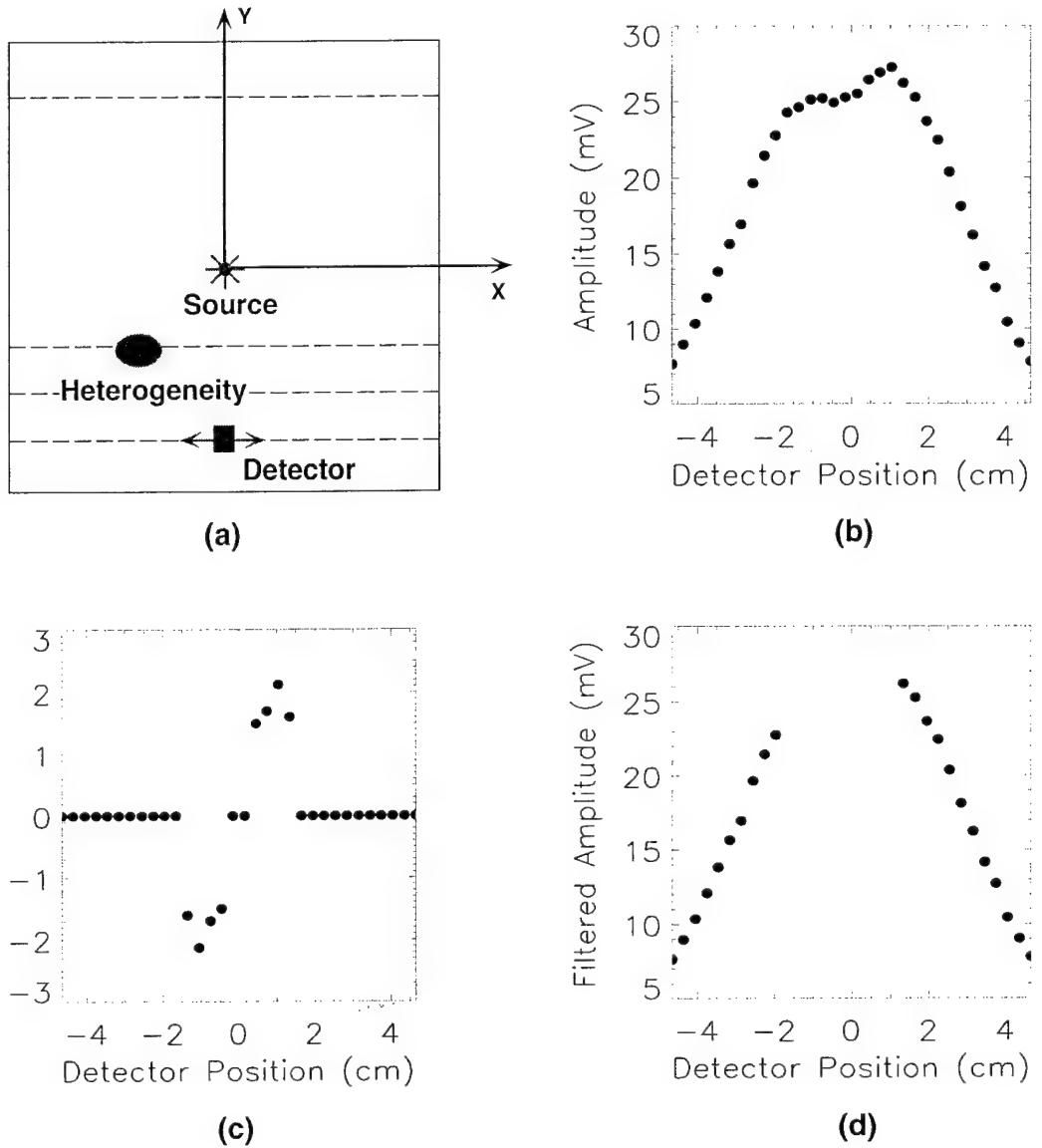


FIG. 12. (a) shows a 2-D version of the experimental geometry in Fig. 2. The detector scans along a line from left to right symmetrically with respect to the source. (b) shows the raw data measured on a heterogeneous medium by scanning the detector along a line from left to right. (c) shows the most perturbed data points for which the left and right differences are greater than the noise level of our detection system (e.g., 2.5 mV in this case). (d) show the rest data points after the most perturbed data points are filtered out. The background optical properties can then be obtained by fitting the data points shown in (d) to a homogeneous model.

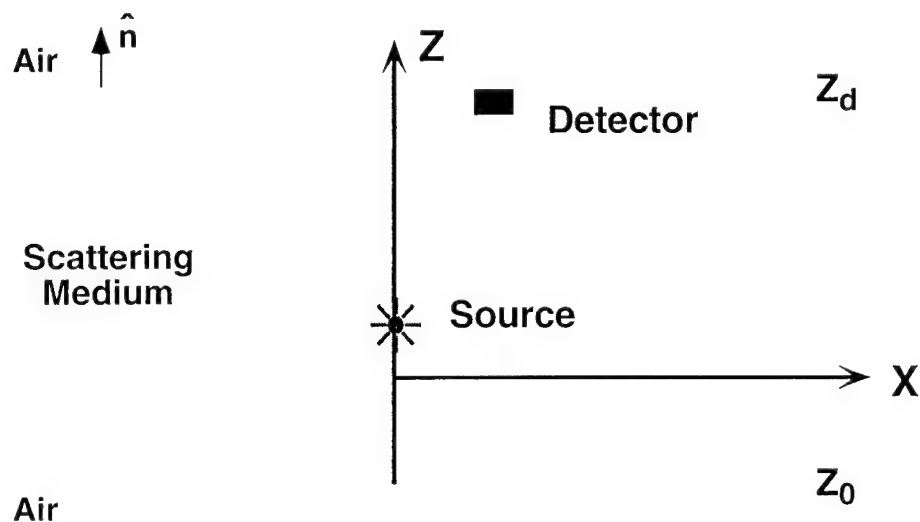


FIG. 13. A slab geometry is considered for the boundary problem. The slab is infinite long but has a finite thickness, e.g. $z_d - z_0$. One surface of the slab is at plane $z = z_0$ and another surface is at plane $z = z_d$. The turbid medium is between these two planes and outside the slab is non-scattering media such as air. This slab geometry is quite suitable for a compressed breast configuration in clinical studies.

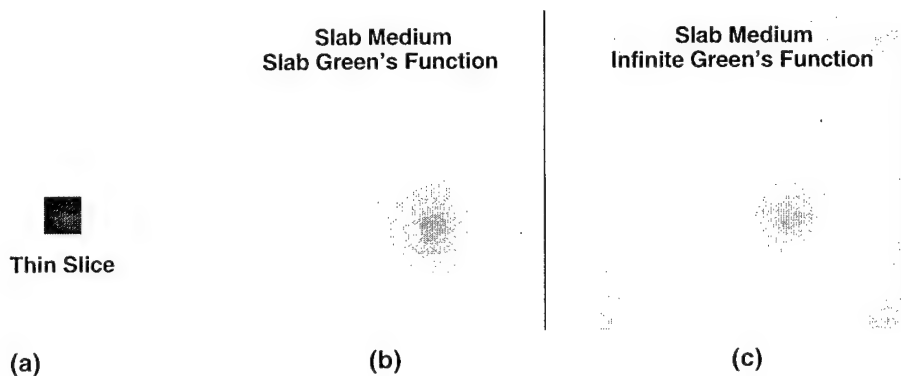


FIG. 14. (a) shows the position of a 0.3 cm thick, 1.0×1.0 cm 2 absorbing slice at (1, -1, 3) cm in a slab turbid medium. The two surfaces of the slab are respectively at planes $z=0$ cm and $z=5$ cm. The source is at origin at one of the slab surface ($z=0$ cm) and the detector scans at the other surface ($z = 5$ cm). The reconstructed absorption image using the “slab” Green’s function (Eq. (49)) is shown in (b). The reconstructed absorption image using the *wrong* “infinite” Green’s function (Eq. (19)) is shown in (c).

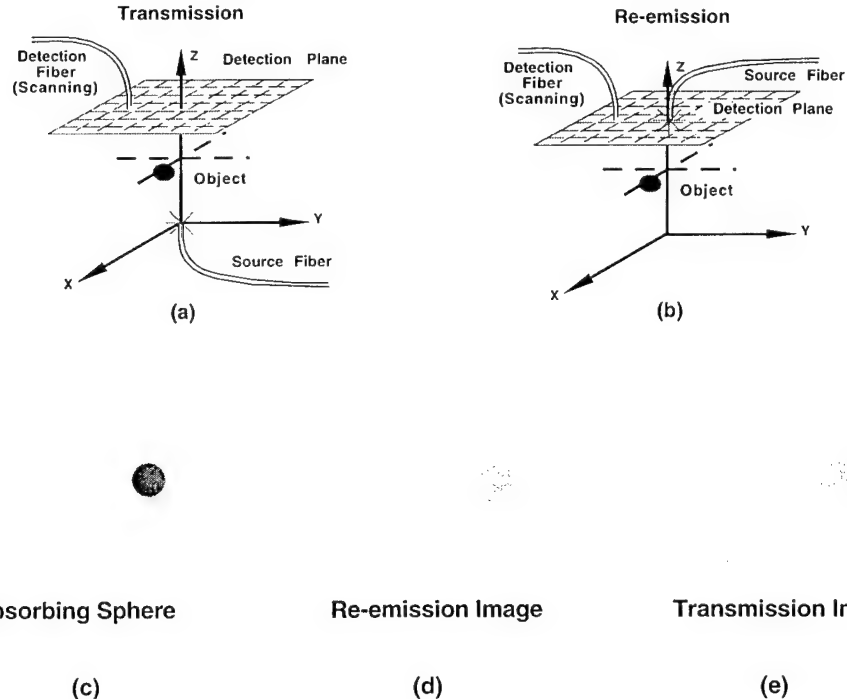


FIG. 15. (a) shows the transmission geometry. The source is at the origin and the detector scans in a plane at $z = z_d$. (b) shows the re-emission geometry where the source is at the center of the detection plane at $z = z_d$. (c) illustrates a spherical absorbing object at $(2, 1, 2)$ cm embedded within a slab turbid medium. The two surfaces of the slab are at $z_0 = 0$ cm and $z_d = 4.0$ cm, respectively. For both transmission and re-emission geometries, the scattered waves in the detection plane at $z_d = 4$ cm are calculated using the exact DPDW solution for a slab geometry over a 9×9 cm^2 region with x-y steps of 0.6 cm. The reconstructed images for the re-emission and transmission geometries are shown in (d) and (e), respectively. The two images look similar. We also found that the reconstructed absorption coefficients are also about the same under both geometries.

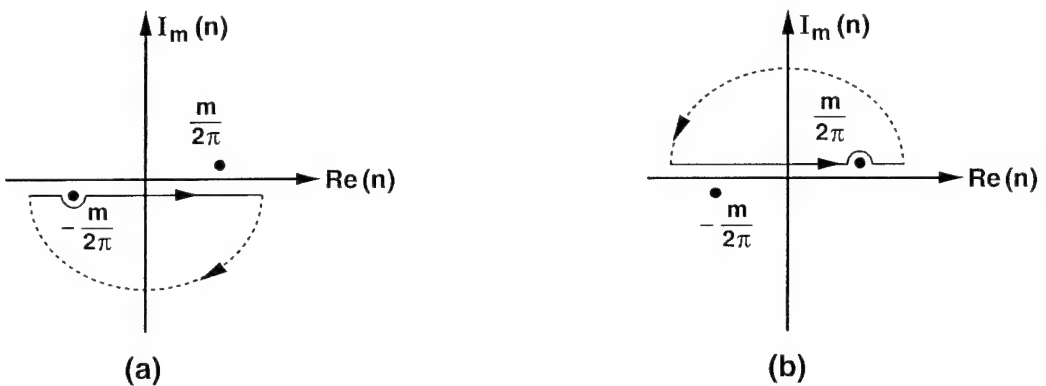


FIG. 16. There are two poles for the integral over n in Eq. (B6). (a): for $z > 0$ the singularity is at $n = -m/2\pi$ and the integral is done along the lower close curve; (b): for $z < 0$ the singularity is at $n = m/2\pi$ and the integral is done along the upper close curve.

Tissue Bulk Optical Properties of Breasts and Phantoms Obtained with Clinical Optical Imager

Turgut Durduran, M. Holboke, J. P. Culver, L. Zubkov, R.
Choe, D.N.Pattanayak, B. Chance* & A. G. Yodh

Department of Physics & Astronomy,

** Department of Biophysics & Biochemistry,*

University of Pennsylvania, Philadelphia, PA 19104

Phone: 215-898-5148, 215-573-6391, durduran@mail.sas.upenn.edu

Abstract:

A Clinical, compression-plate diffuse optical imager is used to determine the bulk optical properties and blood saturation in breast tissue of volunteers and in tissue phantoms.

© 1999 Optical Society of America

OCIS codes: (170.3830) Mammography; (170.5270) Diffuse Photon Density Waves; (170.3660) Light Propagation in tissues; (170.5280) Photon Migration

Diffuse optical tomography (DOT) in the near-infrared (NIR) is currently emerging as a viable means for breast tumor imaging and specification[1]. This method relies on optical properties and biological factors such as the blood oxygen saturation to enhance tumor specificity and sensitivity. It is important to study the dispersion of normal breast bulk optical properties in order to asses the contrast expected from tumor tissue. For example, various factors such as age and the menstrual cycle are expected to influence the optical properties[2] and should be characterized.

In this study we employ a clinical, compression-plate optical breast imager for measurements. The instrument uses three wavelengths - 830nm, 786nm and 750nm, and employs a scanning, fiber-coupled PMT detector for detection. The lasers are coupled to sixteen different source positions and a dicon multiplexer is used to select the source position. In our clinical measurements so far we have been using single source position due to time constraints. The lasers are modulated at 140MHz to produce a diffuse photon density wave (DPDW) in the medium. The patient lies in the prone position and her breast is inserted into a small tank filled with a matching solution of Intralipid through an opening on the bed. The detector scans along the output plate glass surface, and the source is attached to a compression plate which applies a gentle compression to the breast. Usually the range of compression is 4.5cm to 7cm. It takes \approx 15 minutes to acquire data from a 9.6cm (x) by 4.8cm (y) scan region with 153 (17x9) points. We take two sets of data for each patient; 1) tank filled with Intralipid only, i.e without the breast, which allows us normalize for instrument response, 2) tank filled with Intralipid and the patient breast. For the last six months we have been acquiring data at the Hospital of University of Pennsylvania from volunteers with normal breasts.

In order to test the feasibility of our instrument and approach we also performed phantom measurements using balloons filled with different concentrations of ink and Intralipid. The balloons were inserted into the Intralipid tank to fill a volume which is similar to the average breast volume obtained from the clinical trials. A large fraction of the balloon was kept above the Intralipid level to simulate the chest wall. For analysis we follow the same procedure as done with the healthy patients. We have tested nine phantoms with different optical properties, different background optical properties and different volumes. Here we show the results from 786nm. The results from the other wavelengths are comparable.

To estimate bulk optical properties we solve the forward diffusion problem numerically using a finite difference solver for arbitrary heterogeneities in the domain [3, 4]. To obtain the bulk properties we specialize this approach, segmenting the image volume into Intralipid background and breast volumes (see fig.(1)). During the measurement we obtain an outline of the breast in the x-y plane, and the y-z plane in order to define the segmentation geometry. The top x-z segmentation plane wall, however, is assumed to extend far above the Intralipid level in the tank and thus models the rest of the chest. Therefore, we end up with a three dimensional T-shaped heterogeneity that approximates the breast volume as illustrated in fig. (1). The relevant boundaries are also shown.

An inverse solver based on this solution which in its simplified version can be used to obtain the bulk properties of the heterogeneity volume was developed. First we divide the heterogeneous data by the background data giving a "normalised" DPDW. The solver is then initialized with the background properties, convergence is tested as the squared difference between the measured and calculated normalized DPDWs. If it did not converge, then the optical properties are updated according to a rule based on distorted born iterative method and the forward solution is tested for convergence once more. The process is repeated until either a particular number of iterations is reached or a certain criterion in the error is achieved. Here we simplified this process for the bulk properties by summing up the

weight matrices (essentially averaging) in the solver for the heterogeneity region and by not allowing the properties of the homogenous background region to change (as opposed to calculating every single voxel in the domain). We allowed for a maximum of ten iterations and stopped earlier if the error falls below 10^{-6} . We find that this criterion is generally adequate for our numerical simulations and phantom tests.

To illustrate our results, we show four sets of data from balloon phantoms as follows where the balloon volume and other parameters were kept constant but the optical properties were changed. The background properties were 0.05 and 8 cm^{-1} for the absorption (μ_a) and scattering (μ_s') coefficients respectively.

Expected (cm ⁻¹)		Calculated (cm ⁻¹)	
Absorption	Scattering	Absorption	Scattering
0.05	12	0.0587	13.54
0.05	4	0.0575	4.90
0.035	8	0.0446	8.64
0.07	8	0.0696	9.26

We also calculated the optical properties for these phantoms (total of nine) using a semi-infinite fit for the data from a strip of width $\approx 1.5 \text{ cm}$ at the top part of the scanning region. This geometry is commonly employed and was used earlier by us [4] to obtain estimates of the breast optical properties. We believe that the main drawback of the semi-infinite model is that it ignores the multi-layer boundary structure such as the tissue -Intralipid boundaries. It tends to underestimate μ_s' and both μ_a and μ_s' "saturate" at higher values of absorption and scattering.

The results from both methods are shown in fig.(2) where we plot the mean calculated properties vs the expected values from multiple measurements for each phantom. The error bars are derived from the standard deviations from the expected values. We see that the correlation with the expected values for the finite difference method is within 10% whereas for the semi-infinite model it is worse than 45%.

We then apply this method for the data from healthy volunteers. Fig. (3) shows the histograms of optical properties and also the blood saturations for seven of these patients. The optical properties are well within the generally accepted values. The blood saturation values are also generally satisfactory[6]. The very low saturation value in one case is probably due to a systematic error.

We are currently acquiring more data with healthy patients and we still have a large data set obtained that needs to be analyzed. The model is also being tested thoroughly with more robust phantoms. This work will be presented in April.

References

1. For a recent review of the field see relevant sessions in International Symposium of Biomedical Optics, SPIE Proc., (San Jose, CA, Jan 1999)
2. Thomsen S, Tatman D,"Physiological and pathological factors of human breast disease that can influence optical diagnosis", Adv. Opt. Biop. Opt. Mammo., Ann. NY Acad. Sci., 838: 171-193 (1998)
3. M. Holboke, J. Fishkin, B. J. Tromberg and A. G. Yodh, "Three dimensional diffuse optical mammography with ultrasound localization in a human subject", Journal of Biomedical Optics (submitted for publication, Oct. 1999).
4. T. Durduran, J.P.Culver, M.J.Holboke, X. D. Li, L. Zubkov, B.Chance, D.N. Pattanayak and A.G.Yodh, "Algorithms for 3D localization and imaging using near-field diffraction tomography with diffuse light/Initial Clinical Applications ", Adv. in Opt. for Biotech., Med. and Surg., United Engr. Found.Mtg, (Kona, Hawaii, Aug. 1999)
5. R. C. Haskell, L. O. Svaasand, T. Tsay, T. Feng, M. S. McAddams, B. J. Tromberg, "Boundary Conditions for the diffusion equation in radiative transfer", J. Opt. Soc. Am. A, 11:2727-2741 (1994)
6. Chance. B, "Near-infrared images using continuous, phase-modulated, and pulsed light with quantitation of blood and blood oxygenation", Adv. Opt. Biop. Opt. Mammo., Ann. NY Acad. Sci., 838:19-45 (1998)

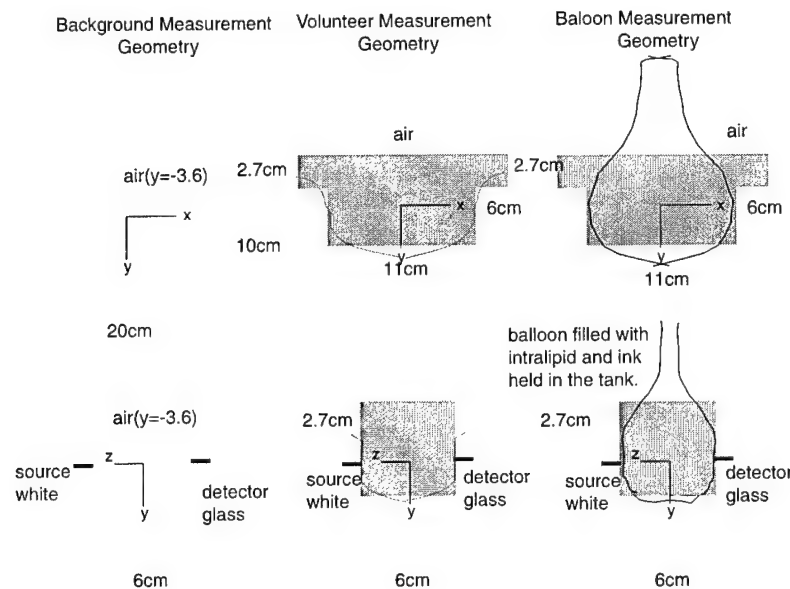


Fig. 1. Models used for finite difference calculations; background (left), breast (middle) and balloon phantom (right) are shown with the corresponding boundaries. The shaded regions show the estimated breast volume in the segmentation process.

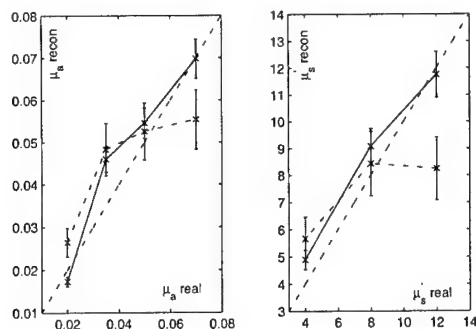


Fig. 2. The mean calculated absorption (scattering) coefficient vs the expected absorption (scattering) coefficient is shown on the left (right). Solid (dashed) lines show the finite difference (semi-infinite) calculations. The equality line (dotted) is also shown. The error bars are obtained from the standard deviations from the equality line.

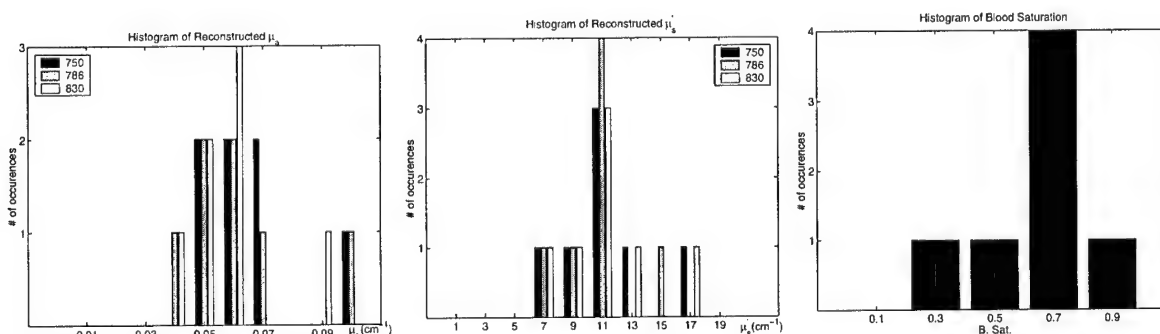


Fig. 3. Histograms of calculated bulk absorption, scattering coefficients and the blood saturation of the normal volunteers' breasts.

Data set size and image quality in diffuse optical mammography: evaluation of a clinical prototype.

J.P. Culver, V. Ntziachristos, L. Zubkov, T Durduran, D.N. Pattanayak, A.G. Yodh

Dept. of Physics, Univ. of Pennsylvania Philadelphia, PA

culver@sol1.lsrm.upenn.edu

Abstract: A diffuse optical tomographic imager is described. It employs a large area CCD to collect large data sets (10^5 measurements) from 32 sources rapidly (30s). 3D images of breast tissue phantoms exhibit ~5mm resolution.

©1999 Optical Society of America

OCIS codes: (179.3830) Mammography, (170.5270) Diffuse Photon Density Waves, (170.3660) Light Propagation in tissues; (170.5280) Photon Migration

1. Introduction

Diffuse optical tomographic (DOT) techniques have paved the way for several groups now focusing on clinical research[1]. However several challenges remain for developing a clinically useful tool. One of the main experimental challenges is to increase the speed and size of the data set collected. Coverage and resolution demand larger data sets and yet patient movement and physiologic noise necessitate fast collection speeds. A generally held view is that DOT techniques may be limited to between 2 -10 mm resolution in deep breast tissue. One might naively assume that a similar sampling density would be sufficient. For typical breast volumes (~1000cc) this would necessitate between 10^3 (1cm resolution) and 10^5 (2mm resolution) measurements. However some surface features have sub millimeter structure and are near the high sensitivity regions of the reconstruction volumes. For these surface structures it may be advantageous data set sizes of greater than 10^6 . Most clinical prototypes thus far have much smaller data sets, i.e. in the range of 10^1 to 10^3 . We therefore anticipate the potential for machines with larger data sets and rapid acquisition to substantially improve upon existing optical mammography devices.

A natural tool for spatially dense light sampling is a CCD. There has been some outstanding work in the biomedical optics field using and developing CCD systems for diffuse light diagnostics, though these have not yet applied to clinical mammography. Time-resolved (80psec resolution)/2D-space-resolved measurements have been carried out by Alfano and coworkers[2,3]. Using this instrumentation they have localized a fluorescent object in chicken breast, and they have begun to work on the general image reconstruction problem in phantoms. In the frequency domain Sevick-Muraca's group has adapted homodyned multi-pixel RF phase-sensitive camera technique for deep-tissue imaging [4,5]. They have measured images of DC/AC amplitude and phase of a tissue phantom with absorbing and fluorescent heterogeneities. They have even used the system for investigation of in-vivo and ex-vivo animal models with mammary cancer. Boas and coworkers have also recently applied CCDs in remission geometry's; in particular they use a single source and simply measure the diffuse light amplitude in remission[6]. In total this work, and related reconstruction work with DC data [7], demonstrates the feasibility of using CCD's to collect data and as well as the surprising utility of DC amplitude only data for image reconstruction. To this end we have developed clinical prototype DOT imager using a larger area CCD camera. This CW imager will be integrated into a existing slower scanning RF imager that we are currently employing to study bulk breast tissue optical properties.

The system we have built introduces several new ideas. Most important are the 32 different transmitted image projections of the illuminated volume. This is crucial for tomographic analysis of the data. In Figure (1) we illustrate our new compression plate, intralipid tank and CCD imaging system. The compression plate and Intralipid tank have been mechanically redesigned compared to our previous system. In particular the positional repeatability and to stability of the moving compression plate relative to the detection window were improved. In addition a modular viewing window permits the use of diffuse or antireflective transparent windows. Our CCD consists of a 1300x1340 pixel array in an area of ~2.6cm x 2.6 cm. The CCD chip is read by a 16 bit A/D and thermoelectrically cooled (-40°C). We have checked the light transmission through a range of tissue phantoms of different thicknesses in order to ascertain the signal-to-noise of the CCD system. We chose a fairly large source-detector plate separation range (~5-8cm), and made an Intralipid tissue phantom with μ_a 0.05 cm⁻¹ and μ_s' =10 cm⁻¹. The raw CCD measurements were binned in 8x8 square units to give an equivalent pixel size of 2mm on the breast surface. Using

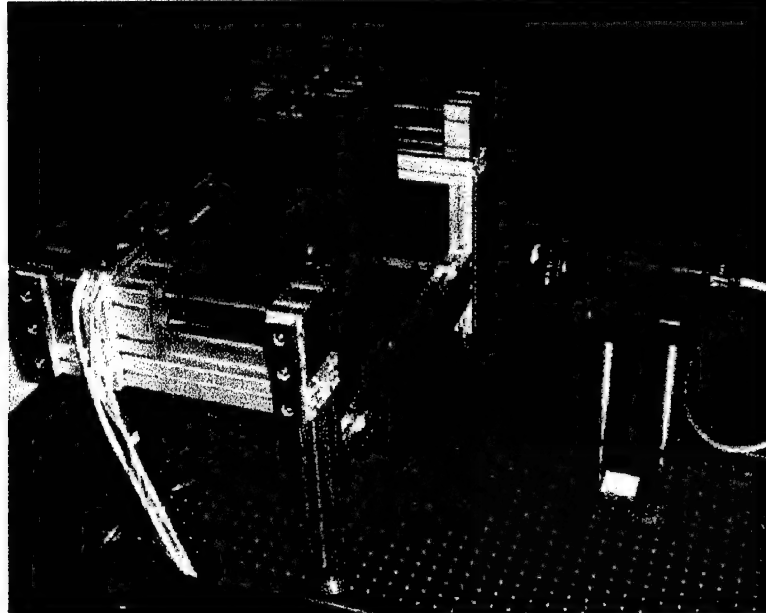


Figure 1. CCD imaging system and Intralipid tank with movable compression plate. The modular viewing window can be either a diffuse resin window ($\mu_a=0.02\text{cm}^{-1}$, $\mu_s'=10\text{cm}^{-1}$) or a transparent window. A 10-mW, 809nm, laser light source is optically switched between 32 fibers arranged in a hexagonal lattice within the compression plate. An average of 4mW is delivered to the fiber tips. A 50mm F#=1.4 lens images the detection plane on to the CCD chip. Ambient room light is eliminated using a RG-9 optical glass filter and light shielding materials.

known detector efficiency and gain the image was converted to photoelectron values, and the signal-to-noise was assumed to scale as $1/\sqrt{N_{\text{photoelectrons}}}$. From our clinical measurements we know that most breast compressions are $\sim 6\text{cm}$. However we find that even for a larger breast compression of 7 cm we can collect $\sim 3 \times 10^3$ light measurements with a S/N of better than $\sim 1\%$ over 100cm^2 area. With 32 available sources we reach a total of 10^5 measurements in ~ 30 seconds.

Figure (2) shows the results from a measurement made with two (T_A and T_B) absorbing $5\times 5\times 10\text{ mm}$ targets in a suspension of Intralipid with a source-detector plane distance of 5.5cm . The source plane is at $y=0$ and the detector plane is at $y=5.5\text{cm}$ with x -axis oriented horizontal and z -axis oriented vertical. The bulk intralipid tissue phantom had $\mu_a=0.05\text{ cm}^{-1}$ and $\mu_s'=10\text{ cm}^{-1}$ and the targets (T_A, T_B) had ($\mu_a=0.3\text{ cm}^{-1}$, $\mu_a=0.2\text{ cm}^{-1}$) respectively. The centers of the two objects were located in the middle of the intralipid tank with ($T_A, x=-0.5, y=2.5, z=0$) and ($T_B, x=1.5, y=2.5, z=0$). T_A aligned along the z -axis and T_B aligned along the x -axis. To demonstrate the tomographic capabilities of the data, 3d images were reconstructed using a Rytov perturbation approach with ART matrix inversion. For these preliminary studies computing restrictions necessitated that we use a subset of the available data. In particular the central six sources were used located at $z=0$ and spaced evenly at 1.4cm steps in the x direction. The detectors were then binned to $4.6\times 4.6\text{ cm}$ area measurements covering a $\sim 4\times 10\text{cm}$ field of view with 19 positions in x and 11 positions in z . A total of 1254 measurements were available. From this total detector set a

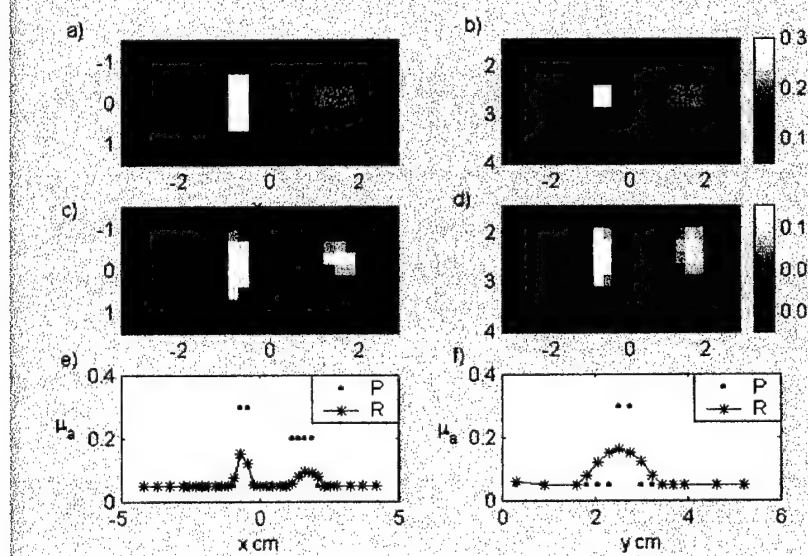


Figure 2. The central $6\times 2.5\times 2.5$ volume (x, y, z) of the entire $10\times 5.5\times 4\text{cm}$ volume. Two slices of the 3D μ_a image maps are shown, a) xz plane at $y=2.5\text{cm}$ for the phantom b) xy plane at $z=0$ for the phantom, c) xz plane at $y=2.5\text{cm}$ for the reconstruction d) xy plane at $z=0$ for the reconstruction, e) e) Cross sections at $y=0, z=0$. f) Cross section at $x=-0.5, z=0$.

reduced data set was selected using a noise threshold defined relative to the peak light intensity for each source. Ultimately 1001 total measurements were used for the reconstruction's. Using rytov absorption weights, the 10x5.5x4cm (x,y,z)volume was meshed in 2.3x2.3x2.3mm voxels. An Algebraic Reconstruction Technique (ART) was used to invert the measurements and obtain the 3D μ_a images. Figure 2 shows the central slices in the xz plane (at y=0) and the xy plane (at z=0) for the (a&b) actual μ_a values and (c&d) the reconstructed values. For quantitative comparison the 1 dimensional cross sections e) in the x direction at y=0,z=0 and f) in the y direction at x=-0.5,z=0 are shown. Note that the orientations of the two objects in the xz plane are observable. Thus the resolution in the xz plane is ~5mm. The reconstructed values are ~2 times smaller than expected. This can be attributed to the reduced (~1cm) resolution in the y direction that spreads the optical weight over a larger volume leaving the total integrated signal $\delta\mu_a^*volume$ the same. It is anticipated that reconstruction's that utilize more of the available source views will improve on the resolution in the y direction and correspondingly the quantification of the optical properties.

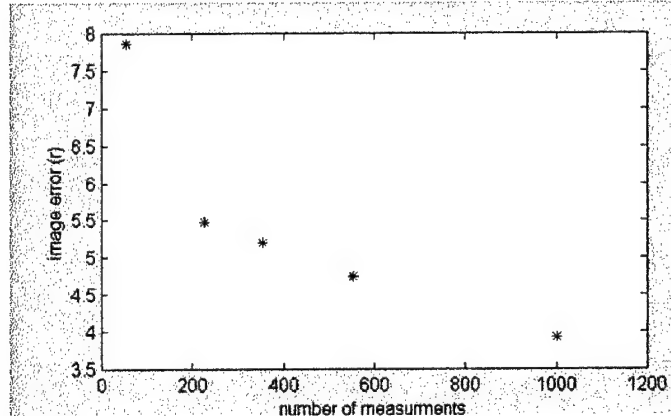


Figure 3. Image error (r) as a function of the number of measurements used in the 3D reconstruction.

we are continuing to improve the image quality as we increase are measurements. With more heterogeneous samples the effects will be even more pronounced. Future work will extend this analysis to larger data sets and more complex tissue phantoms.

In conclusion we have developed a clinical prototype DOT imager using a larger area CCD camera that records 10^5 measurements in 30 seconds. This is a significantly larger data set obtained more quickly than typical existing clinical optical mammography machines. Preliminary 3D reconstructions of tissue phantom demonstrate ~5mm resolution with a limited data set. We will integrate this system into a existing slower scanning RF imager that we are currently employing in the clinic.

To test the effect of data size an image quality criteria is needed. For our comparison we use a standard image error function (ref) applied to the central xz plane. In particular we define

$$r = \sum_{i=1}^Y \sum_{j=1}^X |t_{i,j} - r_{i,j}| / \sum_{i=1}^Y \sum_{j=1}^X |t_{i,j}|$$

where X, Y are the dimension in voxels of the reconstructed image, t is the expected optical property, and r is the reconstructed optical property. The data size is altered by sparsely selecting the pixels while leaving the field of view constant. Figure 3 shows the error as function of data set size. Here the true noise threshold truncated data size is used. Note that

References:

- For a recent review of the field see relevant sessions in International Symposium of Biomedical Optics, SPIE Proc., (San Jose, CA, Jan 1999)
- Cai, W., Gayen, S.K., Xu, M., Zevalls, M., Alrubaei, M., Lax, M., and Alfano, R.R., Optical tomographic image reconstruction from ultrafast time-sliced transmission measurements, *Applied Optics* 38, 4237-4246 (1999).
- Gayen, S.K., Zevalls, M.E., Alrubaei, M., Evans, J.M., and Alfano, R.R., Two-dimensional near-infrared transillumination imaging of biomedical media with a chromium-doped forsterite laser, *Applied Optics* 37, 5327-5336 (1998)
- Reynolds, J.S., Troy, T.L., Mayer, R.H., Thompson, A.B., Waters, D.J., Cornell, J.J., Snyder, P.W., and Sevick-Muraca, E.M., Imaging of spontaneous canine mammary tumors using fluorescent contrast agents, *Photochemistry and Photobiology* 70, 87-94 (1999).
- Reynolds, J.S., Troy, T.L., and Sevick-Muraca, E.M., Multipixel techniques for frequency-domain photon migration imaging, *Biotechnology Progress* 13, 669-680 (1997).
- Cheng, X., Boas, D.A., Diffuse optical reflection tomography with continuous-wave illumination, *Optics Express* 3, 118-123 (1998).
- Jiang, H.B., Paulsen, K.D., Osterberg, U.L., and Patterson, M.S., Improved continuous light diffusion imaging in single- and multi-target tissue-like phantoms, *Physics in Medicine and Biology*, 43, 675-693 (1998).

Diffuse optical 3D-slice imaging of bounded turbid media using a new integro-differential equation

Deva N. Pattanayak *and A. G. Yodh

Department of Physics & Astronomy, University of Pennsylvania
Philadelphia, PA 19104-6396

Also with Silicon Power Corporation, Latham NY 12110

pattanayak@aol.com; yodh@dept.physics.upenn.edu

Abstract: A new integro-differential equation for diffuse photon density waves (DPDW) is derived within the diffusion approximation. The new equation applies to inhomogeneous bounded turbid media. Interestingly, it does not contain any terms involving gradients of the light diffusion coefficient. The integro-differential equation for diffusive waves is used to develop a 3D-slice imaging algorithm based on the angular spectrum representation in the parallel plate geometry. The algorithm may be useful for near infrared optical imaging of breast tissue, and is applicable to other diagnostics such as ultrasound and microwave imaging.

©1999 Optical Society of America

OCIS codes: (170.3010) Image reconstruction techniques; (170.5280) photon migration; (170.3830) mammography; (170.5270) Photon density waves; (170.3660) Light propagation in tissues

References and links

1. B. Chance, Q. M. Luo, S. Nioka, D. C. Alsop and J. A. Detre, "Optical investigations of physiology: a study of intrinsic and extrinsic biomedical contrast," *Phil. Trans. Roy. Soc. London B.* **352**, 707 (1997).
2. A. Villringer and B. Chance, "Non-invasive optical spectroscopy and imaging of human brain functions," *Trends. Neurosci.* **20**, 435 (1997).
3. Y. Hoshi and M. Tamura, "Near-Infrared Optical Detection of Sequential Brain Activation in The Prefrontal cortex during mental tasks," *Neuroimage*. **5**, 292 (1997).
4. J. H. Hoogenraad, M. B. van der Mark, S. B. Colak, G. W. 't Hooft, E. S. van der Linden, "First Results from the Philips Optical Mammoscope", *Proc. SPIE / BiOS-97* (SanRemo, 1997).
5. J. B. Fishkin, O. Coquoz, E. R. Anderson, M. Brenner and B. J. Tromberg, "Frequency-domain photon migration measurements of normal and malignant tissue optical properties in a human subject," *Appl. Opt.* **36**, 10 (1997).
6. M. A. Franceschini, K. T. Moesta, S. Fantini, G. Gaida, E. Gratton, H. Jess, W. W. Mantulin, M. Seeber, P. M. Schlag and M. Kaschke, "Frequency-domain instrumentation techniques enhance optical mammography: Initial clinical results" *Proc. Natl. Acad. Sci. USA*, **94**, 6468-6473 (1997).
7. S. K. Gayen and M. E. Zevallos, B. B. Das, R. R. Alfano, "Time-sliced transillumination imaging of normal and cancerous breast tissues," in *Trends in Opt. And Photonics*, ed. J. G. Fujimoto, M. S. Patterson.
8. B. W. Pogue, M. Testorf, T. McBride, U. Osterberg and K. Paulsen, "Instrumentation and design of a frequency-domain diffuse optical tomography imager for breast cancer detection," *Opt. Express* **1**, 391 (December 1997). <http://pubs.osa.org/oarchive/source/2827.htm>
9. D. Grosenick, H. Wabnitz, H. H. Rinneberg, K. T. Moesta and P. M. Schlag, "Imaging and Characterization of Breast tumors using a laser-pulse mammograph," *SPIE* 3597 (1999).
10. A. G. Yodh, B. Chance, "Spectroscopy and imaging with diffusing light," *Phys. Today* **48**, 34-40 (March 1995).

11. H. Jiang, K. D. Paulsen, U. L. Osterberg, B. W. Pogue and M.S. Patterson, "Optical Image reconstruction using frequency-domain data: Simulations and experiments," *J. Opt. Soc. Am. A* **13**, 253-266 (1996).
12. Y. Yao, Y. Wang, Y. Pei, W. Zhu and R. L. Barbour, "Frequency-domain optical imaging of absorption and scattering distributions using a born iterative method," *J. Opt. Soc. Am. A* **14**, 325-342 (1997).
13. S. R. Arridge, "Forward and inverse problems in time-resolved infrared imaging," in *Medical Optical Tomography: Functional Imaging and Monitoring*, ed. G. Muller, B. Chance, Rl. Alfano, S. Arridge, J. Beuthan, E. Gratton, M Kaschke, B. Masters, S. Svanberg, P. van der Zee, *Proc SPIE IS11*, 35-64 (1993).
14. An integro-differential equation valid for infinite medium, but containing no gradient of Diffusion constant was used for image reconstruction by M. A. O'Leary, D. A. Boas, B. Chance, A.G. Yodh, "Experimental Images of heterogeneous turbid media by frequency-domain diffusing-photon tomography," *Opt. Lett.* **20**, 426-428 (1995).
15. An anonymous reviewer has brought to our attention a recent paper by S.R.Arridge and W.R.B. Lionheart, "Non-uniqueness in diffusion based optical tomography," *Opt. Lett.* **23**, 882-884 (1998), which deals with the second order derivative of the diffusion coefficient.
16. D. N. Pattanayak and E. Wolf, "Resonance States as Solutions of the Schrodinger Equation with a Non-Local Boundary Condition," *Phys. Rev. D* **13**, 2287(1976).
17. J. L.Ye,R.P.Millane, K. J. Webb and T. J.Downar, "Importance of the gradD term in frequency resolved optical diffusion imaging." *Opt. Letters*,**23**,1998.
18. K. M.Case and P. F.Zweifel, in *Linear Transport Theory* (Addison -Wesley,MA,1967).
19. A.Ishimaru, *Wave Propagation and Scattering in Random Media* (Academic Press, New York, 1978) Vol.. 19.
20. P. M.Morse and H. Feshbach, *Methods of Theoretical Physics* (McGraw-Hill,1953).
21. Claus Muller, *Foundations of the Mathematical theory of Electromagnetic Waves* (Springer-Verlag,New York,1969).
22. H. Weyl, *Ann. Phys.* **60**, 481, (1919).
23. See, also , A.J. Banos, in *Dipole Radiation In the Presence of a Conducting Half-Space* (Pergamon Press, New York, 1966).
24. E. Wolf, "Principles and Development of Diffraction Tomography" in *Trends in Optics*, ed. A. Consortini (Academic Press, San Diego, 1996).
25. A. J.Devaney, "Reconstructive tomography with diffracting Wavefields," *Inv. Probl.*,**2**,161-18391986).
26. For an application of diffraction tomography to near field diffusion wave imaging and an analytical expression relating theoretical resolution and tissue thickness see, GE Class I Technical report (publicly available on request) by D. N. Pattanayak, "Resolution of Optical Images Formed by Diffusion Waves in Highly Scattering Media," GE Tech. Info. Series **91CRD241** (1991).
27. C. L. Matson, N. Clark, L. McMackin and J. S. Fender, "Three-dimensional Tumor Localization in Thick Tissue with The Use of Diffuse Photon-Density Waves," *Appl. Opt.* **36**, 214-219 (1997).
28. X.D.Li, T. Durduran, A.G. Yodh, B. Chance and D.N. Pattanayak, "Diffraction Tomography for Biomedical Imaging With Diffuse Photon Density Waves," *Opt. Lett.* **22**, 573-575 (1997).
29. Chen BQ, Stammes JJ, Stammes K, "Reconstruction algorithm for diffraction tomography of diffuse photon density waves in a random medium". *Pure Appl. Opt.* **7**, 1161-1180 (1998).
30. X. Cheng and D. Boas, "Diffuse Optical Reflection Tomography Using Continous Wave Illumination," *Opt. Express* **3**, 118-123 (1998); <http://epubs.osa.org/oarchive/source/5663.htm>
31. S. J. Norton, T. Vo-Dinh, "Diffraction Tomographic Imaging With Photon Density Waves: an Explicit Solution, *J. Opt. Soc. Am. A* **15**, 2670-2677 (1998).
32. J. C. Schotland, "Continuos Wave Diffusion Imaging," *J. Opt. Soc. Am. A* **14**, 275-279 (1997).
33. J. Ripoll, M. Nieto-Vesperinas, "Reflection and Transmission Coefficients of Diffuse Photon Density Waves," (to be published).
34. J. Ripoll and M. Nieto-Vesperinas, "Spatial Resolution of Diffuse Photon Density Waves, " *J. Opt. Soc. Am.A* (to be published).
35. J.C.L.Matson and H. Liu, "Analysis of the forward problem with diffuse photon density waves in turbid media by use of a diffraction tomography model," *J. Opt. Soc. Am. A* **16**, 455-466 (1999).
36. For the angular spectrum representation in a slab field and for an excellent account of the angular spectrum representation see, L.Mandel and E.Wolf, *Optical Coherence and Quantum Optics* (Cambridge University Press, New York,1995).

1. Introduction

Tomographic imaging of deep tissues with diffusive waves makes possible functional imaging based on novel optical contrasts derived from tissue chromophores, structure and metabolism [1-3]. The near-infrared spectroscopic properties of breast tumors for example, have been found to differ from adjacent normal tissues. Such spectroscopic signatures hold promise for increased tumor detection sensitivity and specificity [4-10]. In order to take full advantage of these new contrasts it is critical to develop high fidelity three-dimensional

optical imaging algorithms for diffusing light in turbid media such as the breast. To this end a number of image reconstruction schemes have been developed [11-13]. Many of these schemes use integral equations based on Born or Rytov approximations to generate a set of linear equations which are then solved to update the absorption and scattering coefficients associated with each voxel in the reconstructed volume. The integral formulation is attractive because of its speed. However, to our knowledge most of these formulations ignore terms involving gradients of the light diffusion coefficient [14,15] Although this approximation is often reasonably accurate, a recent paper [17] has established the importance of this gradient term, showing that its neglect is responsible for cross coupling between absorption and scattering images.

In this paper, we derive a new integro-differential equation for diffuse photon density waves (DPDW) within the diffusion approximation. The new equation, which is developed for bounded turbid media does not explicitly contain any terms involving gradients of the light diffusion coefficient. We then use this integro-differential equation and develop a theoretical inverse scattering algorithm for three-dimensional image reconstruction. The theoretical framework follows the principles of near-field diffraction tomography based on the angular-spectrum representation; in particular we show how to develop three-dimensional slice images of a breast compressed between two parallel plates. The technique employs a series of *plane* diffuse photon density waves with different modulation frequencies. For this set of plane incident diffusive waves, the algorithm requires two-dimensional FFT operations, and a one-dimensional matrix inversion. Thus the method is non-iterative in two space dimensions and is therefore computationally fast.

2. Integro-differential equation for diffuse photon density waves

We begin with the equations satisfied by the diffuse photon density, Φ and the diffuse photon flux density, \vec{J} [18]

$$\vec{J}(\vec{r}, \omega) = -\frac{\nabla \Phi(\vec{r}, \omega) - \vec{S}_1(\vec{r}, \omega)}{3\mu'_s(\vec{r}, \omega)} \quad (1)$$

$$\Phi(\vec{r}, \omega) = -\frac{\nabla \cdot \vec{J}(\vec{r}, \omega) - S_0(\vec{r}, \omega)}{\left(-\frac{i\omega}{c} + \mu_a(\vec{r}, \omega)\right)} \quad (2)$$

Here, ω denotes the modulation frequency of the source intensity, μ_a and μ'_s are the absorption and transport scattering coefficients of the bounded turbid media, c is the velocity of light in the medium and $S_0(\vec{r}, \omega), \vec{S}_1(\vec{r}, \omega)$ are the monopole and dipole moments of the intensity modulated optical source respectively. From these equations we eliminate the photon flux density and obtain, after a lengthy calculation, the following wave equation involving only the photon density function

$$\begin{aligned} (\nabla^2 + k_d^2) \Phi(\vec{r}, \omega) &= 3 \overline{\mu}'_s \delta \mu_a \Phi(\vec{r}, \omega) + \nabla \cdot \left(\frac{\delta \mu'_s}{\mu'_s} \nabla \Phi(\vec{r}, \omega) \right) \\ &\quad - \nabla \cdot \left(\frac{3\delta \mu'_s}{\mu'_s} \vec{S}_1(\vec{r}, \omega) \right) - 3\overline{\mu}'_s(\vec{r}) S_0(\vec{r}, \omega). \end{aligned} \quad (3)$$

Here

$$k_d^2 = 3\bar{\mu}'_s \left(\frac{i\omega}{c} - \bar{\mu}_a \right) \quad (4)$$

is the square of the complex wavenumber k_d . The bar over a physical parameter denotes spatial average of that parameter. Notice that for unmodulated source intensity (the continuous dc domain in contrast to the frequency domain), the photon density is a non-propagating damped wave. The wave number in this case is purely imaginary. For frequency modulated source intensity, the wave number is complex and the photon density acquires the characteristics of a damped or attenuated wave.

Because of its differential nature Eq. (3) will admit many solutions and boundary conditions are necessary to obtain the physical solution. The problem of finding the proper boundary condition is complex and is generally further exacerbated because the diffusion approximation is not valid near the boundary. Inspite of this basic difficulty, diffusion theory is used widely due to its simplicity and the applicability of numerous analytical and numerical techniques for its solution in finite domains of arbitrary geometry. Approximate boundary conditions are generally adopted which have been shown to be fairly accurate. Here, we adopt the general boundary condition [19]

$$\hat{n} \cdot \vec{J}(\vec{r}, \omega) = \alpha \Phi(\vec{r}, \omega). \quad (5)$$

The value of α can be defined based on boundary considerations or taken as a fitting parameter for a given interface. In Eq. (5) \hat{n} is the unit outward normal to the boundary surface. Using Eq. (5), it is now possible to transform Eq. (3) into an integral equation, the solution of which will provide one with a physical picture of the interaction of the diffuse photon density wave with the turbid media. The basic interaction of light with the molecules of the turbid media is already included in the absorption and scattering parameters. The determination of these material parameters is at the heart of the optical modality for cancer diagnostics. The integral representation forms a basis for extraction of these parameters from measurements of the diffusion waves at the boundary. We next derive the integro-differential equation using Eqs. (3) and (5).

We follow the standard Green's function technique for the derivation of an integral equation from a partial differential wave equation [20]. However, we deliberately choose a simple Green's function corresponding to the operator on the left hand side (L.H.S.) of Eq. (3) that satisfies the equation

$$(\nabla^2 + k_d^2) G(\vec{r}, \vec{r}', \omega) = -4\pi\delta(\vec{r} - \vec{r}'), \quad (6)$$

and is given by

$$G_d(\vec{r}, \vec{r}', \omega) = \frac{\exp(i k_d |\vec{r} - \vec{r}'|)}{|\vec{r} - \vec{r}'|}, \quad (7)$$

with

$$k_d = \sqrt{3\bar{\mu}'_s(\frac{i\omega}{c} - \bar{\mu}_a)}. \quad (8)$$

Here $\text{Im}(k_d) > 0$. Notice that our choice of an infinite space Green's function will not limit in any way when we consider finite domains; finite medium effects are properly treated by the boundary integrals. If we now multiply both sides of Eq. (3) and (6) by $G_d(\vec{r}, \vec{r}', \omega)$ and $\Phi(\vec{r}, \omega)$ respectively and subtract the resulting equations from one another and use a number of standard Green's identities, we obtain

$$\begin{aligned} \Phi(\vec{r}, \omega) = & \frac{3\bar{\mu}'_s}{4\pi} \int_V S_0(\vec{r}', \omega) G_d(\vec{r}, \vec{r}', \omega) d^3\vec{r}' + \frac{3}{4\pi} \int_V \bar{S}_1(\vec{r}', \omega) \cdot \nabla' G_d(\vec{r}, \vec{r}', \omega) d^3\vec{r}' \\ & + \frac{1}{4\pi} \int_S (3\alpha\bar{\mu}'_s G_d(\vec{r}, \vec{r}', \omega) + \nabla' G_d(\vec{r}, \vec{r}', \omega) \cdot \hat{n}) \Phi(\vec{r}', \omega) dS' \\ & - \frac{3\bar{\mu}'_s}{4\pi} \int_V (\mu_a(\vec{r}') - \bar{\mu}_a) \Phi(\vec{r}', \omega) G_d(\vec{r}', \vec{r}) d^3\vec{r}' \\ & + \frac{1}{4\pi} \int_V \frac{\mu_s(\vec{r}') - \bar{\mu}'_s}{\mu_s(\vec{r}')} \nabla' \Phi(\vec{r}', \omega) \cdot \nabla' G_d(\vec{r}', \vec{r}) d^3\vec{r}'. \end{aligned} \quad (9)$$

In deriving Eq. (9), we also made use of Eqs. (1)-(2) and (5). V denotes the volume of the turbid medium and the surface bounding the volume is denoted by S. The first two terms on the right hand side (R.H.S.) of Eq.(9) are related directly to the source and the second term on the R.H.S. of Eq.(9) arises because of the presence of the boundary. The solution to this integro-differential equation is unique as long as there exists no non-trivial solutions to the corresponding homogeneous integral equation. It is possible that for certain modulation frequencies the resulting homogeneous integral equation may possess non-trivial solutions. These frequencies will generally be complex and will correspond to resonance behavior of the photon density waves. We shall not dwell with this singular case, but refer the reader to a related paper on resonance theory by one of the authors [15]. Our Eq.(9) differs from the corresponding equation used in reference [14], in which the boundary effect was ignored. The treatment of the source contribution to the integral equation is also different.

For a homogeneous diffusing media, the integro-differential equation becomes

$$\begin{aligned} \Phi(\vec{r}, \omega) = & \frac{3\bar{\mu}'_s}{4\pi} \int_V S_0(\vec{r}', \omega) G_d(\vec{r}, \vec{r}', \omega) d^3\vec{r}' + \frac{3}{4\pi} \int_V \bar{S}_1(\vec{r}', \omega) \cdot \nabla' G_d(\vec{r}, \vec{r}', \omega) d^3\vec{r}' \\ & + \frac{1}{4\pi} \int_S (3\alpha\bar{\mu}'_s G_d(\vec{r}, \vec{r}', \omega) + \nabla' G_d(\vec{r}, \vec{r}', \omega) \cdot \hat{n}) \Phi(\vec{r}', \omega) dS'. \end{aligned} \quad (10)$$

Equations (9) and (10) are the basic equations of our paper. They are derived using the diffusion approximation to photon transport and without any other approximations. Eq. (9) is an integro-differential equation for the photon density wave and involves only the absorption and transport scattering coefficients. Notice that Eq. (9) does not explicitly contain gradients of light diffusion coefficient. Our derivation is exact and does not assume any condition on the gradient of the light diffusion coefficient. As has been pointed out recently [17] neglect of the gradient term leads to cross coupling between scattering and absorption images. Eq. (10) describes the homogeneous or the background photon density field that includes the source contributions (the first two terms on the R.H.S.), as well as contributions from the boundary (the last term of the R.H.S.). Note that Eq. (10) contains only average values of the scattering parameters and the surface integral includes the total field.

Eq. (10) relates the value of the diffuse photon density wave at any point inside the turbid medium to the monopole and dipole moment of the source and to the photon density on the surface bounding the medium. A surface integral equation for the boundary value of the photon density is obtained if we take the point \vec{r} to be on the surface. This limiting operation must be done carefully because the integrals involving the gradient of the Green's function are not continuous when the interior point approaches a point on the surface. The other integrals involving the Green's function however are continuous [21]. From an experimental point of view, if the photon density on the surface surrounding the turbid medium is measured, then one can use Eq. (10) to determine the diffuse photon density wave anywhere inside the medium by simply carrying out the surface integrals in Eq. (10). If the value of this estimated photon density matches that of the measured value at all points on the surface, then an absence of tissue heterogeneity is indicated. In practice there will never be perfect cancellation, but a larger difference indicates the presence of stronger heterogeneities inside the tissue.

Another approximate way to evaluate the background field is to evaluate the surface integrals in Eq. (10) iteratively. First ignore the third surface term involving the boundary values of the photon density in Eq. (10) and use only the first two terms involving the source terms to calculate the first order background field everywhere. Then update the value of the background field by using the first order values in the last integral in Eq. (10). It is important to devise a way to estimate a reasonable background field, because when this field is subtracted from the total measured diffuse photon density field, then the remainder is the field directly attributable to the presence of the heterogeneity.

We have already noted that unlike other integral formulations our integro-differential equation does not contain an explicit term involving the gradient of the transport scattering coefficient. This is important in the inverse problem where the absorption and transport scattering heterogeneity are to be estimated from the measured values of the field. The formalisms that include the gradient term will of necessity have to use a numerical estimate of the gradient value. Such procedures may lead to numerical instabilities and numerical artifacts. We next develop a 3D-slice image reconstruction technique based on the integro-differential equation for the photon density, i.e. the Eqs. (9) & (10).

3.Inversion algorithm for 3D-slice imaging

We make the assumption that the heterogeneities are weak and do not perturb the background field substantially. Then we can approximate the photon density within the integral operator with the background field. With this first order Born approximation, Eq. (9) becomes

$$\begin{aligned} \Phi^P(\vec{r}, \omega) = \Phi^M(\vec{r}, \omega) - \Phi^H(\vec{r}, \omega) &= -\frac{3\bar{\mu}_s}{4\pi} \int_V (\mu_a(\vec{r}') - \bar{\mu}_a) \Phi^H(\vec{r}', \omega) G_d(\vec{r}', \vec{r}, \omega) d^3 r' \\ &+ \frac{1}{4\pi} \int_V \left(\frac{\mu'_s(\vec{r}') - \bar{\mu}_s}{\mu'_s(\vec{r}')} \right) \nabla' \phi^H(\vec{r}', \omega) \cdot \nabla' G_d(\vec{r}', \vec{r}, \omega) d^3 r'. \end{aligned} \quad (11)$$

The superscript M implies measured field and the superscript P denotes the processed (scattered) field values. In Eq.(12), we have used the identity

$$\begin{aligned}\Phi^H(\vec{r}, \omega) \equiv & \frac{3\bar{\mu}'_s}{4\pi} \int_V S_0(\vec{r}', \omega) G_d(\vec{r}, \vec{r}', \omega) d^3\vec{r}' + \frac{3}{4\pi} \int_V \vec{S}_1(\vec{r}', \omega) \cdot \nabla' G_d(\vec{r}, \vec{r}', \omega) d^3\vec{r}' \\ & + \frac{1}{4\pi} \int_S (3\alpha\bar{\mu}'_s G_d(\vec{r}, \vec{r}', \omega) + \nabla' G_d(\vec{r}, \vec{r}', \omega) \cdot \hat{n}) \Phi^M(\vec{r}', \omega) dS'.\end{aligned}\quad (12)$$

The quantity $\Phi^H(\vec{r}, \omega)$ often identified as the background field can be determined from the knowledge of the source and the measured field at the boundary from Eq. (12).

Although our integro-differential equation is valid for arbitrary geometry, from now on we shall restrict ourselves to the case of a plane parallel plate configuration. The plane parallel plate is an accepted clinical diagnostic configuration for breast imaging. It offers the possibility of compressing the breast to decrease its thickness for increased signal strength. We also take the transverse dimension of the plate to be sufficiently larger than the plate separation. Because of the negligibly small value of the field at the periphery of sufficiently large plates, in practice the transverse plate extent can be taken to be infinite. In essence, Eq. (11) is an integral equation for $\mu_a(\vec{r})$, and $\mu'_s(\vec{r})$ with all the other variables such as the background field, the Green's function and the background optical parameters either given or estimated.

In the new integro-differential equation, we use the Weyl representation [22-23] of Green's function

$$G(\vec{r}, \vec{r}', \omega) = \int_{-\infty}^{\infty} dp \int_{-\infty}^{\infty} dq \frac{i}{2\pi n} \exp(ip(x - x') + iq(y - y') + im|z - z'|), \quad (13)$$

$$\text{where } m = \sqrt{k_d^2 - p^2 - q^2}, \quad \text{with} \quad \text{Im}(m) > 0.$$

The direction z is chosen perpendicular to the surface normal and the x and y directions are chosen along the transverse directions. There is a singularity in the z direction as can be seen from the absolute value operator in the exponent of the Weyl representation. This representation is also known as the angular spectrum representation and is fundamental to the theory and algorithm now commonly known as Diffraction tomography [24-25]. Diffraction tomography was applied to far field coherent optical imaging systems, but recently this technique has been extended to the near field diffuse photon density wave based imaging [26-34]. With this representation of Green's function the integrals in x and y become convolution integrals which turn into algebraic products in p, q space. Taking the two-dimensional Fourier transform of Eq. (12) at the detector plane $z = z_d$ we find that

$$\begin{aligned}\hat{\Phi}^P(p, q, z_d, \omega) = & \int_{z_s}^{z_d} dz' \hat{T}_a(p, q, z', \omega) \hat{K}(p, q, z_d - z', \omega) \\ & + \int_{z_s}^{z_d} dz' \hat{\tilde{T}}_s(p, q, z', \omega) \cdot \vec{k} \hat{K}(p, q, z_d - z', \omega),\end{aligned}\quad (14)$$

where

$$T_a(\vec{r}, \omega) = -\frac{3\bar{\mu}_s}{4\pi} (\mu_a(\vec{r}) - \bar{\mu}_a) \Phi^H(\vec{r}, \omega), \quad (15)$$

$$\vec{T}_s(\vec{r}, \omega) = \frac{1}{4\pi} (1 - \frac{D(\vec{r}, \omega)}{\bar{D}}) \nabla \phi^H(\vec{r}, \omega), \quad (16)$$

and

$$\hat{K}(p, q, z_d - z', \omega) = \frac{i}{2\pi n} \exp(im(z_d - z)). \quad (17)$$

In Eqs.(14)-(17), $\vec{k} = \hat{x}p + \hat{y}q + \hat{z}m$ is the wave vector and z_s, z_d denote the positions of the source and detector plates respectively. The caret (^) over functions signifies the Fourier transform of a function. Several things are worth noting at this point. First, the absorption coefficient contribution depends on a scalar function, while the transport scattering coefficient depends on the product of two vectors. Second, the gradient of the diffuse photon density wave interacts with the scattering heterogeneity, while the diffuse photon density wave interacts with the absorption heterogeneity. Finally, the inverse of the transport scattering

coefficient has been explicitly replaced by the photon diffusion coefficient $D = \frac{c}{3\mu'_s}$.

Eq. (14) is a very simple looking equation, but in fact a lot of physics is hidden. The Fourier transform of the so-called tumor functions, T_a and T_s which are products of the scattering parameters and the background field in real space, will be convolution integrals in the Fourier space. This convolution in the spatial frequency space between the tumor parameters and the background field couples temporal frequency, ω with spatial frequency (p, q). This implies that the use of a set of modulation frequencies does not in any easy manner let us solve for the spatial Fourier amplitudes of the tumor functions. This coupling is eliminated if the background field is *spatially* in the form of a plane wave rather than a spherical wave. The usefulness of plane wave sources is well known in the field of diffraction tomography [24].

We will use a series of plane waves whose central modulation frequencies are stepped to span some frequency bandwidth. For the plane wave case the tumor functions, \hat{T}_a, \hat{T}_s , can be written as a product of two functions. One function, \hat{t}_a or \hat{t}_D , contains information about the heterogeneities and depends upon (p, q, z) and the other function depends upon the background plane waves and modulation frequency (see Eq. (18) below). One can then utilize this temporal frequency bandwidth to obtain resolution in the longitudinal (z) direction. The key advantage of using the series of stepped central modulation frequencies is that the detection system is still narrow band and one can use maximum permissible signal strength at all discrete frequencies. We plan to publish in a later paper the details of this technique with simulated data, but here we point out the salient features of the method. For the plane wave case we find

$$\begin{aligned} \hat{T}_a(p, q, z, \omega) &= t_a(p, q, z) \{ \Phi^+ \exp(+im_0 z) + \Phi^- \exp(-im_0 z) \}, \\ \hat{T}_s(p, q, z, \omega) &= t_d(p, q, z) \{ \vec{k}_0^+ \Phi^+ \exp(+im_0 z) + \vec{k}_0^- \Phi^- \exp(-im_0 z) \}, \\ \hat{t}_a(p, q, z) &= \frac{3}{4\pi} [\bar{\mu}_a \delta(p - p_0) \delta(q - q_0) - \mu_a(p - p_0, q - q_0)], \end{aligned}$$

$$\hat{t}_D(p, q, z) = \frac{1}{4D} [\bar{D} \delta(p - p_0) \delta(q - q_0) - D(p - p_0, q - q_0)],$$

and $\vec{k}_0^+ = \hat{x}p_0 + \hat{y}q_0 + \hat{z}m_0, \quad \vec{k}_0^- = \hat{x}p_0 + \hat{y}q_0 - \hat{z}m_0.$ (18)

Here $p_0 = \text{Re}(k_d) \cos(\theta) \cos(\phi), q_0 = \text{Re}(k_d) \cos(\theta) \sin(\phi)$ where θ is the angle the plane wave makes with respect to the z direction, and ϕ is the corresponding azimuthal angle. Care must be exercised in the angle interpretations as we are dealing with attenuating plane waves. For the case of a normal incidence, $p_0 = 0$ and $q_0 = 0$. The parameter $m_0 = \sqrt{k_d^2 - p_0^2 - p_0^2}$ with $\text{Im}(m_0) > 0$. The general mode structure of the background plane wave for the parallel plate slab geometry can be shown from the solution of the homogeneous equation (Eq. (10)) to be a sum of both forward and backward propagating waves [33]

$$\Phi_0(x, y, z, \omega) = \Phi^+ \exp(ip_0x + iq_0y + im_0z) + \Phi^- \exp(ip_0x + iq_0y - im_0z). \quad (19)$$

Here, Φ^+ , and Φ^- are complex constants obtained from solution or measurements as discussed earlier in the section on the background field.

We approximate the integration in Eq. (14) in the z variable by means of a sum over N slices between the parallel plates (the slice thickness can be different and is denoted by Δz_j with j ranging from 1:N), and use Eqs. (15)-(19) to obtain the following result

$$\hat{\Phi}(z^d, \omega_j) = \sum_{i=1}^N [\hat{t}_a(z_i) \hat{f}_1(z_i, \omega_j) + \hat{t}_a(z_i) \hat{f}_2(z_i, \omega_j)] \quad \text{for } j = 1:2N, \quad (20)$$

where

$$\begin{aligned} \hat{f}_1(z_i, \omega_j) &= \Delta z_i \{ \Phi^+ \exp(+im_0 z_i) + \Phi^- \exp(-im_0 z_i) \} \hat{K}(z_d - z_i, \omega), \\ \hat{f}_2(z_i, \omega_j) &= -\Delta z_i \{ (pp_0 + qq_0 + mm_0) \Phi^+ \exp(+im_0 z_i) + \\ &\quad (pp_0 + qq_0 - mm_0) \Phi^- \exp(-im_0 z_i) \} \hat{K}(z_d - z_i, \omega). \end{aligned} \quad (21)$$

Here, we suppressed the (p,q) arguments for the sake of brevity. Eq. (20) provides 2N linearly independent complex equations that can be solved for the two dimensional Fourier transform of the absorption and scattering coefficients at the N selected slice positions in the z direction. This can be seen more clearly when Eq. (20) is written in a matrix form

$$\hat{\Phi} = \underline{\underline{\hat{f}}} \cdot \underline{\underline{\hat{t}}}. \quad (22)$$

Where $\hat{\Phi}$ is the vector of 2N dimension consisting of the measurements of the processed (scattered) field at the 2N modulation frequencies, $\underline{\underline{\hat{f}}}$ is a 2NX2N matrix consisting of two

2NXN matrices \hat{f}_1 , and \hat{f}_2 defined in Eqs. (21a)-(21b). Eq. (22) can be solved by direct matrix inversion as shown below or iteratively by following methods such as SIRT, ART [13]. \hat{t} consists of the sum of the two N dimensional vectors \hat{t}_a and \hat{t}_D .

$$\hat{t} = (\hat{f})^{-1} \cdot \hat{\Phi}. \quad (23)$$

\hat{t} in Eq. (23) is the two-dimensional Fourier transform of the absorption and scattering coefficients at each of the N number of slices in the direction normal to the plates (the z direction). The values of the scattering coefficients in the direction transverse to the surface normal (the x and y directions) are obtained by applying the two-dimensional inverse Fourier transform, i.e.

$$t(x, y, z_i) = \frac{1}{4\pi^2} \int_{-\infty}^{\infty} \int_{-\infty}^{\infty} dp dq (\hat{f}(p, q))^{-1} \cdot \hat{\Phi}(p, q) \exp(-ipx - iqy) \quad \text{for } i = 1 : N \quad (24)$$

For the Breast imaging case, Eq. (24) provides one with 3D-slice images of the absorption and scattering coefficients at the selected "virtual" slice positions in the interior of the breast compressed between the two plates. These images may be reconstructed with light of different wavelengths within the near- infrared window. Such measurements improve the usefulness of nearfield optical imaging modality employing diffuse photon density waves.

4. Conclusion

We presented a rigorous derivation of a new integro-differential equation for the diffuse photon density wave in an inhomogeneous bounded turbid medium within the diffusion approximation. The resulting equation contains only the absorption and scattering coefficients and does not include gradients of the light diffusion coefficient. We also derived a novel surface integral equation for the diffuse photon density waves for the case of a bounded homogeneous turbid medium. We used the theory to develop a detailed imaging algorithm that provides one with 3D-slice images of the absorption and scattering coefficients of tissue (breast) that is compressed between two parallel plates. We believe this algorithm will be useful in increasing the specificity of the near infrared optical imaging modality. Our algorithm being based on inhomogeneous wave equation of the Helmholtz type may also be applicable to other imaging modalities such as ultrasound.

Acknowledgements

We gratefully acknowledge useful conversations with Britton Chance, Joe Culver, Leonid Zubkov, Monica Holboke, Turgut Durduran, Xingde Li, Regine Choe. We acknowledge partial support from US Army RO DAMD17-97-1-7272 and NIH 1-RO1-CA75124-01 grants respectively.

Parallel three-dimensional diffuse optical tomography

M. J. Holboke and A. G. Yodh

Dept. of Physics and Astronomy, University of Pennsylvania, 209 S. 33rd Street, Philadelphia, PA 19104
Phone: (215)898-5150, Fax: (215)898-2010, E-mail: mholboke@physics.upenn.edu

Abstract: Three-dimensional diffuse optical tomography is a computationally intensive procedure. An iterative perturbative algorithm is followed and parallelized. The results show that three-dimensional images can be reconstructed on realistic time scales compared to the synchronous approach.

©1999 Optical Society of America

OCIS codes: (100.6890) Three-dimensional image processing; (170.6960) Tomography; (170.5280) Photon migration

1. Introduction

Most Diffuse Optical Tomography (DOT) has occurred in 2-D. In the best of these cases, a cylindrical geometry was employed to reduce the dimensionality of the problem [1,2]. In fact, only recently have full 3-D reconstructions been accomplished and compared to 2-D [3,4]; not surprisingly, the 3-D images were superior. Additionally, in any clinical setting the problem is necessarily 3-D. Therefore, we are convinced that 3-D reconstruction is the best approach for optimal image fidelity in a clinical setting.

The main barriers for 3-D reconstruction are memory requirements and computational processing time. Arridge and Schweiger have presented an algorithm that reduces memory requirements significantly [5]. Unfortunately, the computational processing time was still significant. Subsequently, they recently presented a 3-d segmented reconstruction using parallel processing [4]. In this application they parallelized the forward problem matrix solver and received a factor of four speed-up when using eight processors. While, this is promising it is still necessary to speed up the reconstruction time as much as possible in order to make 3-d clinical imaging a reality. Therefore, we have developed a parallel 3-d DOT algorithm that parallelizes the algorithm itself and plans for expanding the parallelization are underway.

2. Methods

A variety of methods have been developed for (DOT). These include fitting to an analytic solution [6-8], backprojection method [9-11], diffraction tomography in k-space [12-16], perturbation approach [17-23], elliptic systems method (ESM) [24,25], and direct method [26]. Each method has advantages and drawbacks, but the only method to date that has been utilized in full 3-D simultaneous reconstructions of absorption and scattering coefficients for complicated geometries and boundary conditions is the perturbation approach. Within the perturbation approach there are a couple of methods to solving the forward problem and determining the Jacobian [for a review see 27]. Additionally, there are a variety of methods for solving the inverse problem [2,5,27-31].

Our algorithm is based on an iterative perturbative approach that uses the explicit adjoint formulation for the inverse problem and parallel processing in master-slave style (fig. 1). This requires solving the forward problem for each source (NS=number of sources), solving the adjoint problem for each detector (ND=number of detectors), and solving the inverse problem ([NMxNV], NM=number of measurements, NV=number of voxels). In the first step each node has its own set of arrays and variables that are initialized. During the second step the master sends out the optical properties, which in the first iteration are just the background values. In the third step, the slaves calculate the solutions to the forward problem; consequently NS slaves are used in this step. The solution vectors are then returned to the master and at this point the master checks for convergence. If convergence has not be achieved then the slaves calculate the solutions to the Green's function resulting in ND slaves being utilized. Again the solution vectors are returned to the master and the Jacobian is determined. Next the master solves the inverse problem by using a spatially variant regularized conjugate gradient optimization method [2,21]. Finally, the optical properties are updated on the master and the algorithm repeats until convergence has been achieved.

The outlined approach utilizing parallel processing results in many gains. First we are able to calculate our forward solutions simultaneously. Therefore, what would normally take $NS \times \Delta t_{\text{forward}}$ ($\Delta t_{\text{forward}}$ = the time of one forward solve) is now $\{\text{NS}/\text{Min(NS, NP (number of processors))}\} \times \Delta t_{\text{forward}}$ plus some small amount of time for communication. Similarly, for the Green's function, processing is reduced from $ND \times \Delta t_{\text{Green}}$ (Δt_{Green} = the time of one Green's function solve) to $\{\text{ND}/\text{Min(ND, NP (number of processors))}\} \times \Delta t_{\text{Green}}$. If $NP > NS, ND$ then our matrix solve time is reduced by $\sim NS + ND$.

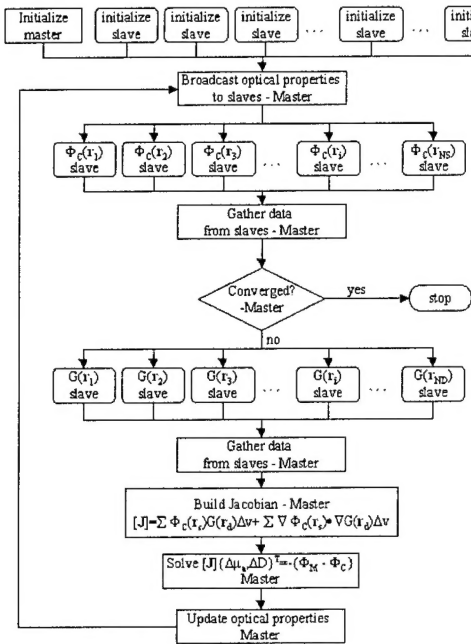


Fig. 1: Algorithm for full 3-D reconstruction.

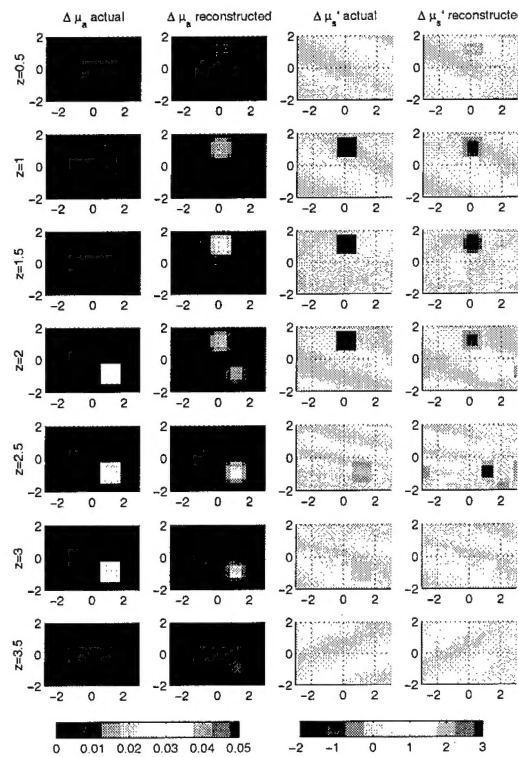


Fig. 2: Maps of $\Delta\mu_a$ (left) and $\Delta\mu_s'$ (right) actual and reconstructed.

3. Results

A full 3-D parallel reconstruction based on numerically generated frequency domain data with 0.1% noise in amplitude and 0.1 degree noise in phase is demonstrated. The size of the domain was 20cmx10cmx4cm and the grid was 81x41x33, equivalent to 0.25cmx0.25cmx0.125cm resolution. The size of the inverse grid was 19x9x4, equivalent to 1cm voxels and 1368 unknowns. There are five sources with the same frequency modulation (140MHz) and 81 detectors, equivalent to 810 measurements. The source locations are (0,0,0), (-1,1,0), (1,1,0), (-1,-1,0), and (1,-1,0). The detector locations are a grid from -2 to 2 in x and y every 0.5cm. There are two 1cm-cube heterogeneities located at (0,1,1.5) and (1,-1,2.5). The optical properties are $\mu_a=0.05\text{cm}^{-1}$ and $\mu_s'=8.0\text{cm}^{-1}$ for the background, $\mu_a=0.10\text{cm}^{-1}$ and $\mu_s'=6.0\text{cm}^{-1}$ for the cube at (0,1,1.5), and $\mu_a=0.08\text{cm}^{-1}$ and $\mu_s'=10.0\text{cm}^{-1}$ for the cube at (1,-1,2.5). The source strength, although it is known here, is generally unknown in clinical settings. Therefore, in order to remove the source term dependence background measurements are made at the detector locations (Φ_M^0); the corresponding calculated values are the first forward solutions (Φ_C^0). These values are then divided out of the inverse problem for each measurement (*i.e.* $\Phi_M=\Phi_M/\Phi_M^0$, $\Phi_C=\Phi_C/\Phi_C^0$). The 3-D reconstruction is shown in Fig. 2 along with the actual values. Convergence was achieved when χ^2 changed less than 0.1%, this occurred by the 67th iteration. The reconstructed cube at (0,1,1.5) had $\mu_a=0.08206\text{cm}^{-1}$ and $\mu_s'=5.9802\text{cm}^{-1}$ and the cube at (1,-1,2.5) had $\mu_a=0.07721\text{cm}^{-1}$ and $\mu_s'=12.2638\text{cm}^{-1}$. The total time was 5.6hrs on 20nodes (*i.e.* 1 master and 19 slaves), while synchronously it took 20.8hrs.

4. References

1. B. W. Pogue *et al.*, "Instrumentation and design of a frequency-domain diffuse optical tomography imager for breast cancer detection," *Opt. Exp.* **1**, 391-403 (1997).
2. B. W. Pogue, *et al.*, "Spatially variant regularization improves diffuse optical tomography," *Appl. Opt.* **38**, 2950-2961 (1999).
3. M. Schweiger and S. R. Arridge, "Comparison of two- and three-dimensional reconstruction methods in optical tomography," *Appl. Opt.* **37**, 7419-7428 (1998).
4. M. Schweiger, *et al.*, "Optical tomography using the SCIRun problem solving environment: Preliminary results for three-dimensional geometries and parallel processing," *Opt. Exp.* **4**, 263-269 (1999).

5. S. R. Arridge and M. Schweiger, "A gradient-based optimisation scheme for optical tomography," *Opt. Exp.* **2**, 213-226 (1998).
6. J. B. Fishkin *et al.*, "Frequency-domain photon migration measurements of normal and malignant tissue optical properties in a human subject", *Appl. Opt.* **36**, 10-20 (1997).
7. S. Fantini *et al.*, "Assessment of the size, position, and optical properties of breast tumors *in vivo* by noninvasive optical methods," *Appl. Opt.* **37**, 1982-1989 (1998).
8. D. Grosenick *et al.*, "Development of a time-domain optical mammograph and first *in vivo* applications," *Appl. Opt.* **38**, 2927-2943 (1999).
9. S.A. Walker *et al.*, "Image reconstruction by backprojection from frequency-domain optical measurements in highly scattering media," *Appl. Opt.* **36**, 170-179 (1997).
10. S.B. Colak *et al.*, "Tomographic image reconstruction from optical properties in light-diffusing media," *App. Opt.* **36**, 180-213 (1997).
11. Oliver Dorn, "A transport-backtransport method for optical tomography", *Inverse Problems* **14**, 1107-1130 (1998).
12. J.C. Schotland, "Continuous-wave diffusion imaging", *J. Opt. Soc. Am. A* **14**, 275-279 (1997).
13. C.L. Matson *et al.*, "Three-dimensional tumor localization in thick tissue with the use of diffuse photon-density waves", *Appl. Opt.* **36**, 214-220 (1997).
14. X.D. Li *et al.*, "Diffraction tomography for biochemical imaging with diffuse-photon density waves", *Opt. Lett.* **22**, 573-575 (1997).
15. C.L. Matson and H. Li, "Analysis of the forward problem with diffuse photon density waves in turbid media by use of a diffraction tomography model," *J. Opt. Soc. Am. A* **16**, 455-466 (1999).
16. T. Durduran *et al.*, "Algorithms for 3D localization and imaging using near-field diffraction tomography with diffuse light," *Opt. Exp.* **4**, 247-262 (1999).
17. J.C. Schotland *et al.*, "Photon hitting density", *Appl. Opt.* **32**, 448-453 (1993).
18. S.R. Arridge and M. Schweiger, "Photon-measurement density functions. Part 2: Finite-element-method calculations," *Appl. Opt.* **34**, 8026-8037 (1995).
19. M.A. O'Leary *et al.*, "Experimental images of heterogeneous turbid media by frequency-domain diffusing-photon tomography," *Opt. Lett.* **20**, 426-428 (1995).
20. W. Cai *et al.*, "Time-resolved optical diffusion tomographic image reconstruction in highly scattering media", *Proc. Nat. Acad. Sci. USA* **93**, 13561-13564 (1996).
21. Y. Yao *et al.*, "Frequency-domain optical imaging of absorption and scattering distributions by a Born iterative method," *J. Opt. Soc. Am. A* **14**, 325-342 (1997).
22. E. M. Sevick-Muraca, *et al.*, "Role of higher-order scattering in solutions to the forward and inverse optical-imaging problems in random media," *Appl. Opt.* **36**, 9058-9067 (1997).
23. K. D. Paulsen and H. Jiang, "Spatially varying optical property reconstruction using a finite element diffusion equation approximation," *Med. Phys.* **22**, 691-701 (1995).
24. M.V. Klibanov *et al.*, "A fast and accurate imaging algorithm in optical/diffusion tomography," *Inv. Prob.* **13**, 1341-1361 (1997).
25. Y.A. Gryazin *et al.*, "Imaging the diffusion coefficient in a parabolic inverse problem in optical tomography," *Inv. Prob.* **15**, 373-397 (1999).
26. M.F. Maritz *et al.*, "Recovery of the absorption coefficient from diffused reflected light using a discrete diffusive model", *SIAM J. Appl. Math.* **59**, 58-71 (1998).
27. S. R. Arridge, "Optical tomography in medical imaging," *Inv. Prob.* **15**, R41-R93 (1999).
28. W. Zhu, *et al.*, "Wavelet-Based Multiresolution Regularized Least Squares Reconstruction Approach for Optical Tomography," *IEEE Transactions on Medical Imaging* **16**, 210-217 (1997).
29. M. J. Eppstein, *et al.*, "Biomedical optical tomography using dynamic parameterization and Bayesian conditioning on photon migration measurements," *Appl. Opt.* **38**, 2138-2150 (1999).
30. J. C. Ye, *et al.*, "Modified distorted Born iterative method with an approximate Frechet derivative for optical diffusion tomography," *J. Opt. Soc. Am. A* **16**, 1814-1826 (1999).
31. J. C. Ye, *et al.*, "Optical diffusion tomography by iterative-coordinate-descent optimization in a Bayesian framework," *J. Opt. Soc. Am. A* **16**, 2400-2412 (1999).